Effects of Negative Valve Overlap on HCCI Combustion and its use in the Control of HCCI Combustion Timing

by

Alexander E. Schramm

A thesis submitted in partial fulfillment of the requirements for the degree of

Master of Science

Department of Mechanical Engineering
University of Alberta

Abstract

Homogeneous charge compression ignition (HCCI) combustion can produce higher efficiencies and lower emissions when compared to tradition spark or compression ignition engines. This study reports an experimental investigation into the effects of valve timings on HCCI combustion conditions. Using a single cylinder engine with state-of-the-art electromagnetic variable valve timing (EVVT) fully independent valves, a series of tests are conducted with varying negative valve overlap (NVO). The in-cylinder residual trapped by the NVO causes an advance in combustion timing, a shortening of burn duration as well as increase in load and increase in brake specific fuel consumption. Asymmetric valve timings are also investigated and show complex behavior with high sensitivity of combustion timing in certain operating ranges. Finally, these strategies are implemented as a set of feedback controllers including a proportional-integral (PI) controller and a feedforward with integral action controller. Both controllers have good tracking for step changes in combustion timing setpoint with the feedforward controller providing a rise time of just four cycles.

ACKNOWLEDGEMENTS

Firstly I would like to thank Dr. Koch not only for the opportunity for this endeavor but also the patience, guidance and financial support provided along the way. Without him none of this would have been possible and I am in his debt.

To my parents, who's endless support and love have been with me the whole way, sincere thanks for everything you have provided and done to keep me following my dreams.

A special thanks to Bernie Faulkner from the mechanical engineering shop, who always went above and beyond whenever I was in need of help.

Finally to my colleagues over the years, thank you for the camaraderie and experiences gained along the way.

Table of Contents

List of Tables

LIST OF FIGURES

NOMENCLATURE

Acronyms

aTDC	after Top Dead Center
BSFC	Brake Specific Fuel Consumption
bTDC	before Top Dead Center
CAS	Combustion Analysis System
CAD	Crank Angle Degree
CA50	Crank Angle of 50% mass burned
CI	Compression Ignition
CO	Carbon Monoxide
CO_2	Carbon Dioxide
DOT	Department of Transportation
EGR	Exhaust Gas Recirculation
EPA	Environmental Protection Agency
EVC	Exhaust Valve Closing
EVO	Exhaust Valve Opening
EVVT	Electromagnetic Variable Valve Timing
HCCI	Homogeneous Charge Compression Ignition
ICE	Internal Combustion Engine
IMEP	Indicated Mean Effective Pressure
IVC	Intake Valve Closing

IVO	Intake Valve Opening
LHV	Low Heating Value
LQ	Linear Quadratic
MEP	Mean Effective Pressure
MPC	Model Predictive Control
NHTSA	National Highway Traffic Safety Administration
NO_x	Oxides of Nitrogen
NVO	Negative Valve Overlap
O_2	Oxygen
PI	Proportional Integral
PID	Proportional Integral Derivative
PRF	Primary Reference Fuel
RMS	Root Mean Square
SI	Spark Ignition
SNVO	Symmetric Negative Valve Overlap
SOC	Start of Combustion
TDC	Top Dead Center
VVT	Variable Valve Timing

Symbols

γ	Ratio of Specific Heats
$\delta CA50$	Error in CA50
$\delta IMEP$	Error in IMEP
δP	Error in Cylinder Pressure
$\eta_{Combustion}$	Combustion Efficiency
$\eta_{Thermal}$	Thermal Efficiency
η_V	Volumetric Efficiency
θ	Crankshaft Angle
ν	Degrees of Freedom
ρ_{Air}	Density of Air in Intake Runner
C_P	Constant Pressure Specific Heat
$E_{Injected}$	Injected Energy
e_k	Discrete Output Error
$e(t)$	Output Error Signal
$HR_{50\%}$	Value of Heat Release Closest to and Above 50%
$HR_{\%}$	Heat Release Percentage
K	Number of Error Sources
K_D	Derivative Gain
K_I	Integral Gain
K_P	Proportional Gain
m_{Air}	Mass of Air
$m_{Excess\,air}$	Mass of Excess Air
m_{Fuel}	Mass of Injected Fuel
$m_{Residual}$	Mass of Residual

m_{Stoich}	Mass of Air, Stoichiometric
N	Number of Samples
P	Cylinder Pressure
$Q(\theta)$	Heat Release
$Q_{Net}(\theta)$	Cumulative Heat Release
Q_{Total}	Total Heat Release
$r_{Dilution}$	Dilution Ratio
$r(t)$	Setpoint Signal
R_U	Universal Gas Constant
$R(X)$	Value Equation
S_i	Sample Variance
$t_0.025$	Student Distribution Value
T_s	Sample Time
$U_{0.95}$	Sample Uncertainty
u_k	Discrete Plant Input
U_R	Repeatability Uncertainty
$u(t)$	Plant Input Signal
V	Cylinder Volume
V_d	Displaced Volume
$\bar{X}$	Sample Mean
X_i	Sample Value
y	Plant Output
y_{Set}	Output Setpoint
$y(t)$	Output Signal

Chapter 1

Introduction

1.1 Motivation

Emissions standards worldwide are becoming more stringent. For example, Tier 3 automobile and light truck emissions standards propose to decrease tailpipe nitrous oxides (NO_x) and hydrocarbons by over 80% and particulate emissions by 70% from 2016 levels by 2025 [EPA, 2013]. Passenger vehicles in the United States are also required to increase overall fuel economy by 60% from 2016 levels by 2025 [DOT, NHTSA, 2012]. This requirement has led engine and automobile manufacturers looking into fuel saving and emission reducing methods such as engine down-sizing and turbocharging, off-cycle improvements such as idle stop-start, and transmission, rolling resistance and aerodynamic improvements. Alternative methods include fully electric or electric hybrid vehicles, fuel cell vehicles, compressed natural gas engines, extreme lightweight vehicles (carbon fibre body and chassis) or homogeneous charge compression ignition (HCCI) engines [Weissler, 2013].

Although the alternatives to the conventional internal combustion engine (ICE) mentioned above are available, when the life-cycle is looked at, they are not yet a viable option [EPA, 2012]. A gasoline ICE is also shown to be more sensitive to engine efficiency and technology improvements, as well as less sensitive to mass increases [Atkins and Koch, 2003]. The HCCI combustion cycle can operate in both gasoline spark ignition (SI) and Diesel compression ignition (CI) engines with little to no modification. HCCI uses the existing fuel system and combustion chamber and the engine can be switched between the conventional (SI or CI) operating mode and HCCI [Widd et al., 2011]. For this reason, HCCI is an attractive option to improving overall fuel economy and reducing tailpipe emissions.

Unlike SI and CI operating modes, HCCI does not have a direct ignition timing control mechanism. The ignition timing in HCCI operation is dependent on the chemical kinetic state of the in-cylinder mixture at intake valve closing (IVC). This condition creates a need to control the mixture temperature and/or composition at IVC.

1.2 Problem Statement

The objective of this study is to examine experimentally the effects of valve timing strategies on HCCI engine operation using a state-of-the-art electromagnetic variable valve timing (EVVT) system. The effects on HCCI operating region, combustion timing and duration, load, efficiency and emissions are examined. Using these findings several different control strategies for controlling combustion timing are developed.

1.3 Thesis Organization

This thesis is organized into six chapters. Chapter two begins with an introduction of the basics concepts of HCCI combustion, EVVT valves, negative valve overlap and valve timing strategies, combustion metrics used in this thesis and examines previous work. Chapter three covers the experimental setup, experimental uncertainty and the testing conditions and operating points used. Chapter four contains the results and discussion of the tests using different valve strategies and their effects on HCCI combustion. Chapter five details combustion timing control work in HCCI, including a PI controller and a feedforward/feedback controller. Finally, Chapter six presents conclusions of this study.

1.4 Contributions

The major contributions of this study are:

- Mapping of the engine operating region and analysis of the effects of engine inputs on engine operation.
- A detailed experimental error analysis for the engine setup in this study
- Documentation of procedures needed for this complex engine setup

Chapter 2

Background

An overview of the fundamental topics discussed in this study are given in this chapter. A short summary of previous research pertinent to this study is also given.

2.1 HCCI

HCCI is described as a four-stroke engine cycle where a homogeneous air/fuel mixture is ignited by cylinder compression alone [Najt and Foster, 1983]. Where the SI cycle uses a spark plug to initiate combustion, and the CI cycle uses the injection of fuel into a compressed (hot) air mixture, HCCI does not have a direct control of combustion timing. Figure 2.1 shows a comparison of the three different combustion cycles.

Drawbacks of HCCI operation include the difficulty of controlling ignition timing, a limited and low range of loads, and difficulty in switching between HCCI and other modes. There is research into the areas of load range extension [Weall et al., 2012] and mode switching [Widd et al., 2011]. This study focuses on the control of combustion timing.

The combustion timing in an HCCI engine depends predominately on the chemical kinetic state of the in-cylinder mixture at IVC. Other dependencies include heat transfer to the cylinder walls, compression ratio and rate of compression due to engine speed. The control of HCCI combustion timing therefore can be implemented

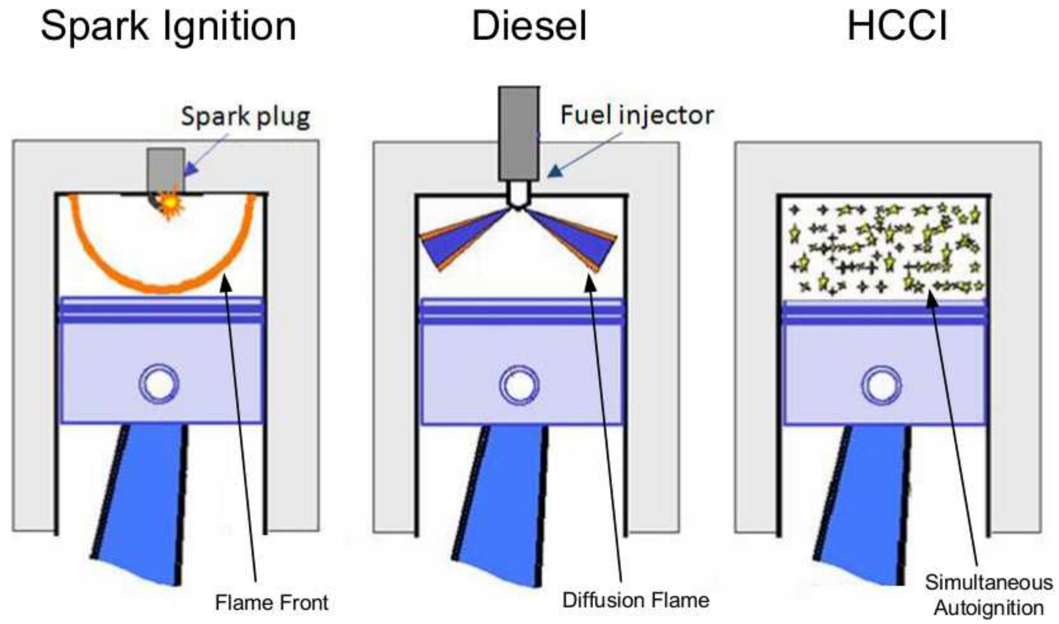

Figure 2.1: Comparison of SI, CI and HCCI combustion.

through controlling the mixture temperature and/or composition at IVC. There are several strategies for controlling the mixture temperature and composition. One is the thermal management of intake air [Haraldsson et al., 2004], another is the use of variable compression ratio [Haraldsson et al., 2002], and there are dual fuel strategies for controlling fuel octane, therefore controlling mixture properties [Audet, 2008] [Audet and Koch, 2009].

A strategy of significant interest, and the topic of this study, is the reinduction of combustion products through internal exhaust gas recirculation (EGR). Unlike external EGR, internal EGR is achieved through different valve timing strategies. The re-induction of exhaust gases effects the dilution and temperature of the mixture at IVC, allowing HCCI combustion timing to be controlled.

2.2 Electromagnetic Valves

To achieve independent, cycle-by-cycle combustion timing using variable valve timings, a more complex system than a conventional camshaft system is needed. Typical production valve timing control systems on conventional camshafts are cam-phasers [Audet, 2008] [Audet and Koch, 2009]. This allows the intake and exhaust timings to be shifted by about 40 crank angle degrees (CAD). The drawbacks are that both the opening and closing timings are moved simultaneously, and the actuation is typically too slow for cycle-by-cycle changes at higher engine speeds.

For cycle-by-cycle independent timing a crankshaft-independent system is needed, such as electromagnetically or hydraulically actuated valves. There are several styles available for independent valve actuation. [Agrell et al., 2003b] use a fully hydraulic system. These systems are large, draw a lot of power and are expensive [Mashkournia, 2012]. They are suitable for research and development purposes but not for industrial or consumer use.

This study is conducted with the use of electromagnetic valves. These valves offer fully independent, cycle-by-cycle valve timing changes in a small and light-weight package [Mashkournia, 2012]. Drawbacks include the need for complex controllers for valve operation, which leads to reliability issues, as well as temperature and wear sensitivity.

2.3 Negative Valve Overlap

There are different strategies used to re-induct exhaust gas. In a standard engine, exhaust valve close (EVC) and intake valve open (IVO) timings are usually set at approximately top dead centre (TDC) of the exhaust stroke. If both timings are moved as a unit into the exhaust stroke, exhaust gas is deposited into the intake and re-breathed into the cylinder during the intake stroke. In a similar fashion, if the timings are moved as a unit into the intake stroke, exhaust is expelled into the exhaust and then re-inducted into the cylinder before the intake valve is opened.

The techniques described above are considered “re-breathing” techniques, where exhaust is expelled from the cylinder then re-inducted back in before intake or with the intake charge. Another method, and the method used in this study, is the re-compression of the exhaust gases. This is accomplished using negative valve overlap (NVO), where the exhaust valve is closed earlier than TDC, and the intake valve is opened late, or after TDC. This action traps exhaust residual within the cylinder to be re-compressed by the piston, and then expanded until the intake valve is opened and fresh charge inducted. If EVC and IVO timings are symmetrically timed around TDC, it is called symmetric NVO (SNVO), this mode is shown in Figure 2.2.

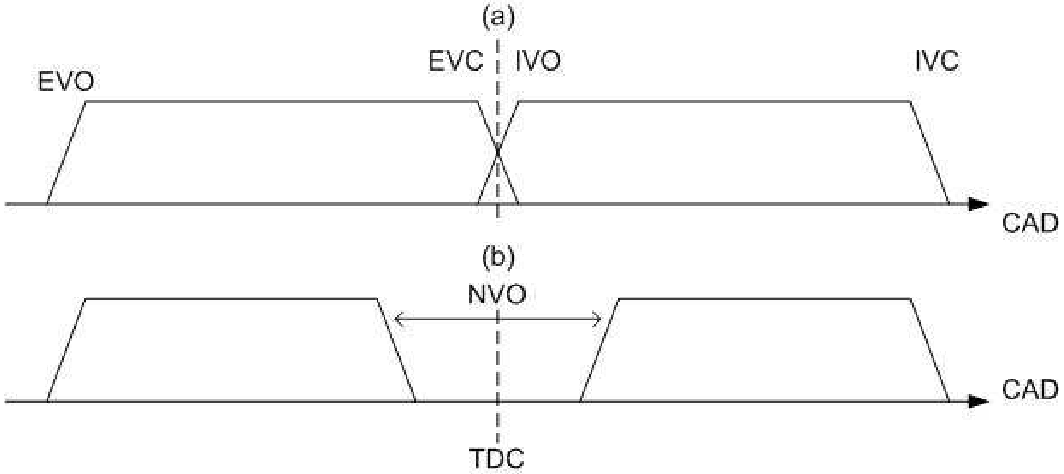

Figure 2.2: Valve opening schematic as a function of crank angle degrees (CAD) of (a) conventional valve timing and (b) symmetric negative valve overlap (SNVO).

Another valve strategy experimentally explored in this study is asymmetric NVO. In this study, the asymmetric NVO timings use a constant NVO duration (CAD between EVC and IVO timings) while the timings are advanced or retarded about TDC. The timings for asymmetric NVO, referred to in this study, are the location of the centre of the NVO duration. For example, if a test with a constant NVO duration of 60 CAD and EVC timing is 40 CAD before TDC, and IVO is set to 20 CAD after TDC, the timing would be listed as 10 CAD before TDC. A visual representation of asymmetric NVO is shown in Figure 2.3.

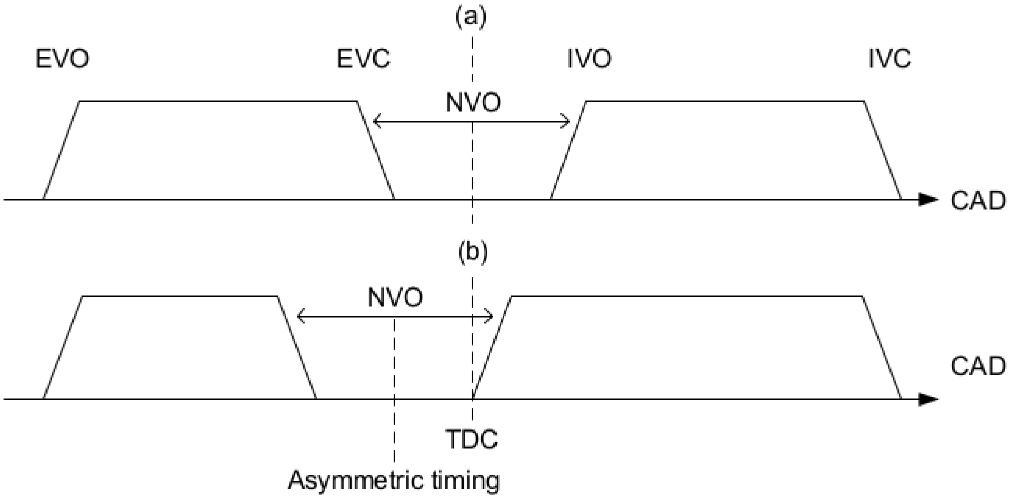

Figure 2.3: Valve opening schematic as a function of crank angle degrees (CAD) of (a) symmetric and (b) asymmetric negative valve overlap.

2.4 Control and Modelling Strategies

Typically the goal of a controller is either regulation (keeping an output at a constant value) or tracking (making the output follow a desired value). To achieve this goal, feedback from the output is required. A basic feedback controller is a proportional-integral-derivative (PID) controller. A controller structure is shown in Figure 2.4 where the plant is the system that is to be controlled and the setpoint is the desired value for the output.

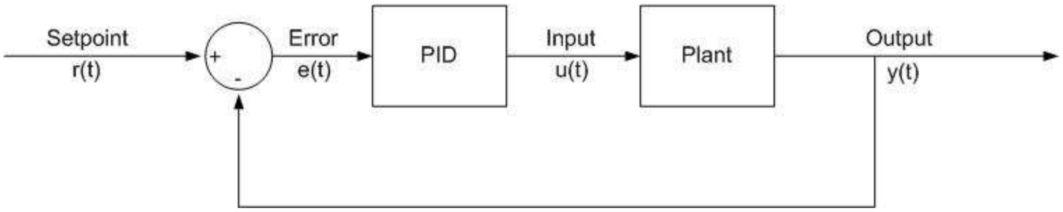

Figure 2.4: Basic structure of a feedback PID controller.

The PID in Figure 2.4 contains the formula for calculating the plant input value. For a PID controller the input is calculated from the output error, or $e(t) = y_{Set} - y$.

In continuous time, the PID is:

$$u(t) = K_P e(t) + K_I \int_0^t e(\tau) d\tau + K_D \frac{de(t)}{dt} \tag{2.1}$$

The three gains in the equations are then tuned (either manually by trial and error, or by other methods) to produce an acceptable response [Franklin et al., 2010]. The error is multiplied by a proportional gain (K_P), this value dictates the responsiveness of the controller, with a low K_P having low responsiveness to error. For many systems, if K_P is too large, the system can become unstable. Solely proportional controllers can also suffer from steady state error. The integral of the error, taken over all time, is multiplied by the integral gain (K_I). This term is used to reject steady-state errors. Although too large a K_I often results in overshoot and oscillation. Finally, derivative gain (K_D) regulates the change in error over time and is typically used to damp out oscillations in the system. The derivative action also responds to sensor noise which makes implementation difficult. When derivative action is not used, the controller is referred to as a PI controller. The PID can be discretized using Tustin's approximation to [Franklin et al., 2010]:

$$u_k = u_{k-1} + K_P e_k + K_I \frac{T_s}{2} \left(e_k + e_{k-1}\right) + K_D \left(e_k - e_{k-1}\right) \tag{2.2}$$

Where T_s is the sample time. For a PI controller, the discretized form is:

$$u_k = u_{k-1} + K_P e_k + K_I \frac{T_s}{2} \left(e_k + e_{k-1}\right) \tag{2.3}$$

A model of the system being controlled (the plant) is required for model based control and for designing the controller offline using simulation. Two general approaches are used to get the plant model. The first approach is system identification, or "black-box modelling", where the system order and parameters are unknown. An input, that persistently excites the dynamics of interest, forces the plant through the input and the output is measured. A model is then approximated from the intput/output data using statistical methods [Ljung, 1999]. Another approach is physics-based modeling, where the governing equations to the system are combined and sometimes approximated to achieve an input-output model directly from the physics involved. It is possible to combine the two approaches. For example when using system identification, if the physical structure of the system is known, the physical parameters can be estimated using experimental results.

To incorporate knowledge of the system being controlled and knowledge of constraints a more complex controller, Model Predictive Control (MPC), is used. In MPC, the controller uses a model to propagate the system dynamics forward in time for two time horizons: the first is the prediction horizon, where the model is used to predict the system's output up to the horizon; the second is the control horizon, usually smaller than the prediction horizon, where the controller calculates a set of control inputs and evaluates the response with the model. However, the controller outputs the calculated input from the model into the plant for only the current cycle and then repeats this process each sample time. These types of controllers are often implemented in systems with state and input constraints but require a slow process due to computational overhead. If the model is computationally simple enough it can be implemented at faster sample rates such as in combustion engines [Camacho and Bordons, 2004].

2.5 Combustion Metrics

The combustion metric that is used as controller feedback in this thesis is the crank angle where 50% of the mixture mass fraction is burned, denoted CA50. Since CA50 incorporates both start of combustion (SOC) and the burn duration, it is considered a good indicator of combustion timing in the engine. [Agrell et al., 2003a] uses CA50 as a control input for the feedback controller developed. [Lundstrom, 2006] also uses CA50 as a control and model input, stating that SOC is more difficult to accurately measure. [Bengtsson et al., 2006] quotes CA50 as a reliable source of combustion timing for the use of feedback for control purposes. SOC and crank angle of peak pressure have also been used [Shaver et al., 2004].

CA50 is defined as the crank angle degree after top dead centre (aTDC) that 50% of the air/fuel mixture is burned and is found by finding the CAD location where 50% of the heat from the mixture has been released. Cylinder pressure must be measured as a function of crank angle. To do this, first the heat release rate as a function of CAD is determined as [Heywood, 1988]:

$$\frac{dQ(\theta)}{d\theta} = \frac{\gamma(i)}{\gamma(i)-1} P(i) \frac{dV(i)}{d\theta} + \frac{1}{\gamma(i)-1} V(i) \frac{dP(i)}{d\theta} \tag{2.4}$$

where $P(i)$ and $V(i)$ are the measured pressure and calculated volume traces, respectively. This equation for the heat release rate calculates the heat released through work only, and neglects heat transfer and other inefficiencies. The ratio of specific heats is:

$$\gamma(\theta) = \frac{C_p(\theta)}{C_p(\theta) - R_U} \tag{2.5}$$

where $C_p(\theta)$ is the constant pressure heat capacity at the in-cylinder temperature at crank angle θ, and R_U is the universal gas constant ($8.314 \frac{\mathrm{kJ}}{\mathrm{kmol\ K}}$). The specific heat at a constant volume is replaced using Mayer's relation $C_p - C_v = R_U$. The integration of Equation (2.4) over all of the sampling points gives the total heat release Q_{Total}, whereas the integration up to a certain CAD gives the cumulative heat released,

$Q_{Net}(\theta)$. To find the heat release percentages the formula is used:

$$HR_{\%} = \frac{Q_{Net}(\theta)}{Q_{Total}} \cdot 100 \tag{2.6}$$

The crank angle where $HR_{\%}$ is equal to 50 is considered CA50. Burn duration is defined as the difference between the crank angles where $HR_{\%}$ is equal to 90 and 10. One way to define SOC is when the third derivative of the pressure trace surpasses a certain limit [Ghazimirsaied, 2012] [Ghazimirsaied and Koch, 2012]. These metrics are shown in Figure 2.5.

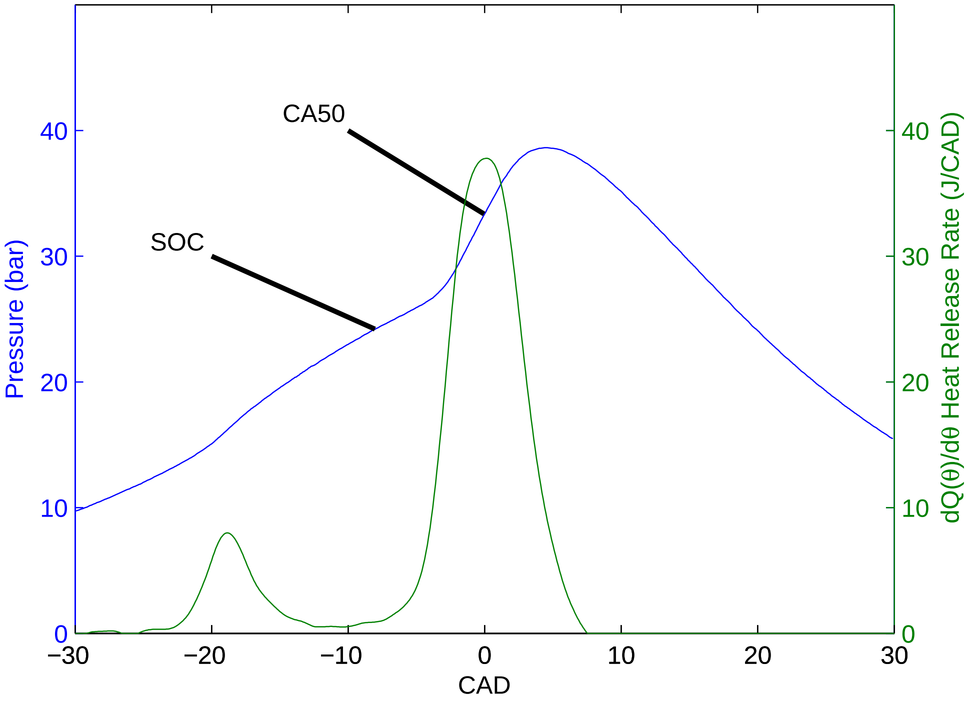

Figure 2.5: Combustion metrics displayed with a common pressure trace.

HCCI engine operation is limited by knock at the high load end and misfire at the low load end [Atkins, 2004] [Ghazimirsaied, 2012] [Ghazimirsaied and Koch, 2012]. In this thesis, HCCI misfire is defined when the air/fuel mixture fails to auto-ignite completely, resulting in a lower indicated mean effective pressure (IMEP). A covariance in IMEP larger than 5% is deemed to be the misfire limit [Audet, 2008] [Audet and Koch, 2009] [Lupul, 2008] [Weall et al., 2012].

Engine knock in HCCI combustion must be distinguished from engine knock in standard SI combustion. In SI, knock is defined as autoignition of the unburned mixture ahead of the propogating flame [Heywood, 1988], which causes damaging oscillating pressure waves inside the cylinder. In HCCI autoignition is standard in each cycle, and knock is caused by inhomogeneity within the mixture, such as lambda (ratio of actual air and stoichiometricly required air), residual fraction or temperature, which causes variation in combustion autoignition, resulting in pressure oscillations [Mashkournia et al., 2011]. Currently there is no universally accepted metric for knock detection in HCCI, but [Atkins, 2004] outlines a few different metrics, including a simple knock amplitude method, a pressure rise rate method, and a method using a bandpass filter and root mean squares. In this study, the knock limit is determined heuristically using the audible signal. The pressure rise rate of this audible signal agrees with previous literature. [Atkins, 2004] quotes a value of 10 bar/CAD as a knock limit, whereas Lupul [2008] uses a value as 7 bar/CAD. In this study, the $\frac{dP}{d\theta}$ knock limits as a function of fuel rate and NVO are shown in Figure 2.6. They are in a range from 5 to 10 bar/CAD, agreeing with the previous literature. The knocking cases are listed in Table 2.1, and four lower fuelling rates along with the knocking case for each point are plotted to show the reduction in the knock metric as less fuel is injected.

2.6 Effects of Negative Valve Overlap on Engine Operation

A brief summary of research into the effects of different valve strategies on HCCI operation is presented in this section.

The control of HCCI using internal EGR, and the potential elimination of high

Knock Case	NVO (CAD)	Maximum Fuelling Rate (kJ per cycle)	1 Step Below (kJ per cycle)	2 Steps Below (kJ per cycle)	3 Steps Below (kJ per cycle)	4 Steps Below (kJ per cycle)
1	0	0.5552	0.5366	0.5159	0.4953	0.4766
2	20	0.5366	0.5159	0.4953	0.4766	0.4560
3	40	0.5366	0.5159	0.4953	0.4766	0.4560
4	60	0.5366	0.5159	0.4953	0.4766	0.4560
5	80	0.4953	0.4766	0.4560	0.4374	0.4167
6	100	0.4766	0.4560	0.4374	0.4167	0.3960
7	120	0.4953	0.4766	0.4560	0.4374	0.4167
8	140	0.4808	0.4518	0.4208	0.3919	0.3629
9	160	0.4415	0.4167	0.3877	0.3567	0.3278
10	180	0.4415	0.4311	0.4022	0.3712	0.3422
11	200	0.4167	0.4063	0.3774	0.3464	0.3174

Table 2.1: Knock cases corresponding to Figure 2.6.

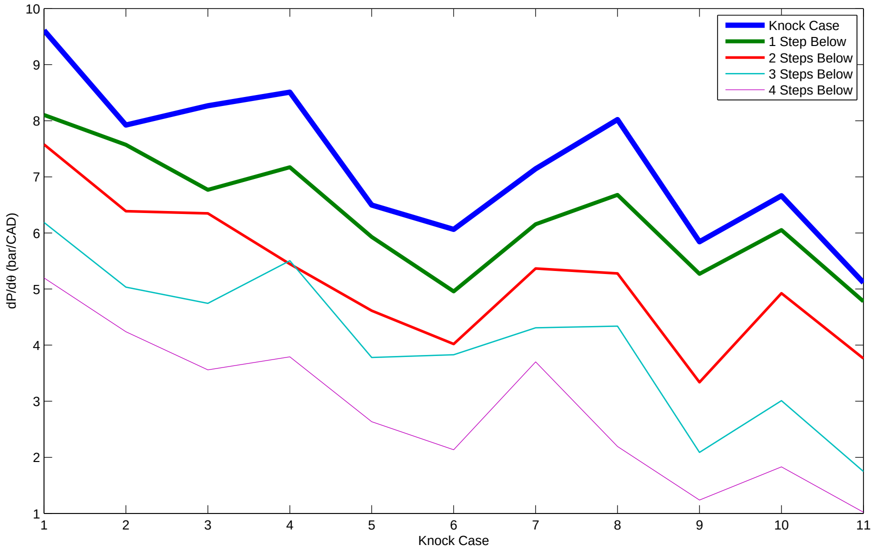

Figure 2.6: $dP/d\theta$ for knocking case and four lower levels of fuelling. Each fuel step is listed in Table 2.1.

intake temperature pre-heating is investigated in [Law et al., 2001]. Exhaust retention (NVO) and exhaust re-induction (re-breathing) are examined and both are found to be similar and have better combustion stability than SI operation. This study a pioneering study into controlling HCCI combustion timing using internal EGR.

The effects of NVO on HCCI combustion including speed-load maps and a comparison between SI and HCCI is described in [Allen and Law, 2002]. The study quotes lower emissions (except hydrocarbons in extreme HCCI conditions) and better fuel efficiency. The study confirms that HCCI is a viable option for part-load conditions, but HCCI does not have a large load range when compared to SI.

NVO and modelling to find a required thermal threshold for autoignition of the air/fuel mixture in HCCI is studied in [Chen et al., 2003]. Different levels of internal EGR through NVO and its effects on engine metrics such as combustion timing, exhaust temperature and exhaust emissions are examined.

[Caton et al., 2005] looks at re-induction (re-breathing) versus retention (NVO) strategies for controlling HCCI combustion. The main focus is on different styles of reinduction control, such as valve timing, lift or duration control of the intake valve, and how it effects combustion metrics. The study goes on to compare a re-induction strategy with a NVO strategy and cites higher efficiency by approximately 5% with re-induction, but also higher emissions.

The effects of NVO and internal EGR on HCCI combustion at three different valve overlaps and at different speeds and loads is reported in [Shi et al., 2006]. The goal of the study is to expand the high load region of HCCI combustion, where an advanced SOC is undesirable. It is found that while internal EGR introduces positive effects such as improved homogeneity and lower emissions, the heat introduced through internal residual advances SOC too far and results in a lower load limit.

The effects of valve timing and pilot direct injection on the combustion metrics of a single cylinder engine is experimentally examined in [Weall et al., 2012]. The main focus is the extension to low loads of HCCI operation using different direct injection fuelling techniques. An investigation into NVO duration's effect is also performed.

2.7 HCCI Timing Control with Variable Valve Timing (VVT)

Previous work on HCCI timing control is briefly summarized in this section. The main focus is control using variable valve trains, ie. NVO, but other control methods such as dual fuels and fast thermal management are also discussed.

[Agrell et al., 2003a] shows the use of NVO can be used to control ignition timing in HCCI engines. They use a fully variable valve train changing NVO or IVC timings to control combustion timing. This demonstrates that the use of variable valve timing can be used to affect the in-cylinder temperature by controlling residual gas amounts, which in turn directly effects combustion timing. A PI controller similar to the one presented in this study is also implemented.

[Shaver et al., 2004] went further and develops a simple non-linear physics based model for controller design which includes simplified models for the intake, compression, combustion, expansion and exhaust. The controller uses volume and pressure at peak pressure as set points and the controller outputs a desired molar ratio of residual gases and volume at IVC. These values are used in a valve timing map to obtain the desired inputs into valve timings for NVO and IVC.

[Lundstrom, 2006] develops a black-box modeling controller. Using white noise inputs on NVO and IVC at different operating points, six different Output Error models are developed. Using these models, controllers are designed using both pole placement and loop shaping and a switching method between controllers for different operating points (similar to gain scheduling) is used.

Using system identification for models and the MATLAB MPC toolbox, [Bengtsson et al., 2006] compares two different control actuators: IVC timing and dual fuel control. The study concludes that the IVC controller can operate in a larger region with less constraints. An MPC controller is successfully implemented with both actuators on a six cylinder engine.

A controller using loop shaping is developed in [Bögemann, 2009]. The control actuator is re-breathing lift where the exhaust valve is re-opened during the intake stroke to a controlled lift and constant timing. This is similar to NVO in that the controlled actuator directly effects combustion residual gases in the cylinder at IVC.

Another model based control is used in [Widd, 2009]. Based on a detailed non-linear physical modelling of the process, multiple linearized models are derived from the non-linear one and implemented in a Linear Varying Parameter model using MPC. The controller actuators chosen are intake temperature and IVC. Subsequently, [Widd et al., 2011] uses EVC timing as an actuator to compare linear quadratic (LQ) control and MPC controllers. The models required for the MPC control are physics based.

A simple physical model is used to design a controller to reduce combustion instability using valve timing in [Jungkunz, 2013]. A combustion timing controller is also designed using fuelling strategies such as pilot injection timing and main injection timing as inputs.

2.8 Work in This Study

This study conducts a further investigation into the effects of valve timing on HCCI combustion characteristics from those found in Section 2.6. An extensive array of valve timings and loads, along with multiple strategies are investigated using a production relevant EVVT system. The system allows instant cycle-by-cycle valve timing variation without the bulk and setup associated with similar performing systems. This also allows the implementation of faster controllers. The ground work is laid for controller development using this system, and several controllers are implemented similar to those found in Section 2.7.

Chapter 3

Experimental Setup

3.1 Engine Assembly

The single cylinder engine used in this thesis has the same lower block as described in [Lupul, 2008], [Audet, 2008] and [Audet and Koch, 2009], and consists of a Ricardo Hydra Mark III block, a Ricardo crankshaft, a custom Carillo connecting rod, a custom Diamond piston, a custom Darton Industries Inc. wet sleeve cylinder and research EVVT head fitted by [Mashkournia, 2012]. The cylinder jug can be adjusted to change the compression ratio of the engine, and in these tests the compression ratio is fixed at 13.9 to 1. The piston is custom made with large valve recesses to allow for free running of the engine, as shown in Figure 3.1. The EVVT setup (discussed later in Section 3.3) allows for fully independent and adjustable valve timings. A picture of the engine assembly is shown in Figure 3.2. The specifications of the engine assembly are found in Table 3.1. To reduce engine vibrations transmitted to the dynamometer, a shaft with two flexible couplings is used.

The dynamometer used is an active type consisting of a 37 kW DC motor with a Eurotherm Drive 590+ drive controller in speed control mode. An Interface Inc. SSMA-A-J-200N load cell mounted on the dynamometer is used to measure the torque. The dynamometer, supercharger, DC motor and air plenum are shown in

Figure 3.1: 97mm diameter piston crown used with the EVVT valves.

Parameters	Values
Bore × Stroke [mm]	97 × 88.9
Compression Ratio	13.9
Displacement [L]	0.653
Valves (used)	2
Intake Valve Diameter [mm]	36
Exhaust Valve Diameter [mm]	24
Intake Valve Diameter [mm]	36
Exhaust Valve Diameter [mm]	24
IVO [aTDC Combustion]	-360 to -260
IVC [aTDC Combustion]	-180
EVO [aTDC Combustion]	180
EVC [aTDC Combustion]	260 to 360

Table 3.1: Specifications of the single cylinder EVVT engine assembly.

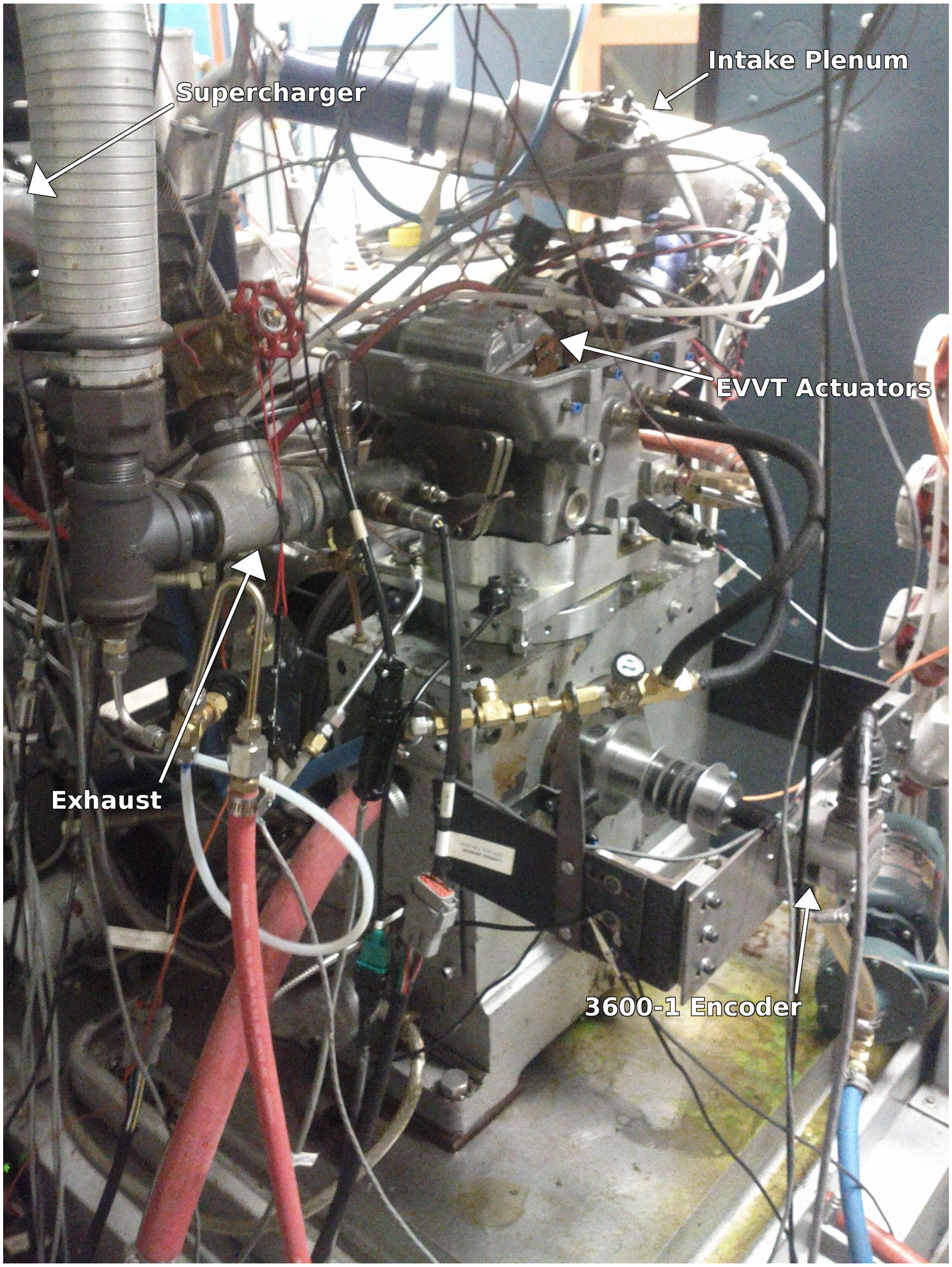

Figure 3.2: Photograph of the engine block assembly.

Figure 3.3.

The complete engine test setup, including the measurement outputs and control inputs is schematically depicted in Figure 3.4. Air enters the system through a laminar flow meter and then enters a large air plenum. It then passes through the electronically controlled throttle. It passes through a roots-type supercharger (Eaton Automotive MP45) which is driven by a variable speed electric drive that allows computer control of boost. In this study no supercharger boost is used. The air then goes through an intake air heater and is heated to 80 °C. Two independent port fuel injectors provide the fuel. One fuel injector injects n-heptane fuel and one iso-octane. This is what allows cycle-by-cycle octane level control. Fuel flow rate is measured only on the n-heptane side using a coriolis meter (Pierburg PLU4000), which a pulse width calibration is used for n-heptane (calibration on a flow bench with an R^2 value of 0.99 [Audet, 2008] [Audet and Koch, 2009]). On the exhaust side, the external EGR loop is controlled by an EGR valve which always remained closed in this study. There is also the emissions bench sample extraction and five gas (hydrocarbons, O_2, CO, CO_2 and NO_x) analyzers.

3.2 dSpace MicroAutobox

A dSpace microautobox is used for the engine controller. It consists of a dSpace model ds1401 computer connected to custom power electronics. The controller is designed with MATLAB Simulink® and is used to set the valve timing, fuelling amount of each injector (and thus octane), and spark timing (not used here). The computer runs these tasks at a rate of 1000Hz, and calculates the next cycles fuel injector pulse widths during the current cycle's intake stroke. The MicroAutobox receives a crank angle position signal from a hall sensor and a 36-1 toothed wheel on the crank shaft. As this engine has electromagnetic valves there is no camshaft. To define combustion

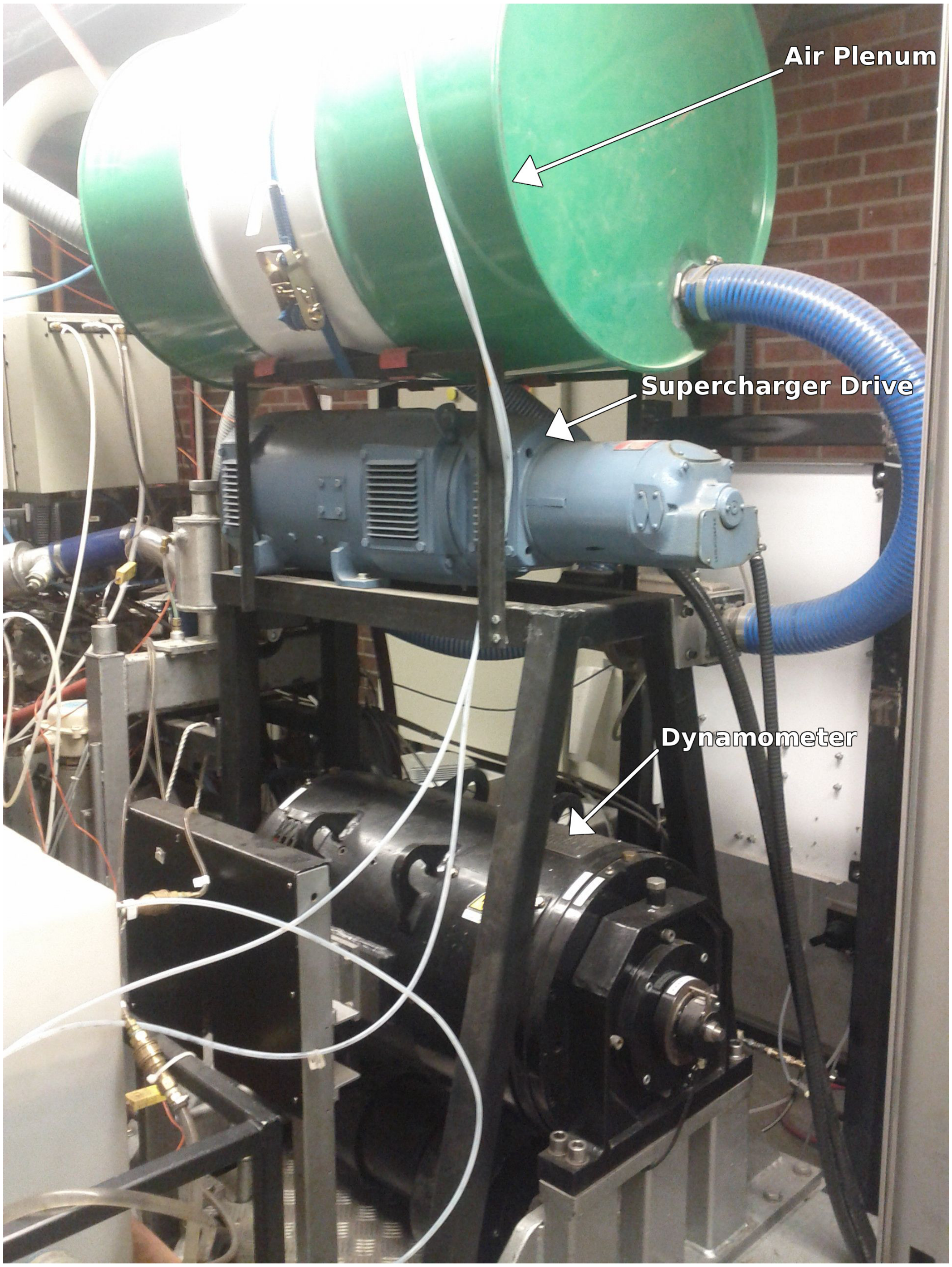

Figure 3.3: Photograph of the engine dynamometer, air plenum and supercharger drive.

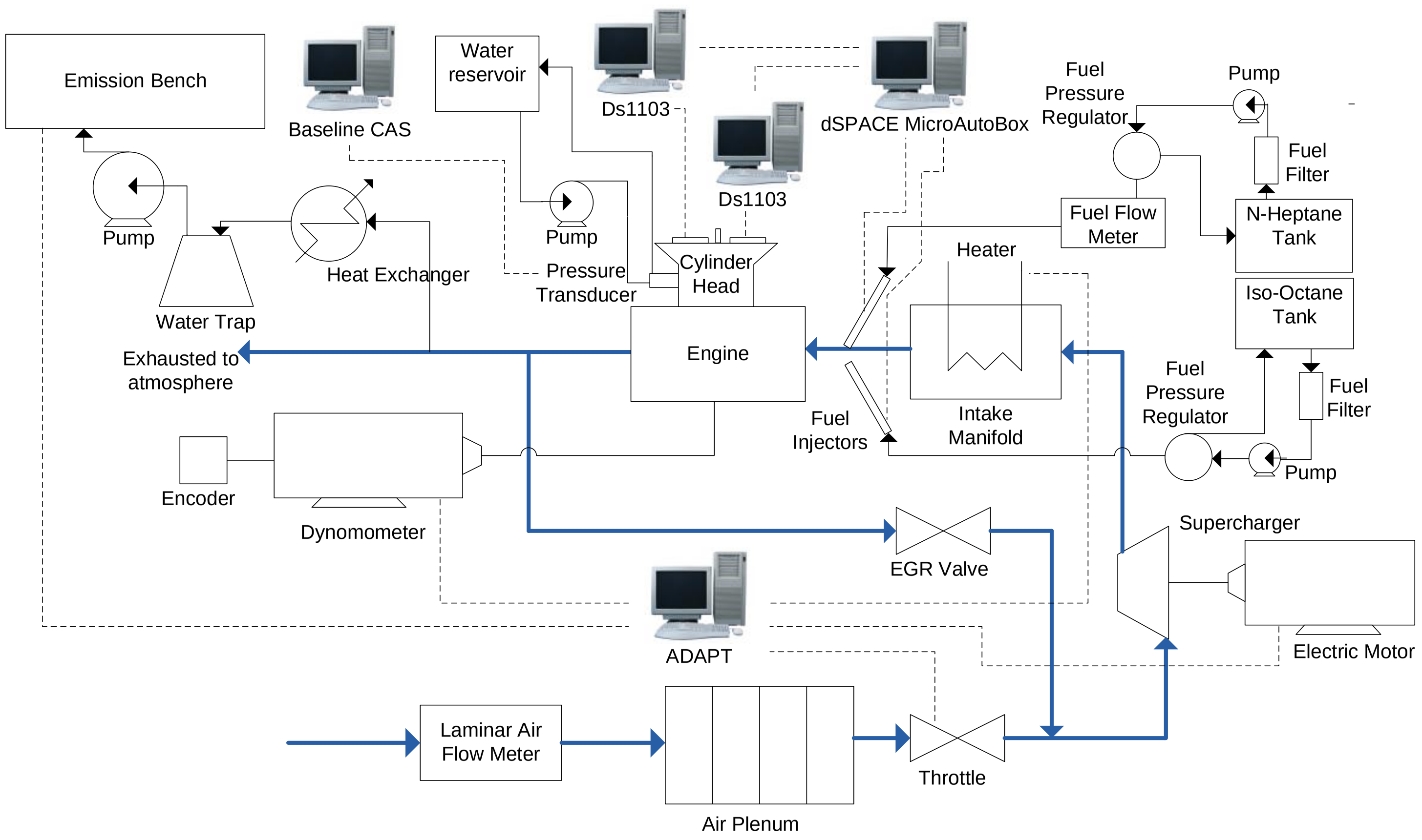

Figure 3.4: Engine Schematic

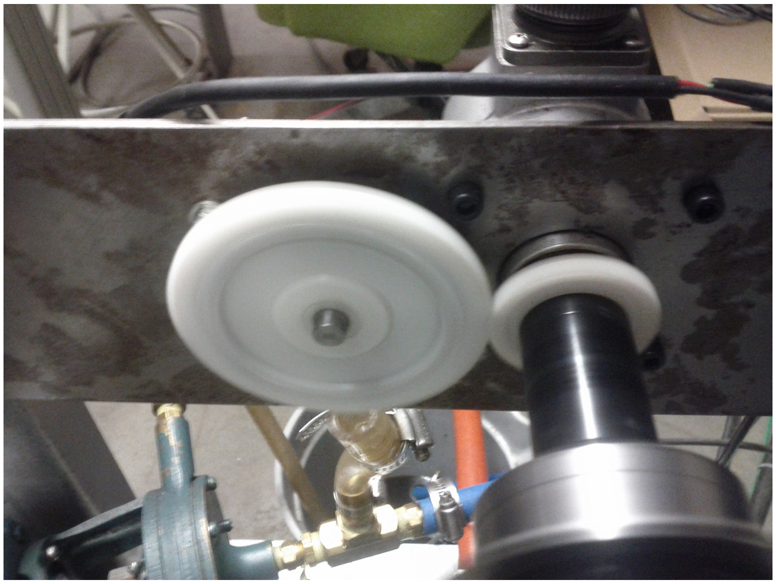

Figure 3.5: Photograph of the cam encoder gear setup.

TDC for the dSpace engine control a cam signal is generated using a 2:1 gear reduction and a hall sensor as shown in Figure 3.5. The dSpace system also receives sensor data and combustion metrics from both Adapt and CAS (Section 3.4) at a rate of 100Hz to help with controller design and actuation. All data from this system is logged on a per-cycle basis. A screenshot of the dSpace control desk user interface for engine control is shown in Figure 3.6, and the system computer can be seen on the left of Figure 3.7.

The Microautobox is the system used for feedback control of combustion timing in this study. A CA50 signal is fed from the CAS system (see Section 3.4) into the Microautobox via an A/D converter. The Microautobox then sets valve timing according to the controller and feeds those as triggers to the ds1103 valve controllers (see Section 3.3).

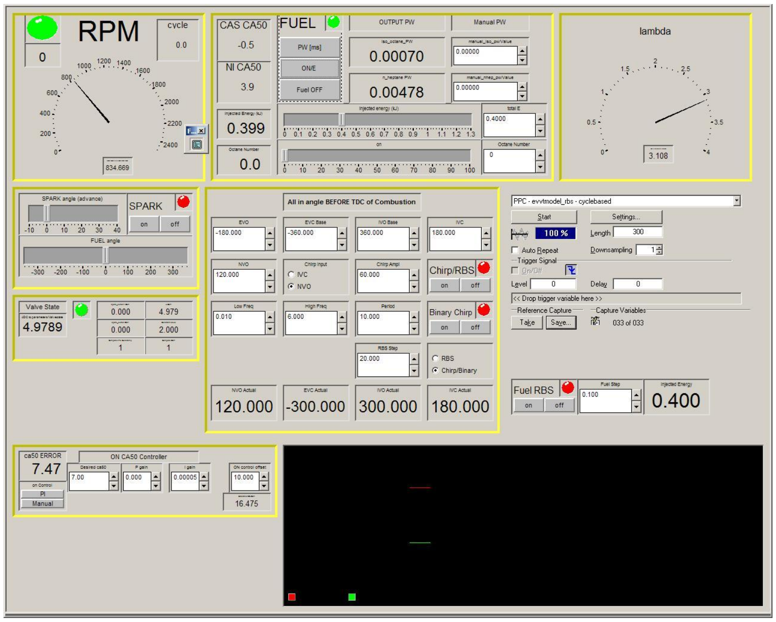

Figure 3.6: Snapshot of dSpace engine controller, RBS input model shown.

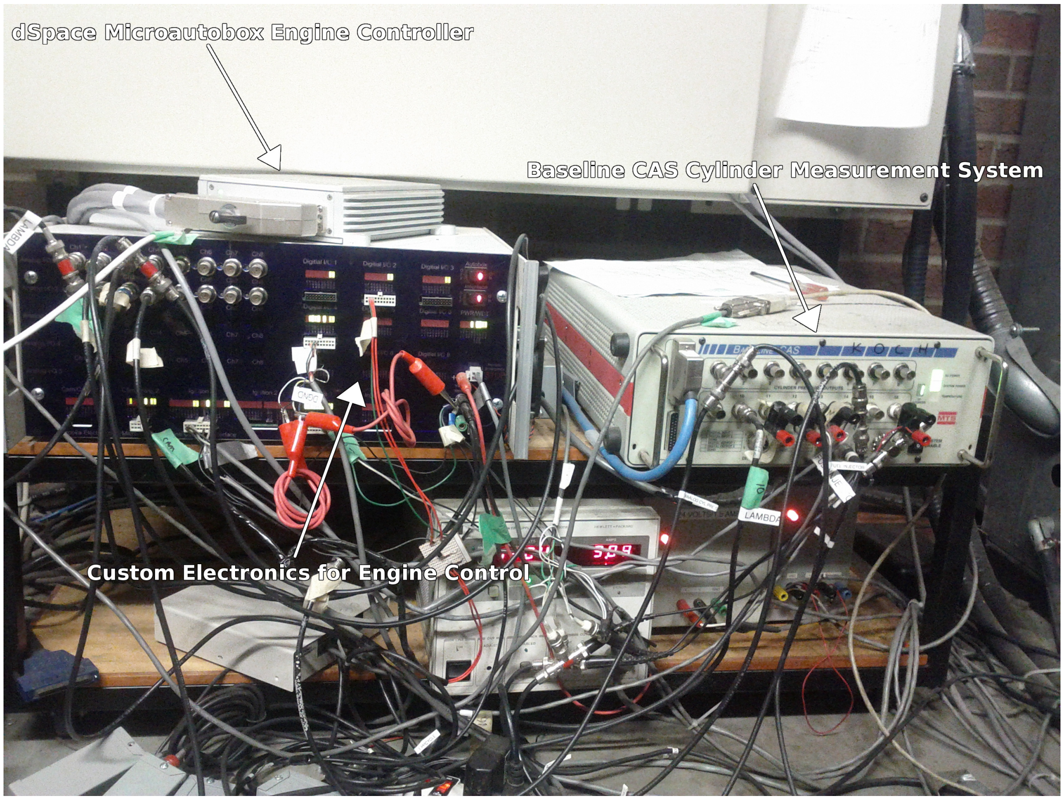

Figure 3.7: Photograph of the dSpace MicroAutobox and Baseline CAS systems.

3.3 Electromagnetic Valves

A proprietary electromagnetic system developed by Daimler AG [Stolk and Gaisberg, 2001] is used for the intake and exhaust valves. They are of the hinged actuator type shown in Figure 3.8, where a hinged armature is moved by opener and closer electromagnetic coils and springs are present which are configured so the rest position of the valve (open and closer electromagnets off) is in the middle position [Chladny et al., 2005] [Chladny and Koch, 2008] [Seethaler et al., 2013]. The engine has a four valve head and each of the 2 Daimler actuators assemblies consists of 2 valves. Since the HCCI tests in this study are at low engine speed, only one intake and one exhaust valve are active while the other two are held closed. This two valve setup is shown to have better performance at load speeds and load, as shown in [Weall et al., 2012]. The motion control and soft landing of the two valves are each controlled by two separate dSpace ds1103 processors as described in [Mashkournia, 2012] with the valve motion control in [Chladny, 2003] [Chladny et al., 2005] [Chladny and Koch, 2008] [Seethaler et al., 2013]. The valve controllers recieve opening and closing trigger timings from the dSpace microautobox engine controller.

The opening and closing timing of each EVVT valve is set independently on a cycle-to-cycle basis. This allows for cycle-to-cycle control based on measured combustion metrics using valve timing. The exhaust valve user interface is shown in the screenshot in Figures 3.9. The ds1103 controllers, valve power electronics and power supplies can be seen in Figure 3.10

3.4 Data Acquisition and Sensors

The A&D Technologies Adapt system is used for controlling the dynamometer and collecting data from all the temperature and pressure sensors, at a sampling rate of 10Hz and is shown schematically in Figure 3.12. More details of this system are given

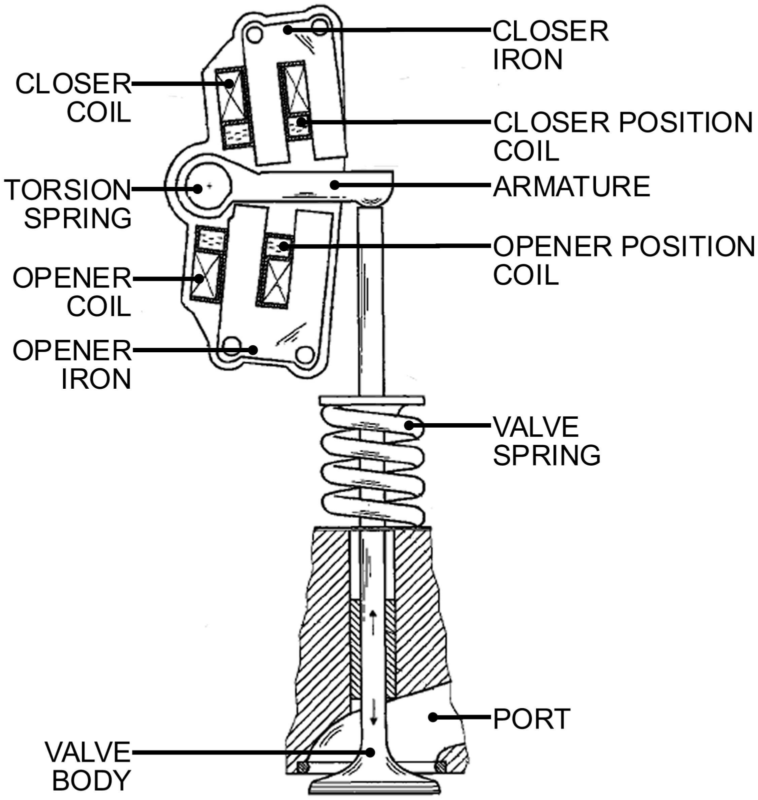

Figure 3.8: Schematic of the valve opening mechanism [Stolk and Gaisberg, 2001].

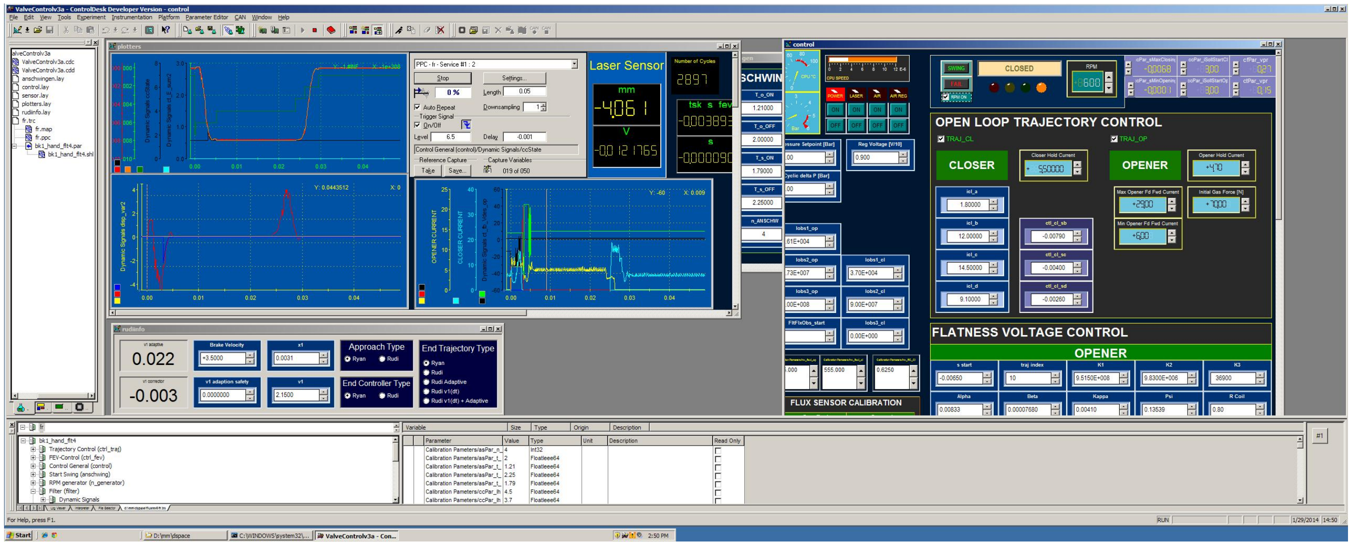

Parameter	Value	Type	Unit	Description	Read Only
Calibration Pameters/asPar_n_	4	Int32			☐
Calibration Pameters/asPar_t_	2	Floatieee64			☐
Calibration Pameters/asPar_t_	1.21	Floatieee64			☐
Calibration Pameters/asPar_t_	2.25	Floatieee64			☐
Calibration Pameters/asPar_t_	1.79	Floatieee64			☐
Calibration Pameters/ccPar_lh	4.5	Floatieee64			☐
Calibration Pameters/ccPar_lh	3.7	Floatieee64			☐

Figure 3.9: Screenshot of the exhaust valve control desk.

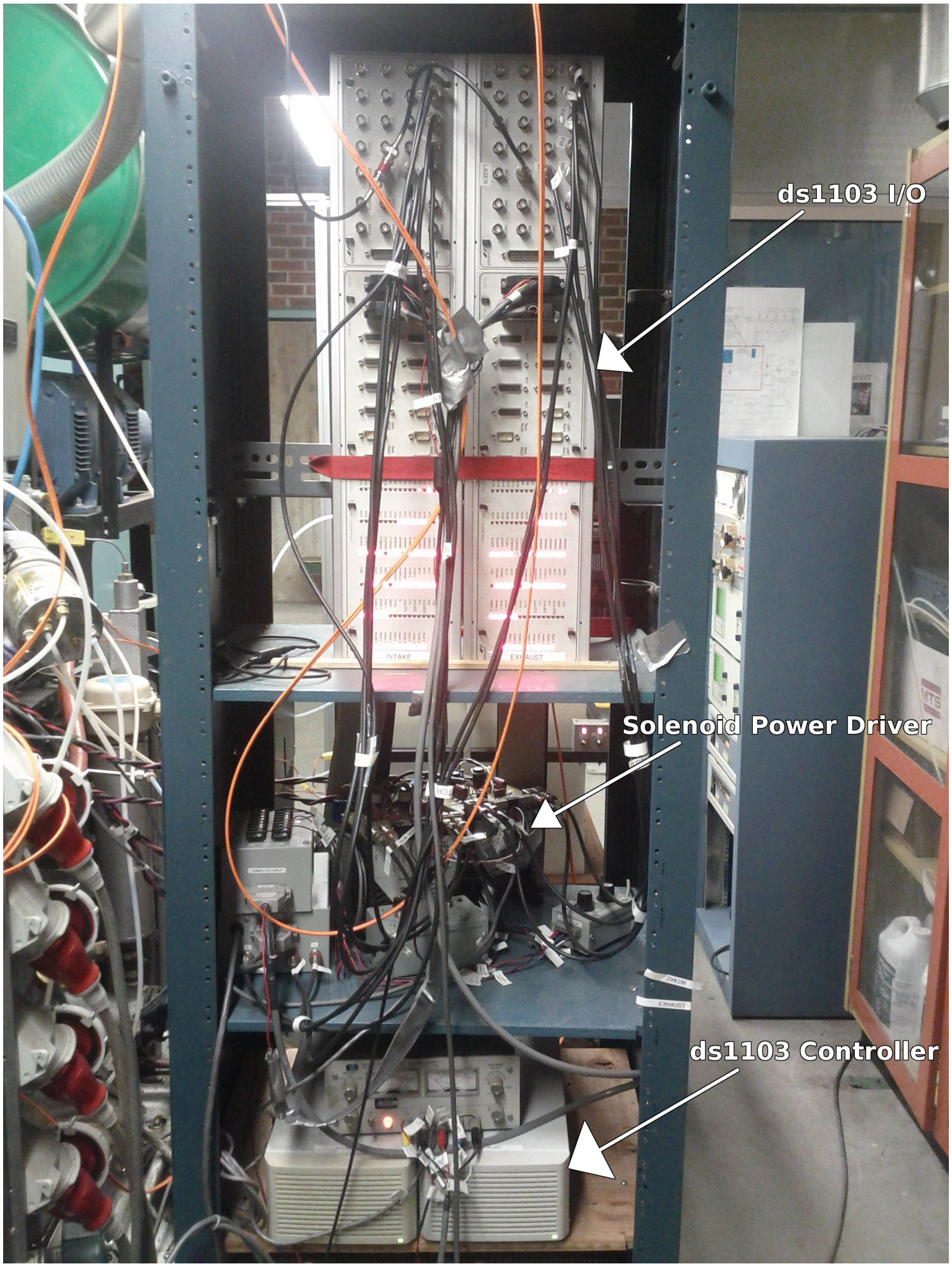

Figure 3.10: Photograph of the electromagnetic valve controllers, power electronics and power supplies.

in [Audet, 2008], [Audet and Koch, 2009] and [Lupul, 2008]. The Adapt system also controls these inputs to the engine: throttle, intake temperature, intake pressure, oil temperature, and coolant temperatures. The temperatures are measured with J and K type thermocouples, while the pressures are measured by Valedyne P305D pressure transducers. The oil and coolant temperatures are regulated by PI controllers using liquid to water heat exchangers and electric heaters for their respective fluid loops. The Adapt also communicates and collects data from the emissions bench which measures five exhaust gases. A screenshot of the Adapt system user interface is shown in Figure 3.11

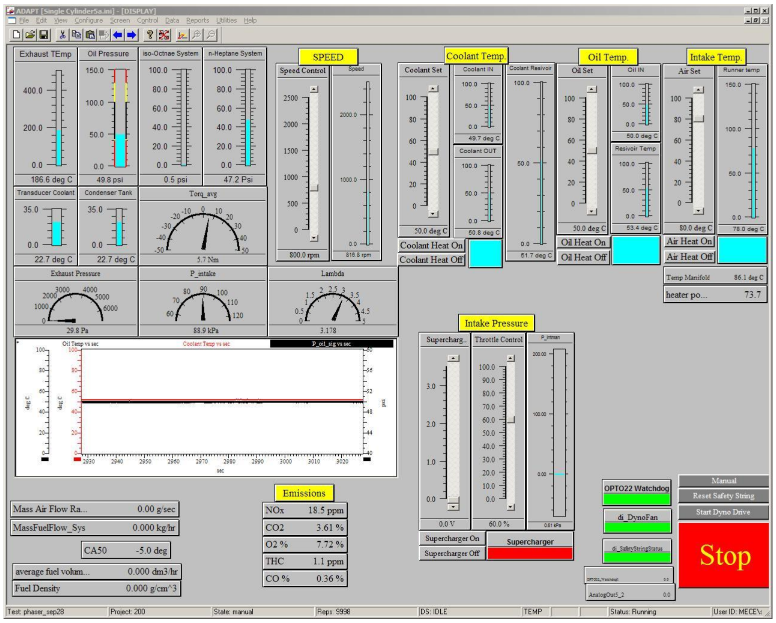

Exhaust TEmp 186.6 deg C
Oil Pressure 49.8 psi
iso-Octnae System 0.5 psi
n-Heptane System 47.2 Psi
Transducer Coolant 22.7 deg C
Condenser Tank 22.7 deg C
Torq_avg 5.7 Nm
Speed Control 800.0 rpm
Speed 816.9 rpm
Exhaust Pressure 29.8 Pa
P_intake 88.9 kPa
Lambda 3.178
Coolant Set 50.0 deg C
Coolant IN 49.7 deg C
Coolant OUT 50.8 deg C
Coolant Resivoir 51.7 deg C
Oil Set 50.0 deg C
Oil IN 50.0 deg C
Resivoir Temp 53.4 deg C
Air Set 80.0 deg C
Runner temp 78.0 deg C
Temp Manifold 86.1 deg C
heater po... 73.7
Supercharg. 0.0 V
Throttle Control 60.0 %

Mass Air Flow Ra... 0.00 g/sec
MassFuelFlow_Sys 0.000 kg/hr
CA50 -5.0 deg
average fuel volum... 0.000 dm3/hr
Fuel Density 0.000 g/cm^3

Emissions
NOx 18.5 ppm
CO2 3.61 %
O2 % 7.72 %
THC 1.1 ppm
CO % 0.36 %

Test: phaser_sep28 | Project: 200 | State: manual | Reps: 9998 | DS: IDLE | TEMP | Status: Running | User ID: MECE\

Figure 3.11: A screenshot of the A&D Technologies Adapt user interface. Main screen to control the engine and dynamometer is shown. Not shown is the emissions screen, fuel measurement screen, digital I/O screen or temperature plots screen.

An emissions bench that consists of five gas analyzers that measure the amounts of CO, CO_2, O_2, NO_x and hydrocarbons in the sample gas stream and communicates the results to the Adapt system via an D/A link. The stream can be switched between the exhaust side or the intake side (to measure external EGR) of the engine. In this study only the exhaust side is measured. The sample gas is pumped through a water

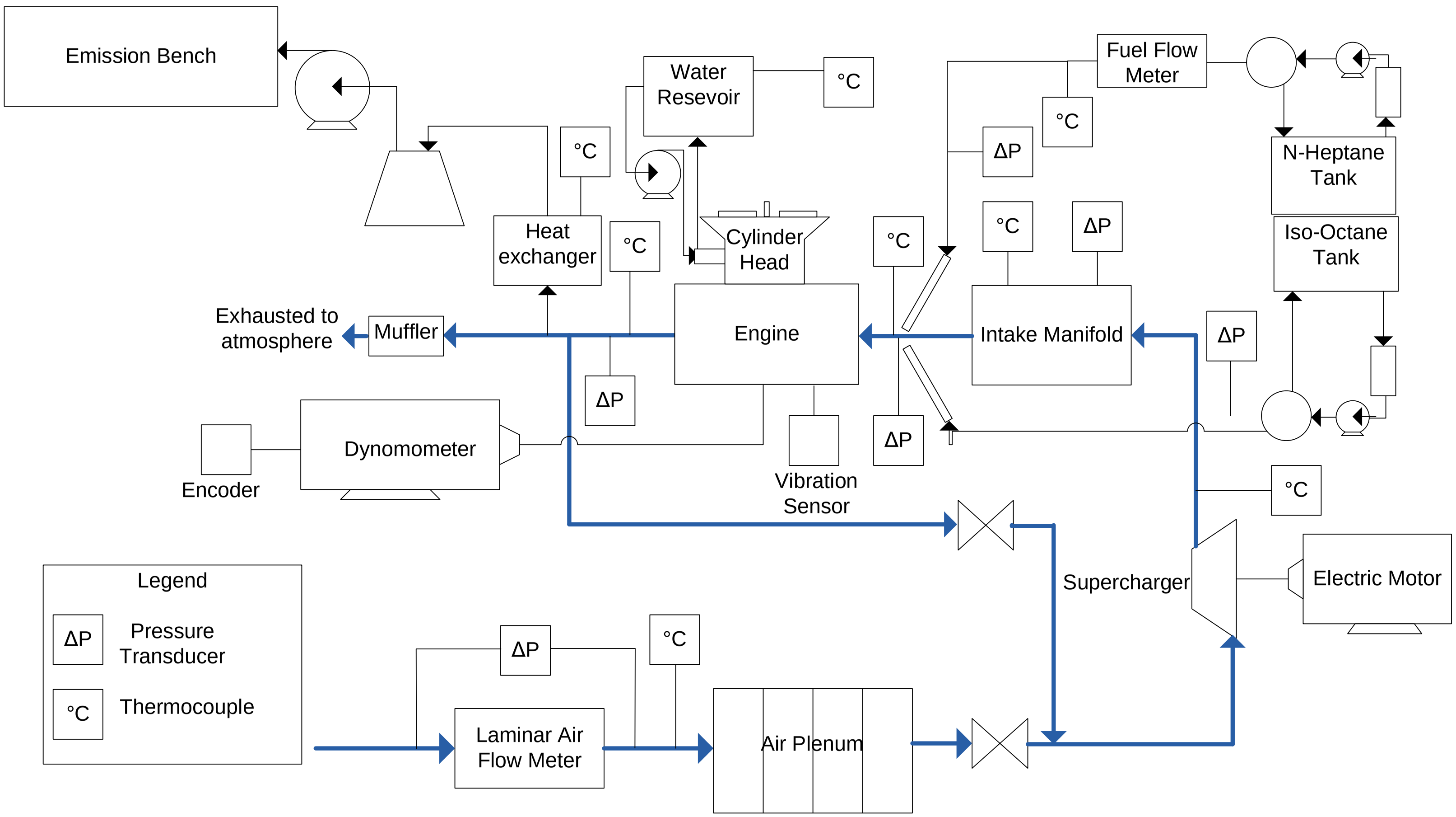

Figure 3.12: Single Cylinder Engine and Dynamometer Schematic

trap to cool and condense any water vapour and then flows through the analyzers. A schematic of the system is shown in Figure 3.13. The bench is shown in Figure 3.14.

To measure and record in-cylinder pressure, the A&D Baseline CAS system and an in-cylinder pressure transducer are used. The pressure transducer is a water cooled Kistler 6061B piezoelectric sensor mounted in the cylinder head. The transducer is connected to a charge amplifier to amplify the signal before being sent to the CAS system. At every engine cycle the sensor voltage is calibrated to the intake runner pressure at intake valve closing timing. This sensor is water cooled to decrease inaccuracy caused by thermal shock. The CAS system is triggered to measure based on a crank angle signal. Here a BEI Industries model XH25D-SS-3600-T2-ABZC-7272-SM18 with 3600 pulses per revolution encoder is used which results in cylinder pressure being collected every 0.1° CAD, as shown in Figure 3.15. CAS can output this data as well as many combustion metrics such as CA50, SOC and IMEP. CAS data logs on an engine cycle (two engine rotations) based frequency, 7200 per cycle for data such as the pressure trace and volume calculation, 720 per cycle for intake manifold pressure, and 1 per cycle for everything else and the output metrics. The Baseline CAS's user interface is shown in the screenshot in Figure 3.16, and the system itself is shown on the right side of Figure 3.7.

3.5 Experimental Uncertainty

A base steady state test under typical operation conditions is examined to determine the sampling experimental uncertainty. The base test taken has an engine speed of 817 RPM, a fuel octane of PRF0, a coolant temperature of 45 °C, a fuelling rate of 0.4 kJ injected energy per cycle and symmetric negative valve overlap of 120 degrees, or operating point C from Table 3.6. The following data is collected: dSpace microautobox for 101 engine cycles, CAS for 100 engine cycles, and Adapt for 150

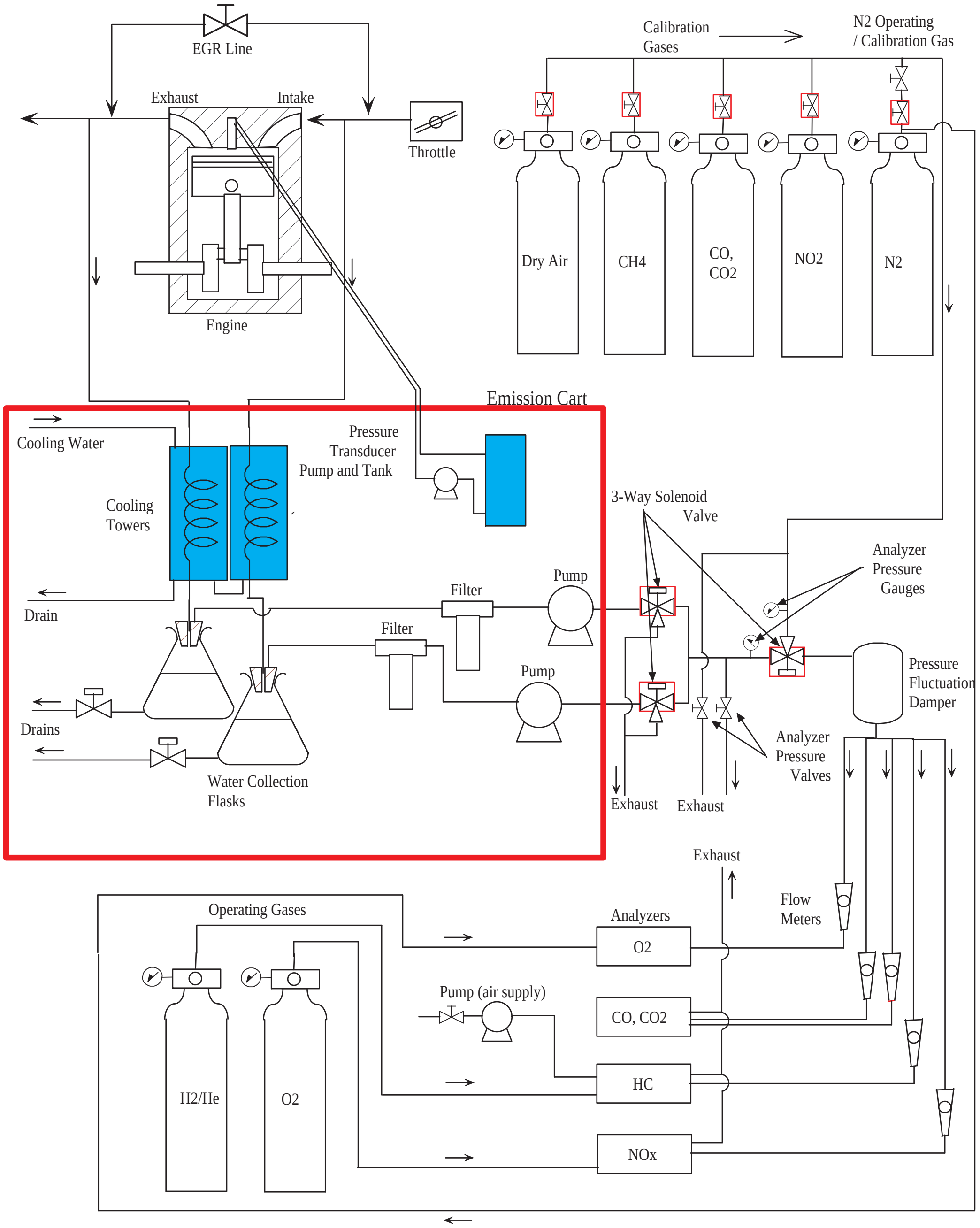

Figure 3.13: Emissions Bench Schematic

Figure 3.14: Photograph of the five emissions gas analyzers bench.

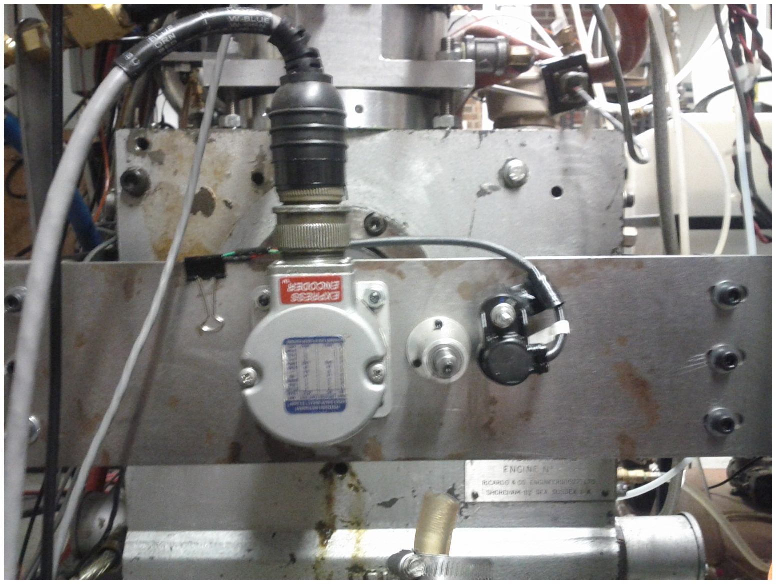

Figure 3.15: Photograph of the BEI 3600 per revolution encoder and cam encoder.

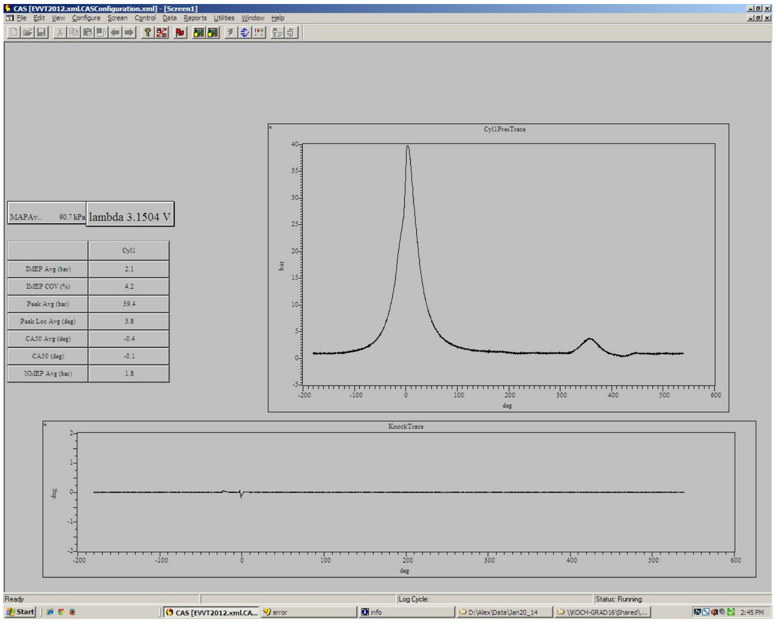

MAPAv.. 90.7 kPa

lambda 3.1504 V

	Cyl1
IMEP Avg (bar)	2.1
IMEP COV (%)	4.2
Peak Avg (bar)	39.4
Peak Loc Avg (deg)	3.8
CA50 Avg (deg)	-0.4
CA50 (deg)	-0.1
NMEP Avg (bar)	1.8

Figure 3.16: A screenshot of the Baseline CAS user interface.

samples over 15 seconds. To determine error in multiple sample tests the following equation is used [Moffat, 1988]:

$$U_{0.95} = t_{0.025} \frac{1}{\sqrt{N}} \sqrt{\frac{\sum\limits_{i=1}^{N} \left(X_i - \bar{X}\right)^2}{N-1}} \tag{3.1}$$

where $U_{0.95}$ represents the 95^{th} percentile experimental uncertainty, N is the number of samples, X_i and $\bar{X}$ are the sample and sample mean, respectively and $t_{0.025}$ is the one-tailed t-distribution value for degree of freedom ν. The degrees of freedom in a experiment is $N-1$ if N is the same for all experiments, or for multiple tests of different N [Abernethy et al., 1985]:

$$\nu = \frac{\left(\sum\limits_{i=1}^{K} \frac{S_i^2}{N}\right)^2}{\sum\limits_{i=1}^{K} \frac{S_i^4}{N^2 \nu_i}} \tag{3.2}$$

where K is the number of error sources, S_i is the variance in the current error source, N is the total number of samples, and ν_i is the degrees of freedom in the current error source. The last term in Equation (3.1) is call the root mean square, or RMS. The error in the pressure trace is calculated at every 0.1 CAD. That is for every 0.1 CAD, the 100 measured pressure cycles are averaged at each crank angle location (3600 per revolution) and RMS is calculated (see Figure 3.17). The largest RMS of 1.3 bar is used in the error calculation, located at 1.3 CAD aTDC for this test.

To determine the uncertainty when repeating a test at the same test conditions (engine inputs held constant) but on a different day, five tests are taken at the same nominal operating point on different dates. The nominal operating point is run at the start and end of tests (these are labeled as pre-test or post-test in Table 3.2). The mean values are taken from each test and an uncertainty analysis of the five is

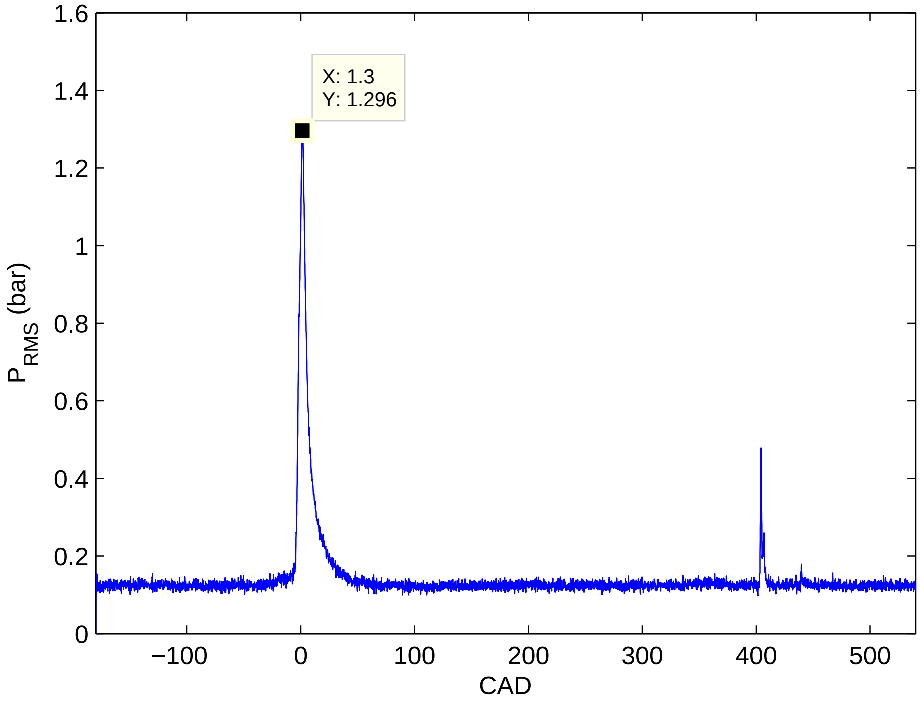

Figure 3.17: Root Mean Square residuals of the pressure trace at all crank angles in the cycle.

conducted. For cylinder pressure analysis, peak pressure is used. The resulting errors are listed in Table 3.2 and are higher than sampling error, listed in Table 3.4.

For values calculated from data, error is found using [Moffat, 1988]:

$$(U_R)_{0.95} = t_{0.025}\sqrt{\sum_{i=1}^{K}\left(\frac{\delta R(X)}{\delta X_i}S_i\right)^2} \tag{3.3}$$

where $(U_R)_{0.95}$ is the 95^th percentile uncertainty of the calculated value, K is the number of error sources in the equation, $R(X)$ is the equation to find the calculated value, X_i is the current parameter source of error and S_i is the variance in that parameter. The error involved in inputs such as fuel mass and in-cylinder volume are deemed small in comparison to larger errors such as cylinder pressure, and are neglected.

The error involved in CA50 is more complex. CA50 is the CAD location of 50% heat release. Since the resolution of the Baseline CAS system is only 0.1 CAD, the exact location of 50% heat release is limited by this resolution. The location of the first value over 50 is taken as CA50. So the error involved in this calculation is found as:

$$\delta CA50 = \frac{HR_{50\%} - 50}{\frac{dHR_{\%}}{d\theta}|_{\theta}} \tag{3.4}$$

Where $\delta CA50$ is the error in CA50, $HR_{50\%}$ is the first heat release percentage value over 50%, and $\frac{dHR_{\%}}{d\theta}|_{\theta}$ is the derivative of the heat release percentage at the location of CA50. This error is calculated for every test, and the largest error found is 3% and is listed in Table 3.3. The calculation error propagated from the pressure error using Equation (3.3) is also found, but is negligibly small compared to the truncation error.

When using Equation (3.3) on the IMEP calculation and neglecting the errors in

Value	Oct 24, 2013 Post-test	Dec 11, 2013 Pretest	Dec 11, 2013 Post-test	Dec 17, 2013 Pretest	Dec 17, 2013 Post-test	Total Uncertainty from Repeatibility
Ambient Pressure [kPa]	93.4	92.9	92.9	91.9	91.9	-
Airflow [L/min]	148	158	159	147	149	1
CA50 [CAD]	1	-1	-1	-2	-1	1
CO [%]	0.47	0.31	0.35	0.28	0.35	0.09
CO_2 [%]	3.3	4.0	3.8	3.9	3.7	0.3
IMEP [kPa]	1.8	2.2	2.0	2.1	2.0	0.1
Lambda	3.3	3.0	3.1	3.1	3.2	0.1
NO_x [ppm]	22	19	19	19	20	2
O_2 [%]	7.9	7.5	7.6	7.6	7.7	0.2
P_{Intake} [kPa]	89.6	88.1	88.3	88.7	88.8	0.7
Peak Pressure [bar]	37	41	39	41	39	2
$T_{Exhaust}$ [°C]	190	210	200	200	200	10
T_{Intake} [°C]	80.0	80.0	80.0	79.8	80.0	0.1
Hydrocarbons [ppm]	5100	3500	3500	3400	3500	900
Torque [Nm]	5.1	6.7	6.1	6.4	5.9	0.7

Table 3.2: Experimental reproducibility in values used.

cylinder volume, the resulting error equation is:

$$\delta IMEP = \frac{d}{dP}\left(\oint PdV\right)\frac{\delta P}{V_d} \tag{3.5}$$

Where $\delta IMEP$ is the error in IMEP, δP is the error in cylinder pressure, and V_d is the displaced volume of the engine. The solution to the derivative-integral combination is found to be solely dV, the step size in in-cylinder volume due to sampling at 0.1 CAD.

When Equation (3.3) is applied to the rate of pressure change formula, it is found that the resulting error equation is:

$$\delta\frac{dP}{d\theta} = \frac{d}{d\theta}(\delta P) \tag{3.6}$$

Where δP is the error found for in-cylinder pressure. The error for the rate of change of pressure is calculated for the full cycle, and the maximum is found to be 0.1 bar/CAD at 44.2 CAD aTDC of gas exchange. Note that the error found at 1.7 CAD bTDC is 0.09 bar/CAD, and is the second largest found.

Value	Uncertainty
Airflow [kg per cycle]	0.00001
BSFC [g/kWh]	4
CA50 [CAD]	0.1
Combustion Efficiency [-]	0.02
Dilution Ratio [-]	0.2
Heat Release [%]	3
IMEP [kPa]	0.2
Rate of Pressure Change [bar/CAD]	0.1
Residual Ratio [-]	0.1
Thermal Efficiency [-]	0.0005
Volumetric Efficiency [-]	0.02

Table 3.3: Experimental uncertainty in values calculated from data.

The uncertainties in the values used in this thesis are summarized in Table 3.4.

Value	Precision	Reproducibility	Bias	Total Uncertainty
Airflow [L/min]	4	1	0.5	4
CA50 [CAD]	0.08	1	0.1*	1
CO [%]	0.00003	0.09	0.02	0.09
CO_2 [%]	0.00008	0.3	0.05	0.3
Combustion Efficiency [-]	-	-	0.02*	0.02
Cylinder Pressure [bar]	0.3	2	0.5	2
Dilution Ratio [-]	-	-	0.2*	0.2
Engine Speed [RPM]	0.1	0.0003	2	2
IMEP [kPa]	0.01	0.1	0.2*	0.2
Lambda	0.004	0.1	0.04	0.1
NO_x [ppm]	0.005	2	0.1	2
O_2 [%]	0.00009	0.2	0.09	0.2
P_{Intake} [kPa]	0.1	0.7	0.5	0.9
Residual Ratio [-]	-	-	0.1*	0.1
$T_{Exhaust}$ [°C]	0.05	10	2	10
T_{Intake} [°C]	0.01	0.1	2	2
Thermal Efficiency [-]	-	-	0.0005*	0.0005
Torque [Nm]	0.05	0.7	0.008	0.7
Hydrocarbons [ppm]	100	900	30	900
Volumetric Efficiency [-]	-	-	0.02*	0.02

*from calculation error

Table 3.4: Experimental uncertainty in measured values used in this study.

3.6 Test Conditions

All test conditions are summarized in Table 3.5. Only the fuelling rate and NVO are varied from these typical base condition in these experiments. There is one experiment where the fuel is changed from PRF0 to PRF20 and this is described later. The two operating points that will distinguish between the octane numbers are listed in Table 3.6.

Variable	Type	Set	Range
Engine Speed [RPM]	Regulated	800	817 to 818
Throttle [%]	Regulated	60	60
Coolant Temperature [°C]	Regulated	50	45 to 53
Intake Temperature [°C]	Regulated	80	74 to 83
Oil Temperature [°C]	Regulated	50	50
Exhaust Temperature [°C]	Measured	-	103 to 213
Intake Pressure [kPa]	Measured	-	88 to 90
Oil Pressure [kPa]	Measured	-	372 to 384
Airflow Rate [L/min]	Measured	-	101 to 187
Lambda [-]	Measured	-	1.78 to 4.12
IMEP [bar]	Measured	-	0.03 to 2.68
Torque [Nm]	Measured	-	0 to 10.5
BSFC [g/kWh]	Measured	-	298 to 914
SOC [CAD aTDC]	Measured	-	-9.4 to -7.3
Burn Duration [CAD]	Measured	-	2.7 to 10.9
Peak Pressure [bar]	Measured	-	26.5 to 52.2
Peak Pressure Location [CAD]	Measured	-	-2.4 to 9.0
Maximum Heat Release Rate [J/CAD]	Measured	-	6.1 to 172.1
Combustion Efficiency [%]	Measured	-	10.1 to 78.6
Total Heat Release [J]	Measured	-	28.1 to 436.5
Fuelling Rate [kJ per cycle]	Input	0.28 to 0.56	-
Octane Number [PRF]	Input	0 to 20	-
IVO [aTDC Combustion]	Input	-360 to -260	-
IVC [aTDC Combustion]	Input	-180	-
EVO [aTDC Combustion]	Input	180	-
EVC [aTDC Combustion]	Input	260 to 360	-
CA50 [CAD aTDC]	Output	-	-6.0 to 8.4

Table 3.5: Engine HCCI Operation Range

Operating Point	A	B	C
Fuelling Rate [kJ per cycle]	0.28-0.56	0.34-0.49	0.4
Octane Number [PRF]	0	20	0
NVO [CAD]	0-200	0-180	120

Table 3.6: Base Engine Test Conditions

Chapter 4

Effects of NVO on HCCI Combustion

The effects of NVO on HCCI engine operation is experimentally tested and the results are described here. The data collected have NVO variation from 0 CAD to 200 CAD in 20 CAD steps and the fuel rate is varied between engine misfire and engine knock limits. Misfire is defined as the point when the IMEP covariance for 100 engine cycles surpasses 5%, and the knock limit is detected audibly. Once the data are collected and sorted, the contours for plotting are produced by cubic spline interpolation onto a regular interval. Due to the nature of cubic spline interpolation, some of the abnormalities near the edges of the contour maps do not reflect the actual behavior in the data. All the NVO test results as a function of lambda are shown in Figure 4.1 and as a function of fuelling rate in Figure 4.2. Two primary reference fuels (PRFs) are shown, n-Heptane (PRF0) and 20 octane (PRF20), and tests show that the higher octane fuel results in a smaller fuelling rate operating region of the engine.

4.1 Effects of EGR on HCCI Combustion

NVO duration predominately changes the amount of residual exhaust gases remaining in the cylinder. There are four main effects of EGR on HCCI combustion [Atkins, 2004]. The most influential effect is the residual heat used to heat the intake charge and modify charge temperature. The EGR also offers dilution effects much like a

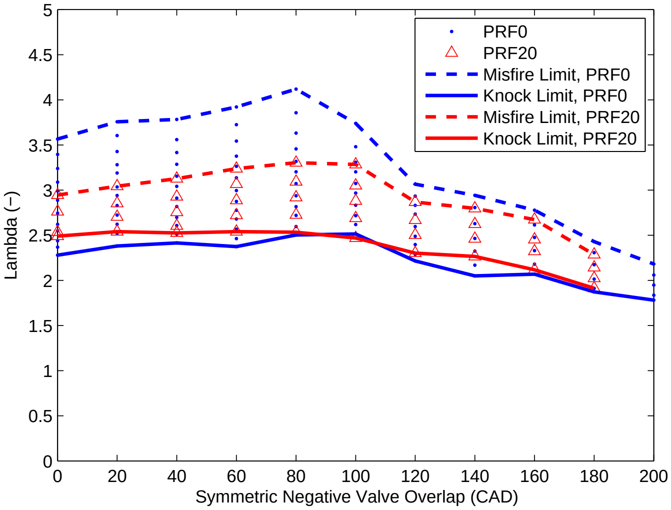

Figure 4.1: Engine operating region for PRF0 and PRF20 for SNVO versus lambda.

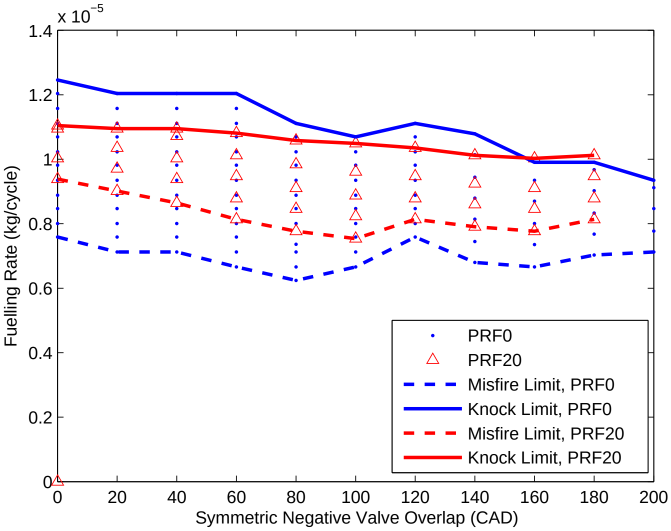

Figure 4.2: Engine operating region for PRF0 and PRF20 for SNVO versus fuelling rate.

lean air/fuel mixture, but with higher sensitivity in influencing combustion timing and duration [Atkins, 2004]. EGR also changes the mixtures thermal properties, such as specific heat. Finally, EGR introduces chemical species which can change the combustion of the air/fuel mixture due to the chemical kinetic state being changed.

4.2 Engine Operating Region for varying SNVO

To generate the experimental results, SNVO is held at a constant value near engine misfire conditions then the fuelling rate to the fuel injector is increased in steps from misfire to knock. At each fuelling rate the engine is run at steady state and data collected. Then SNVO is varied between 0 CAD and 200 CAD in 20 CAD increments and the fuelling rate is again varied. This is done for two fuels. The effect of varying SNVO on steady state HCCI engine operation is examined as a function of lambda, fuelling rate and IMEP in Figures 4.3, 4.4, and 4.5 respectively. A typical engine operating region metric is lambda [Atkins, 2004]. Figures 4.3a with PRF0 and 4.3b with PRF20 provide a basis for comparison. Comparing Figures 4.3a and 4.3b, the operating region narrows and changes location as the octance number (PRF) increases. This is a result of the higher auto-ignition tendencies found in lower octane fuels. The four effects of dilution on combustion increase as the PRF increases, therefore reducing the operating region [Atkins, 2004]. Both Figures 4.6a and 4.6b show that generally CA50 advances as SNVO increases for a constant lambda. A trend of decreasing lambda with increasing SNVO is shown in Figures 4.3 which agrees with the results in [Weall et al., 2012]. Below approximately 80 CAD of SNVO, lambda remains fairly constant, while above 80 CAD of SNVO, lambda decreases in a linear-like fashion. Above 80 CAD of SNVO large amounts of internal EGR decreases the amount of fresh intake air in the cylinder every cycle which decreases lambda. Since lambda is not a direct input in this experiment, and is correlated with SNVO,

Figure 4.3 is not an accurate representation of the engine operating region.

The engine operating range and CA50 timing contours for constant fuelling rates are shown in Figure 4.4. As fuelling rate is one of the inputs (with SNVO), Figure 4.4 directly shows the engine operating range for the two fuels. The higher PRF fuel has a smaller operating region, as shown earlier. The combustion timing, CA50, gradually advances as SNVO increases for a constant fuelling rate.

The operating range in terms of engine load (IMEP), with combustion timing (CA50) contours are shown in Figures 4.5. At constant IMEP, as SNVO is increased, CA50 initially retards and then advances. This can be attributed to the dual regions discussed in Section 4.4. At high values of SNVO, above approximately 120 CAD, the IMEP range decreases. This is attributed to the increasing internal residual, making the charge more sensitive to knock (high heat in the residual) or misfire (less fresh intake with fuel).

Since the HCCI operating point of this engine is very lean and the SNVO allows residual to remain in the cylinder, the dilution of the gas mixture is a combination of excess fresh air and residual gas. A ratio is formed in [Atkins, 2004] to calculate the amount of dilution for a given operating point, and is given as:

$$r_{Dilution} = \frac{m_{Excess\,air} + m_{Residual}}{m_{Stoich}} \tag{4.1}$$

where $m_{Excess\,air}$ is calculated using the laminar airflow meter, while $m_{Residual}$ is calculated using:

$$m_{Residual} = (\frac{1}{\eta_V} - 1)m_{Air}, \quad \forall \eta_V \leq 1 \tag{4.2}$$

Where η_V is the volumetric efficiency from the intake runner [Heywood, 1988]:

$$\eta_V = \frac{m_{Air}}{\rho_{Air} V_d} \tag{4.3}$$

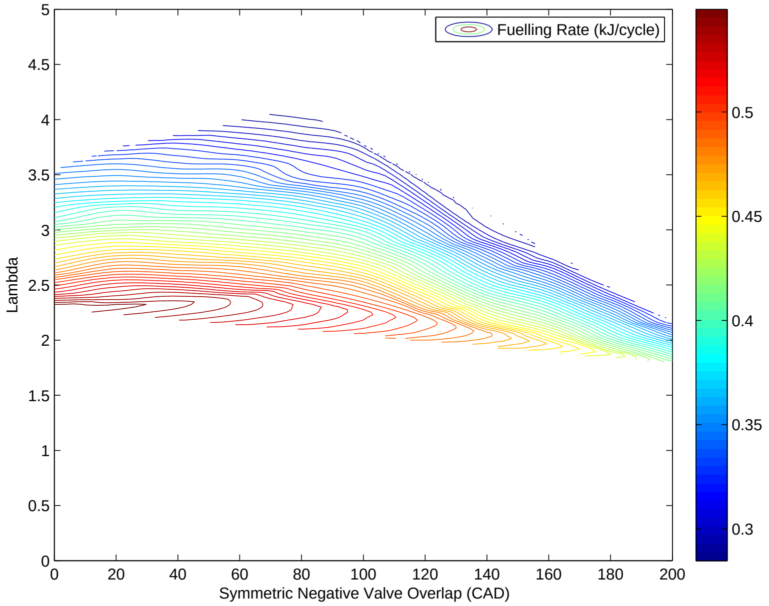

(a) PRF0

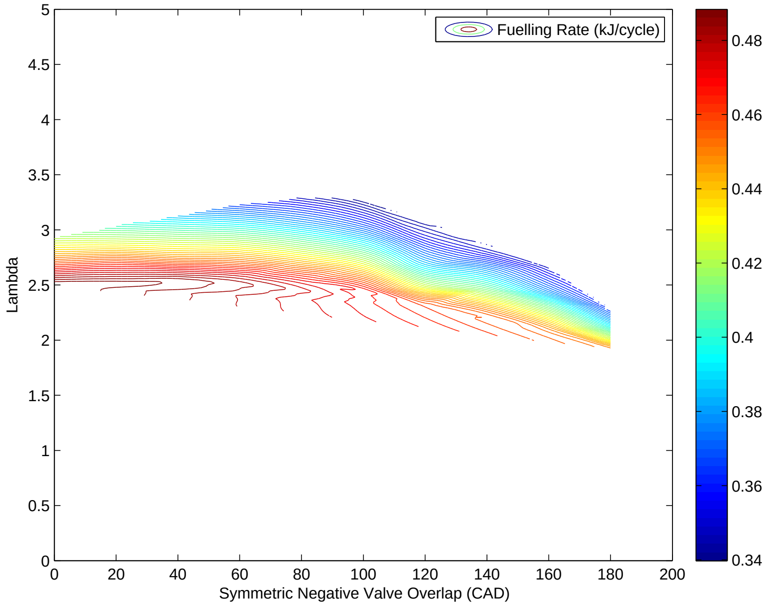

(b) PRF20

Figure 4.3: Engine operating region showing fuelling rate for SNVO versus lambda for PRF0 and PRF20.

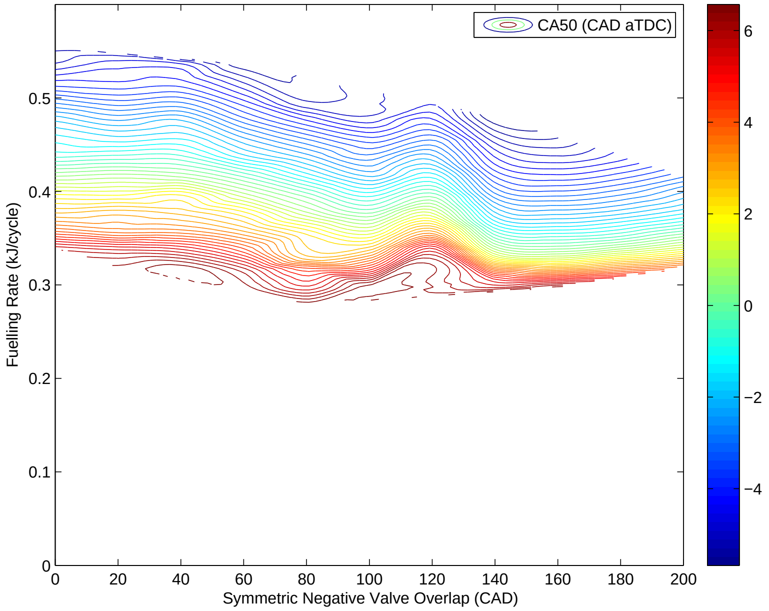

(a) PRF0

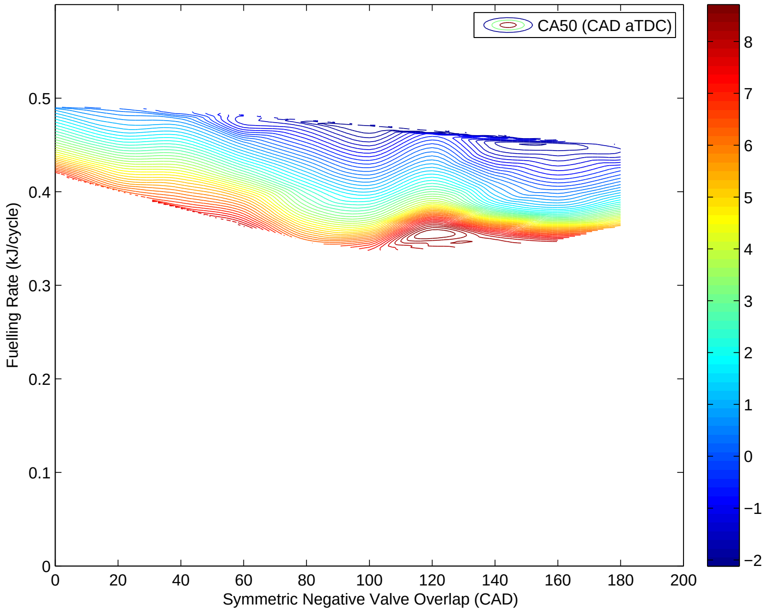

(b) PRF20

Figure 4.4: Engine operating region showing CA50 for SNVO versus fueling rate for PRF0 and PRF20.

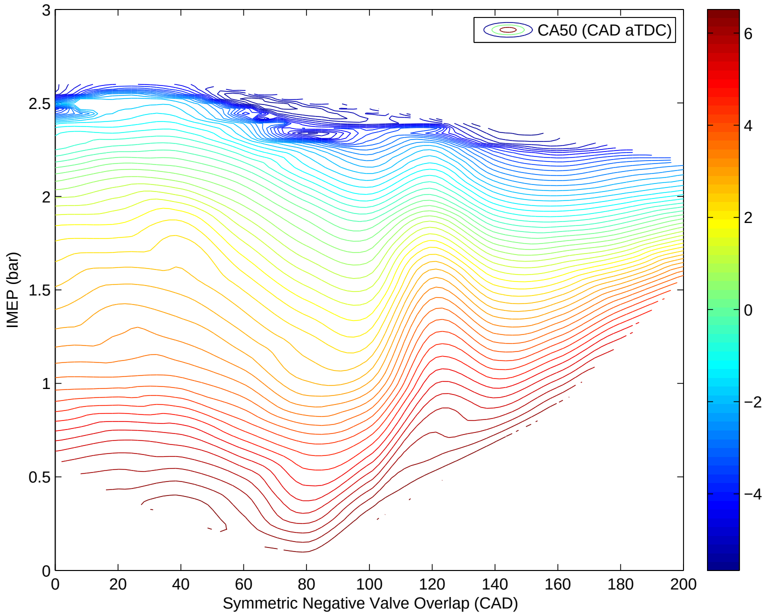

(a) PRF0

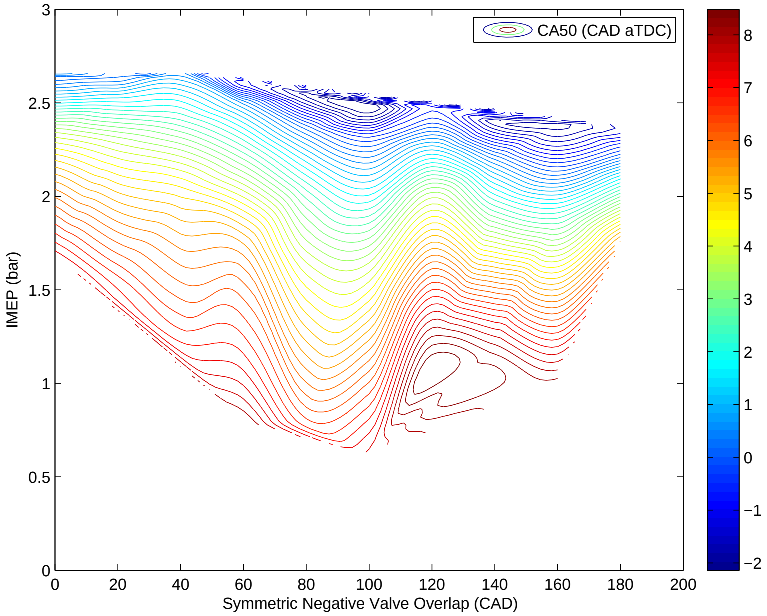

(b) PRF20

Figure 4.5: Engine operating region showing CA50 for SNVO versus IMEP for PRF0 and PRF20.

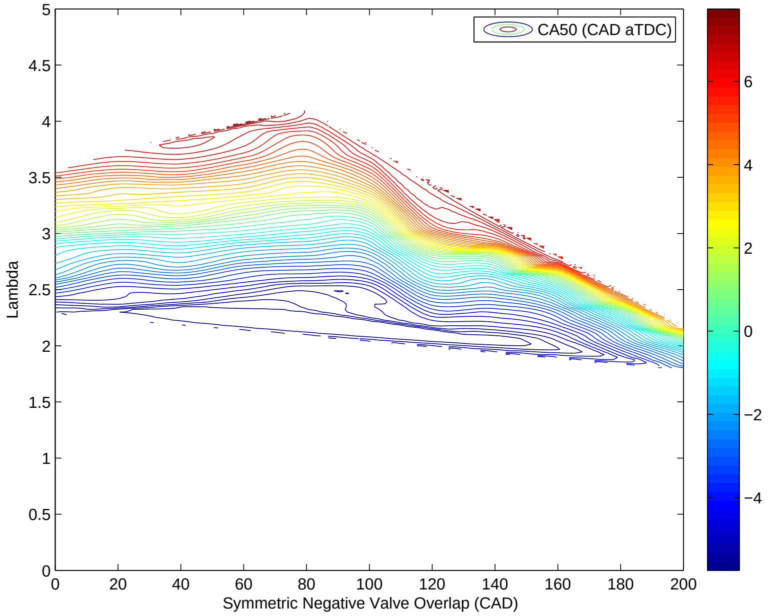

(a) PRF0

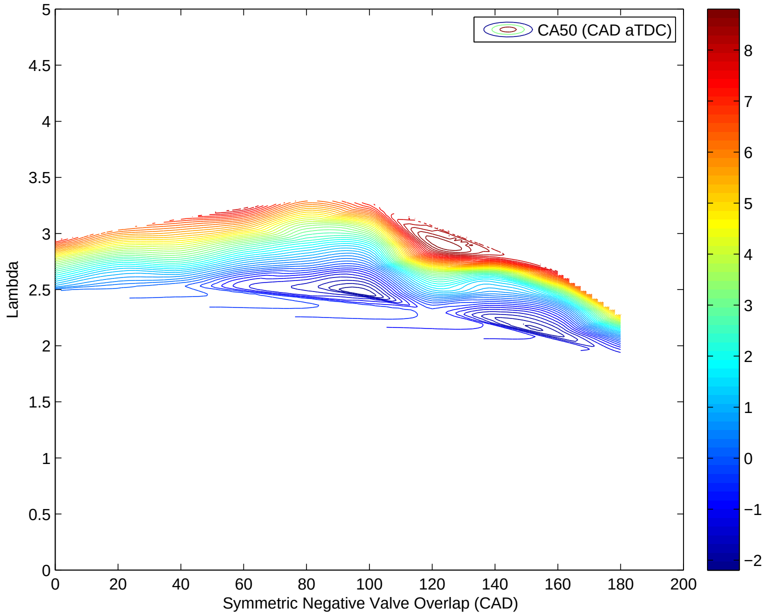

(b) PRF20

Figure 4.6: Engine operating region showing CA50 for SNVO versus lambda for PRF0 and PRF20.

Where ρ_{Air} is the density of air in the intake runner. The results of Equation (4.1) can be found in Figure 4.7. The dilution ratio is effected by fuelling rate as the fuelling rate directly changes the denominator of Equation (4.1). The SNVO duration does not have much of an effect on the dilution of the cylinder due to the diluent being changed from air to residual, and no effective change in the amount of diluent.

To see the increase in internal residual within the intake charge, the second part of Equation (4.1) is plotted similar to Figure 4.8. The result is shown in Figure 4.8, and shows an inversed trend to the airflow shown later in Figure 4.26. This result is expected and shows the increase in internal residual as SNVO is increased.

4.3 Effects of SNVO on CA50

One main goal of using SNVO is to control HCCI combustion timing. In this work, CA50 is used as the measure of combustion timing and with SNVO is plotted to show contours of constant fuelling rate (Figure 4.9). Controlling combustion timing is essential for HCCI combustion [Agrell et al., 2003b] [Shaver et al., 2004] [Agrell, 2006] [Lundstrom, 2006] [Shi et al., 2006] [Bengtsson et al., 2006] [Bögemann, 2009] [Widd, 2009] [Widd et al., 2011] [Bidarvatan et al., 2014]. The contours of constant fuelling rate show how the combustion timing (CA50) changes when fuelling remains constant and SNVO is varied. Generally the combustion timing shows a steady advance as SNVO increases, although there is a slight hump at 120 CAD of SNVO, and an upward inflection in the higher regions. This agrees with similar studies, such as Figure 11 from [Weall et al., 2012], where retarding of CA50 timing is seen with decreasing SNVO. [Chen et al., 2003], [Caton et al., 2005] and [Shi et al., 2006] also find the same results. This result is attributed to increased amounts of hot trapped residual gases at higher levels of SNVO, this heat causes an earlier combustion event given that the fuel quantity is constant.

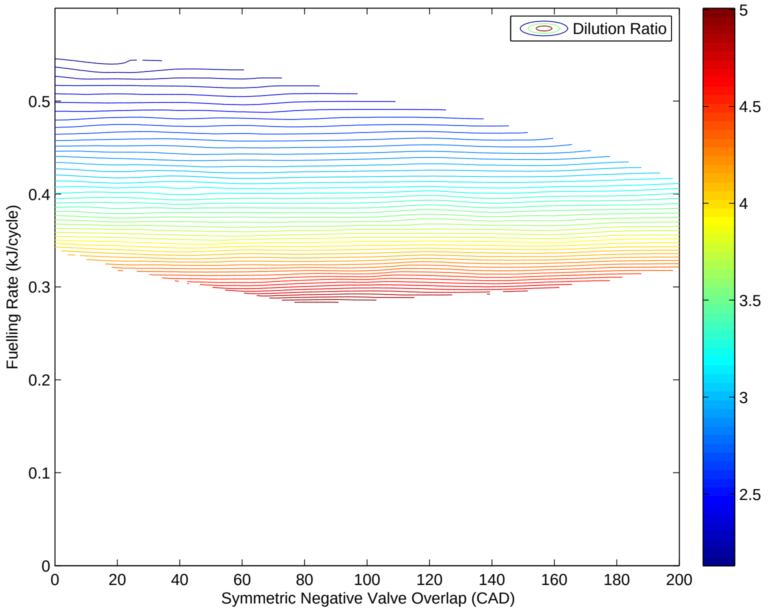

(a) PRF0

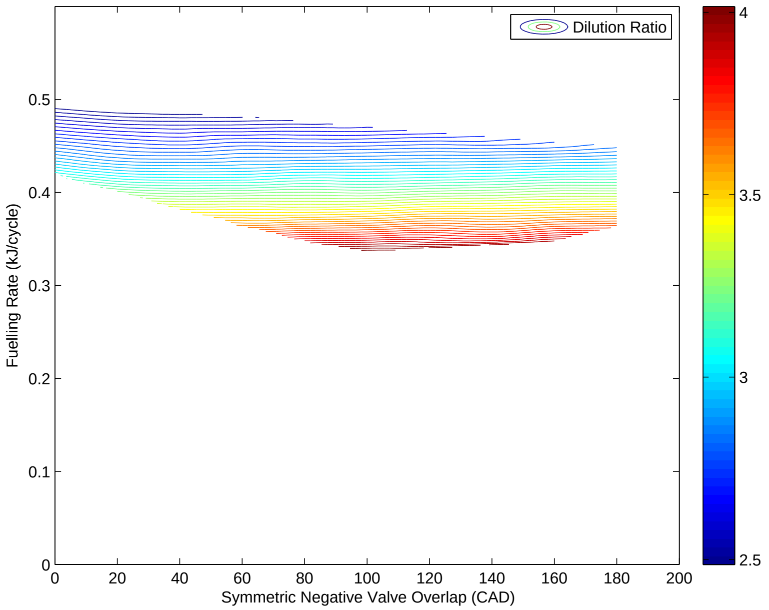

(b) PRF20

Figure 4.7: Engine operating region showing dilution ratio for SNVO versus fuelling rate for PRF and PRF20.

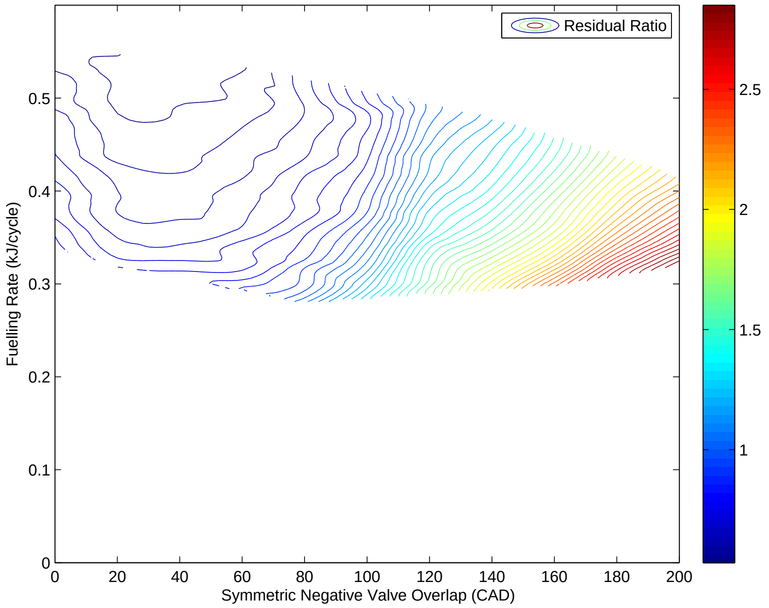

(a) PRF0

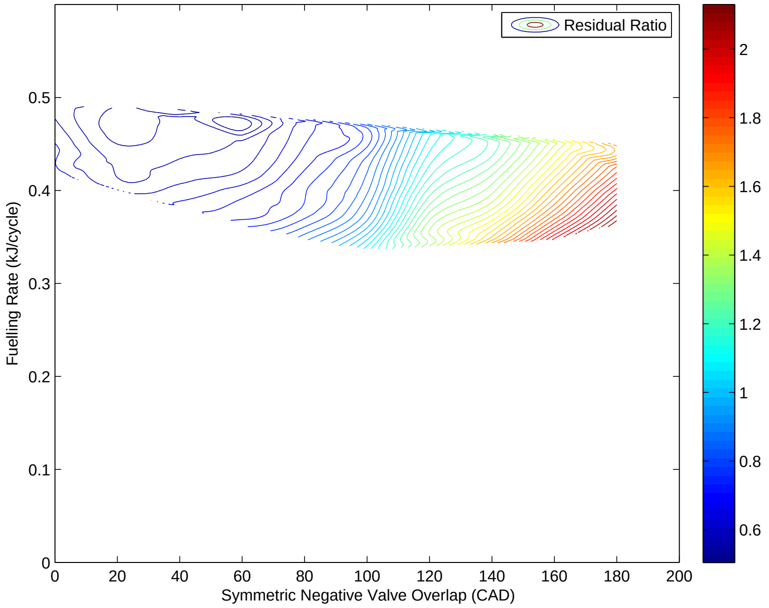

(b) PRF20

Figure 4.8: Engine operating region showing residual ratio for SNVO versus fuelling rate for PRF and PRF20.

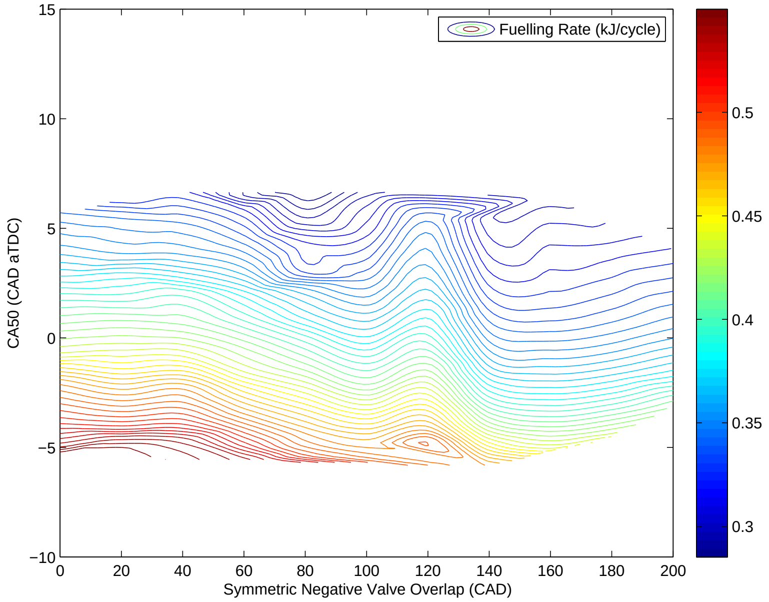

(a) PRF0

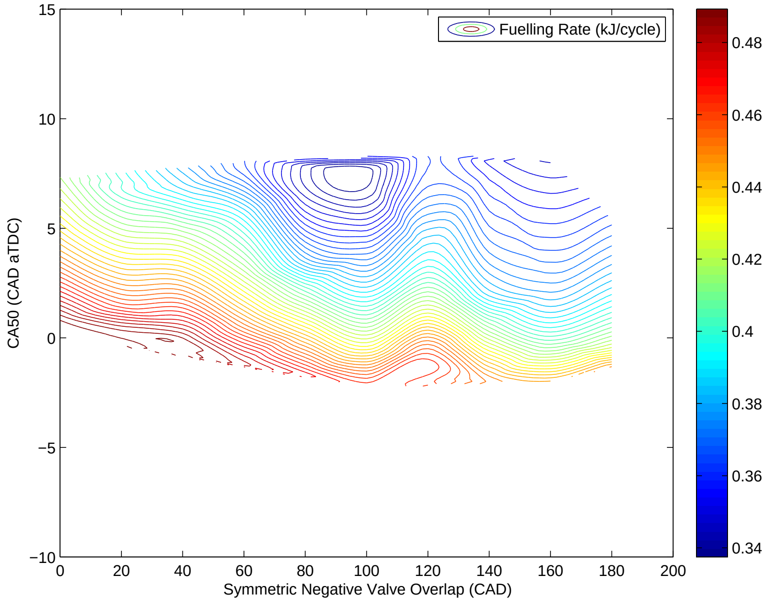

(b) PRF20

Figure 4.9: Effects of SNVO versus CA50 with respect to fuelling rate for PRF0 and PRF20.

Contours of constant load (IMEP) as a function of combustion timing (CA50) and SNVO are shown in Figures 4.10. This illustrates what happens to CA50 if SNVO is changed and a constant load is maintained. CA50 advances as SNVO duration is increased and IMEP is held at a constant, although there is a slight upwards inflection (retarding of combustion timing) near the higher duration regions of SNVO duration.

The effect of SNVO on burn duration is shown in Figure 4.11. Burn duration shows similar behavior to that of CA50, in particular the duration begins to lengthen as CA50 retards past TDC. This effect is attributed to the dilution effects of the trapped residual [Atkins, 2004] as well as the advance of the timing event into a region where the piston is travelling down the cylinder at a higher rate.

Figures 4.12, 4.13 and 4.14 show a comparison of both fuel octanes at a single fuelling rate. Both fuels show a similar trend, yet PRF20 shows a more retarded, longer duration burn at a higher load. The retarding of the timing is caused by less auto-ignition tendency in the PRF20 fuel, causing a later ignition timing. The burn duration increases due to the combustion timing being after TDC, in a region where burn duration is elongated and results in a higher IMEP as the combustion occurs during the downstroke of the piston. For CA50 before TDC, particularly with the PRF0 fuel, a sharp decline in burn duration is witnessed as well, as the rapid compression of the combusting mixture during the upstroke shortens the burn duration.

4.4 Effects of SNVO on Engine Load

To examine the differences in fuelling and load a contour map of IMEP with SNVO on the x-axis and fuelling rate on the y-axis for two fuels is shown in Figure 4.15. At a constant fuelling rate, as SNVO is increased, the load slightly increases. This is attributed to the decrease in lambda seen in Figure 4.3 as well as a shift in peak

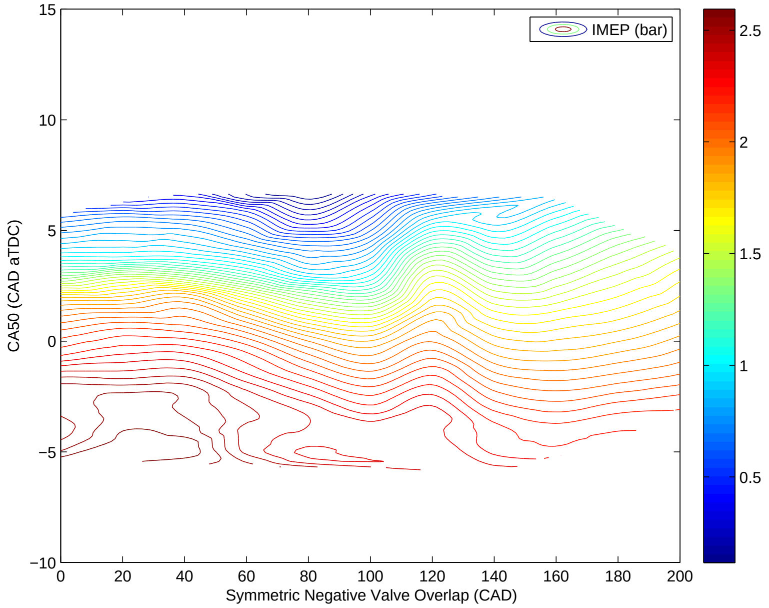

(a) PRF0

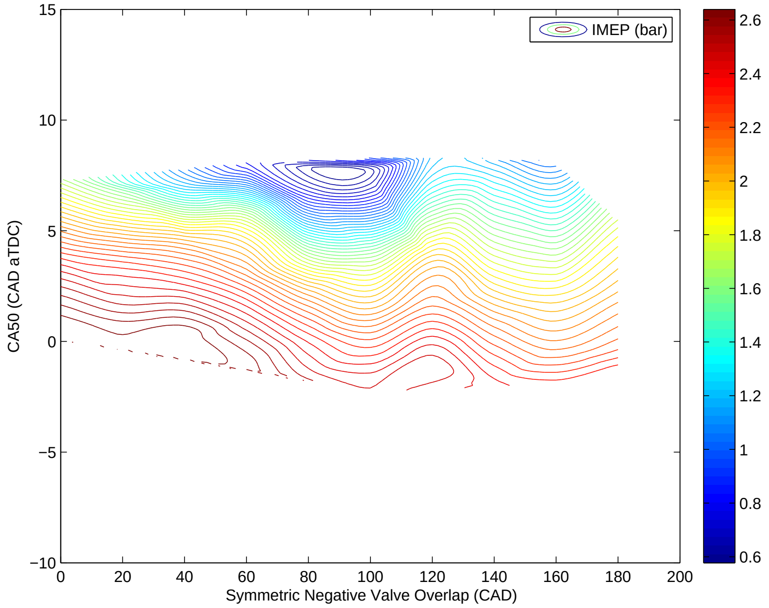

(b) PRF20

Figure 4.10: Effects of SNVO versus CA50 with respect to IMEP for PRF0 and PRF20.

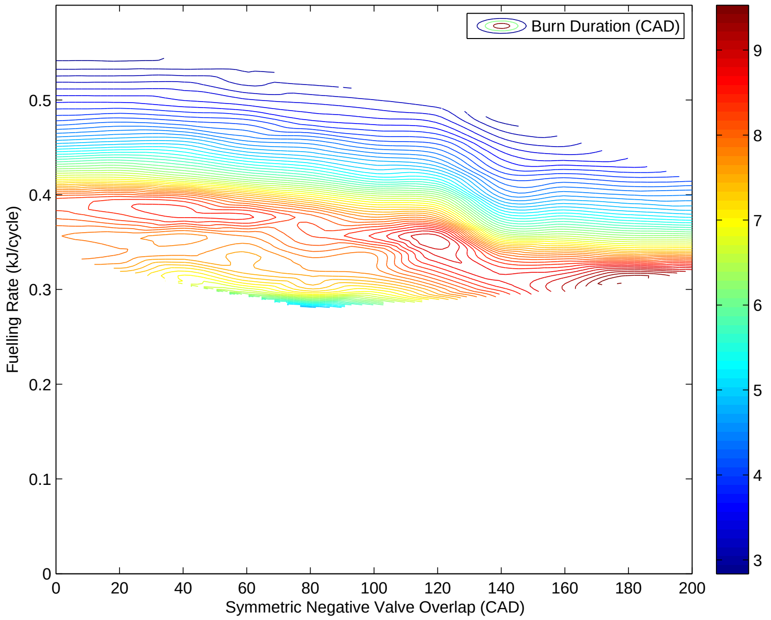

(a) PRF0

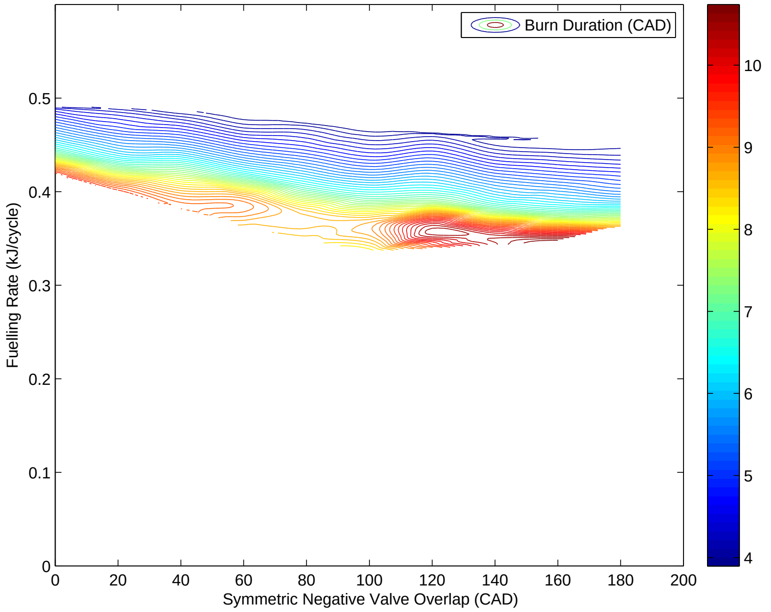

(b) PRF20

Figure 4.11: Effects of SNVO versus fuelling rate with respect to burn duration for PRF0 and PRF20.

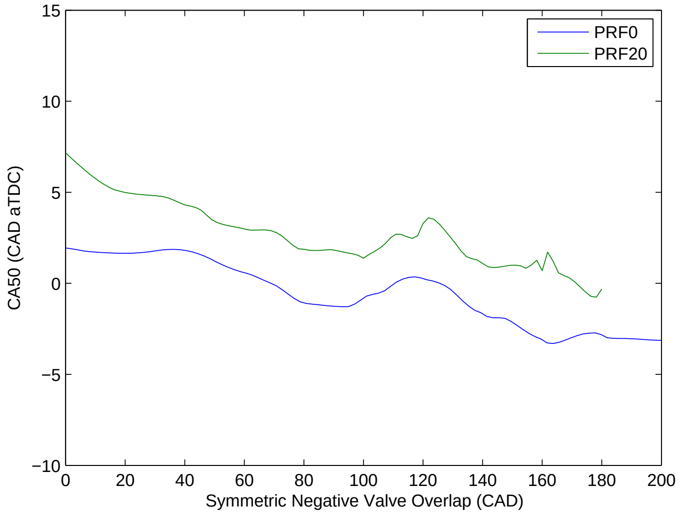

Figure 4.12: A comparison of CA50 for an injected fuel energy of 0.42 kJ per cycle for PRF0 and PRF20 with respect to SNVO.

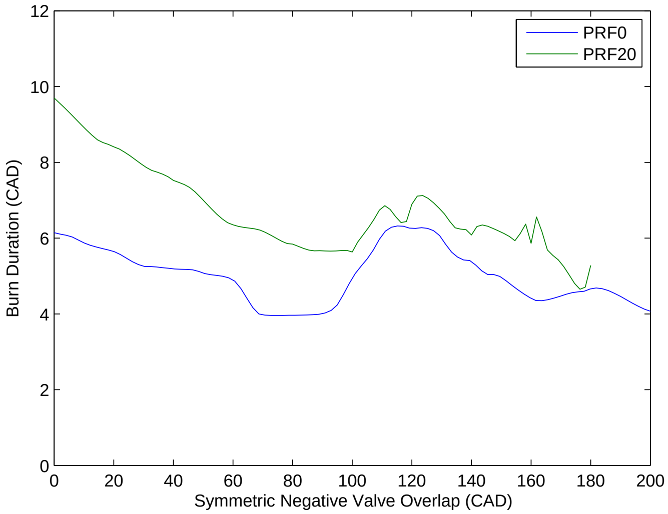

Figure 4.13: A comparison of burn duration for an injected fuel energy of 0.42 kJ per cycle for PRF0 and PRF20 with respect to SNVO.

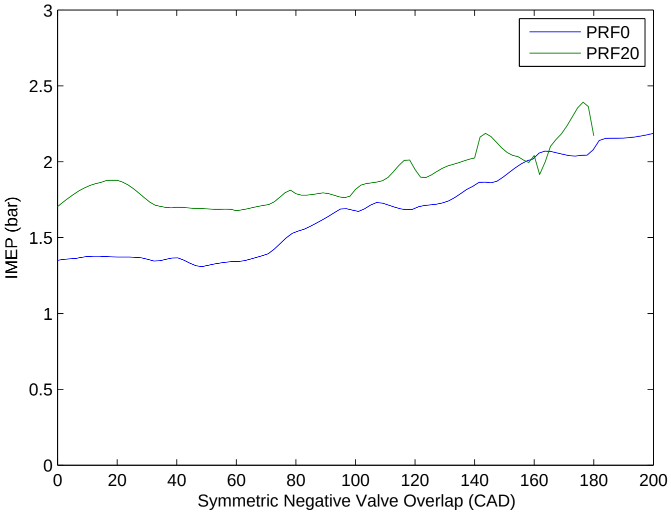

Figure 4.14: A comparison of IMEP for an injected fuel energy of 0.42 kJ per cycle for PRF0 and PRF20 with respect to SNVO.

pressure timing causing a load change. Also the dilution effects of the residual decreases heat transfer to the cylinder walls which results in an increase in IMEP. In [Chen et al., 2003], they find the opposite effect. This could be attributed to a number of factors, although lambda would be one of the prominent causes to a drop in IMEP as EGR rates increase.

Combustion timing (CA50) as a function of engine load (IMEP) is plotted for each of the eleven constant values of SNVO in Figures 4.16. There seems to be two SNVO ranges to these curves: (1) between SNVO of 0 to 100 CAD, the curves have a smaller slope of approximately $-3\ CAD/bar$ up to approximately 1.9 bar IMEP; (2) when SNVO is greater than 100 CAD the combustion timing advances rapidly with load with a slope of approximately $-8\ CAD/bar$. This combustion timing effect is also partially seen in Figure 6 of [Shi et al., 2006], where a slight downward inflection of the timing/load curves is seen. In the lower range, SNVO advances timing and lowers load as it increases, [Shi et al., 2006] finds a similar result. The other SNVO range (SNVO's between 120 and 200) has a more linear result, but does not reach as low a

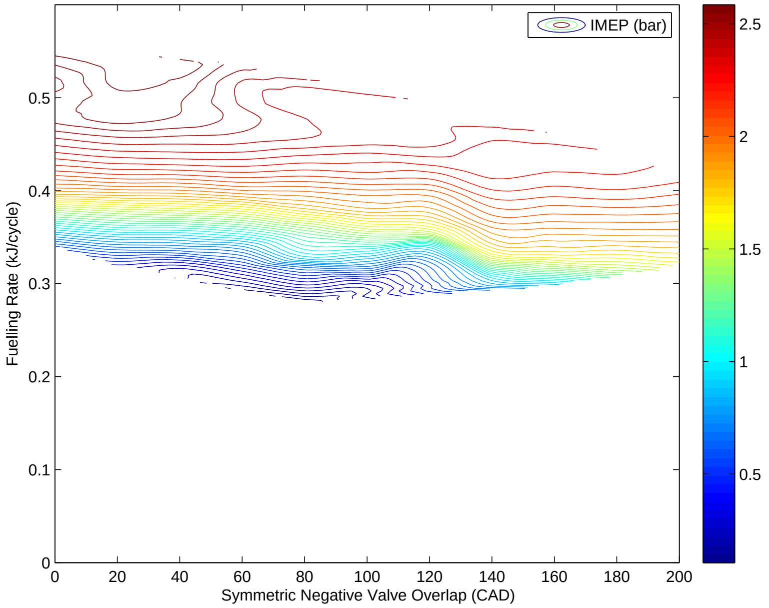

(a) PRF0

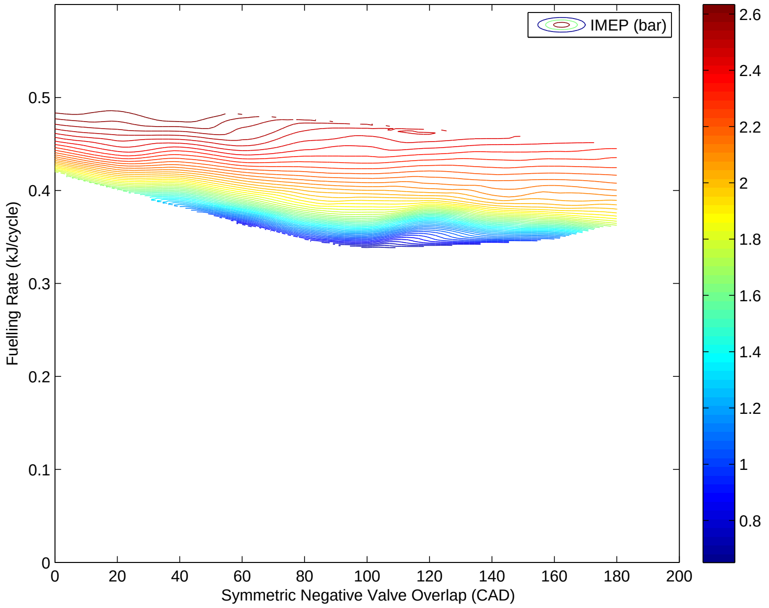

(b) PRF20

Figure 4.15: Effects of SNVO versus fuelling rate with respect to IMEP for PRF0 and PRF20.

load as the lower SNVO range. At mid-region loads (below the inflection seen in the low SNVO range), the high SNVO range has a higher CA50, and does not show much correlation between SNVO and load or timing. In the higher load regions (above the inflection mentioned earlier), these curves resume the normal behavior of the other curves, including the correlation between increased SNVO and lowered timing and load. Burn duration is shown in Figures 4.17, and the curves show similar behavior as the CA50 curves in Figures 4.16. Figure 4.18 shows a comparison of CA50 and burn duration.

4.5 Effects on Thermal Efficiency

Brake specific fuel consumption (BSFC) is shown in Figures 4.19 with respect to injected fuel energy. Again the dual range of SNVO is seen. The lower range (SNVO durations from 0 to 100 CAD) achieves a lower overall BSFC, but in the low fuel injected energy region the higher SNVO range tends to achieve a lower BSFC. Figure 4.15 also shows that the upper range of SNVO durations produces a slightly larger load (for the same injected fuel energy), so if Figure 4.19 is plotted against IMEP instead of fuelling rate, a more regular trend of increasing BSFC with SNVO duration can be seen (see Figure 4.20). The studies [Abd-Alla, 2002] and [Agarwal et al., 2011] both look at the effect of external EGR on BSFC in a diesel engine, and both found opposite effects. [Abd-Alla, 2002] showed that an increase in external EGR lead to a decrease in BSFC. [Agarwal et al., 2011] showed that BSFC slightly decreased with increased external EGR. This suggests that engine layout and operating parameters have large effects on BSFC as well. This might be why [Chen et al., 2003] and [Weall et al., 2012] both showed the opposite effect of NVO on BSFC.

Figures 4.21, 4.22, and 4.23 show the optimal operating point with respect to thermal efficiency (kinetic energy extracted per injected fuel energy). The equation

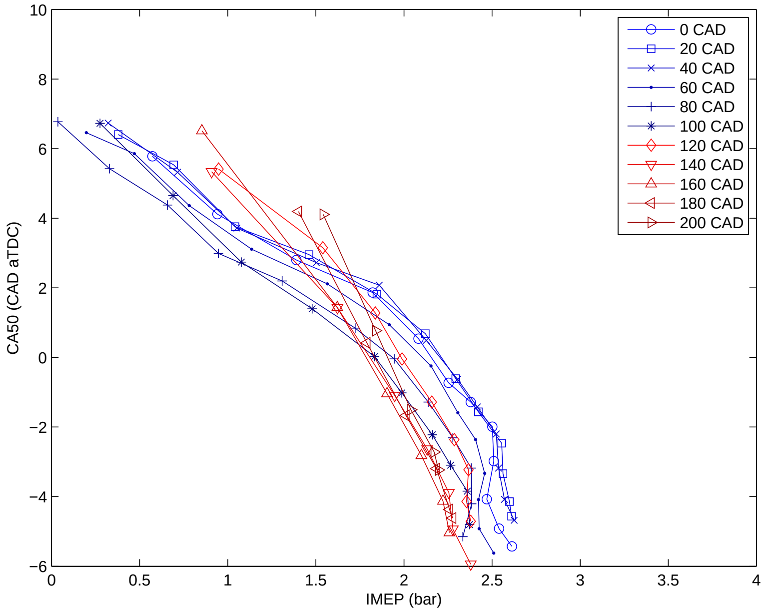

(a) PRF0

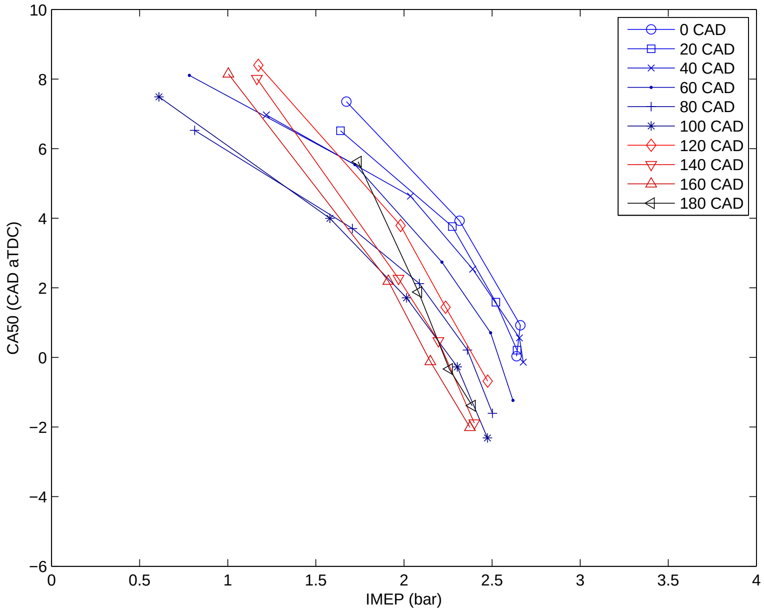

(b) PRF20

Figure 4.16: Plot of IMEP versus CA50 with lines of constant SNVO for PRF0 and PRF20.

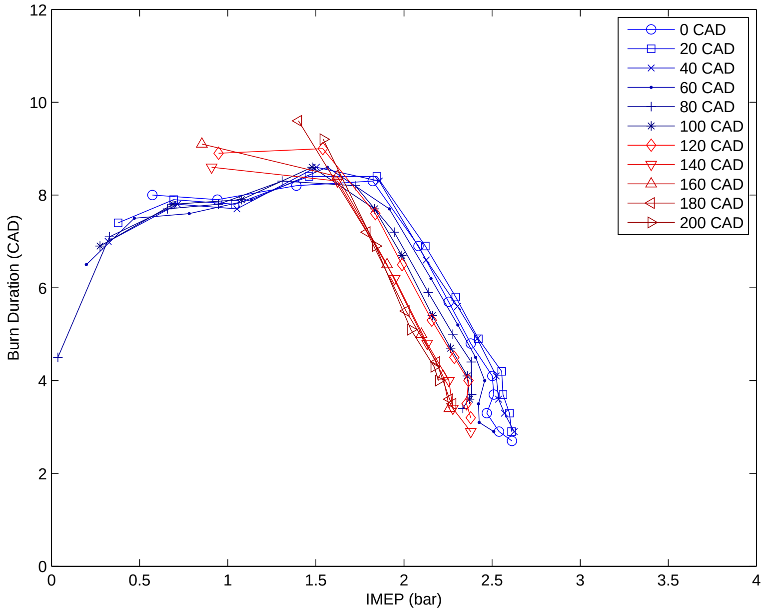

(a) PRF0

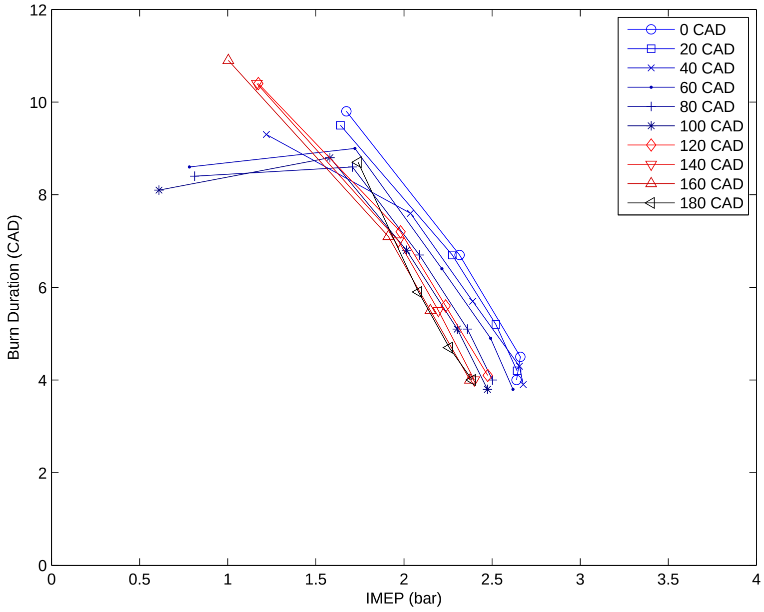

(b) PRF20

Figure 4.17: Plot of IMEP versus burn duration with lines of constant SNVO for PRF0 and PRF20.

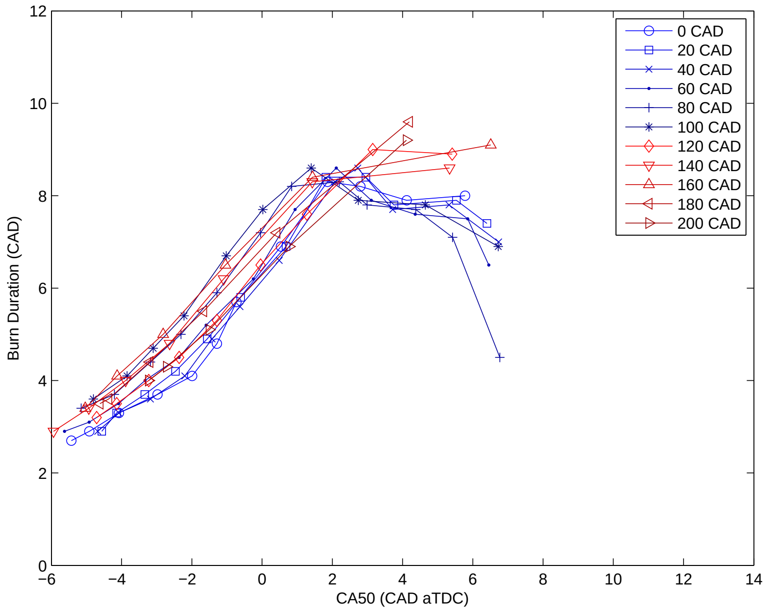

(a) PRF0

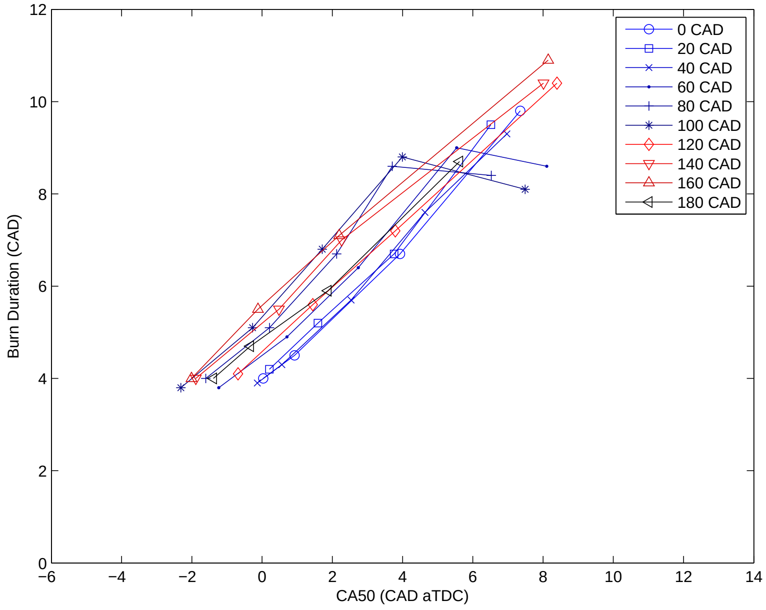

(b) PRF20

Figure 4.18: Plot of CA50 versus burn duration with lines of constant SNVO for PRF0 and PRF20.

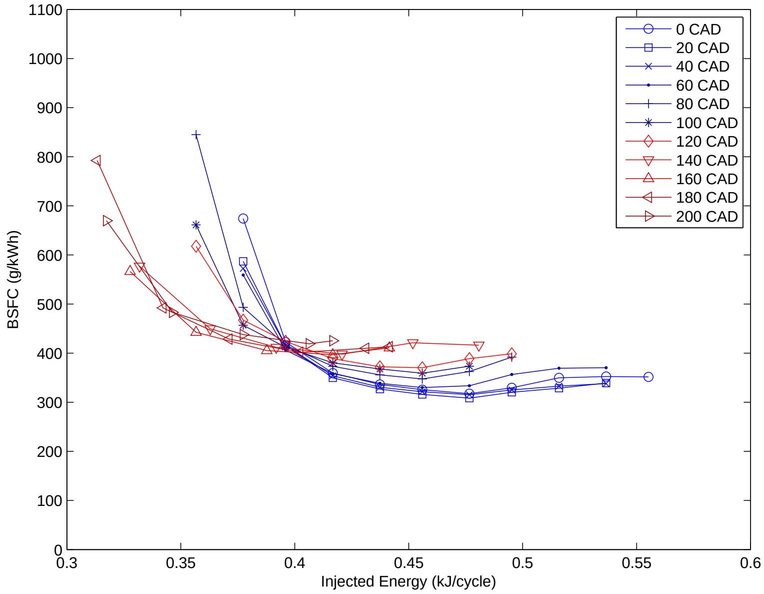

(a) PRF0

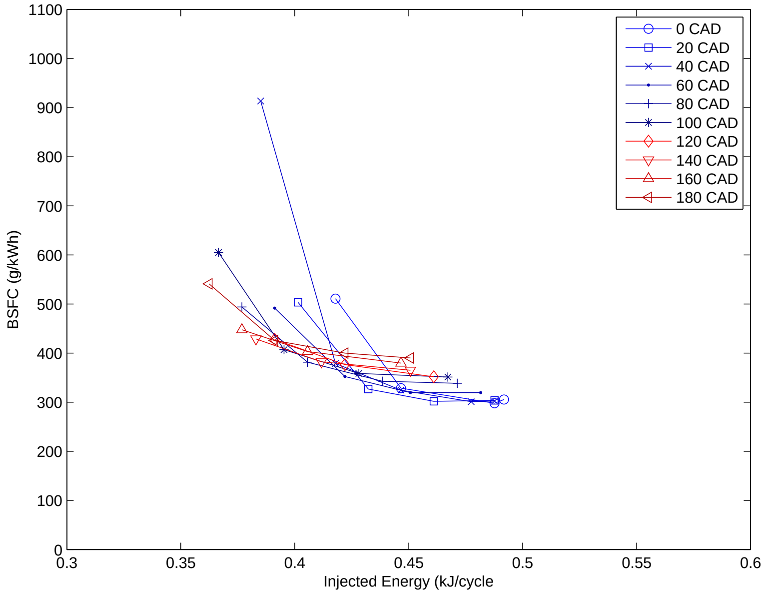

(b) PRF20

Figure 4.19: Plot of fuelling rate versus BSFC with lines of constant SNVO for PRF0 and PRF20.

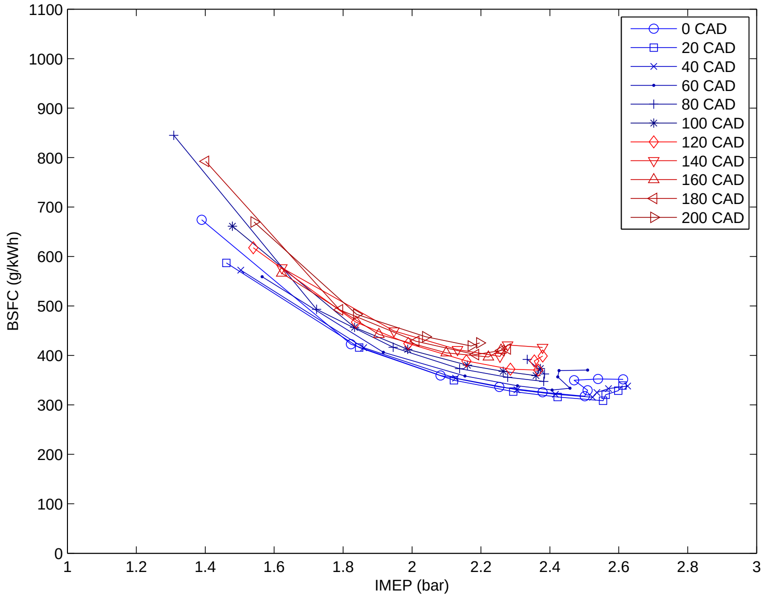

(a) PRF0

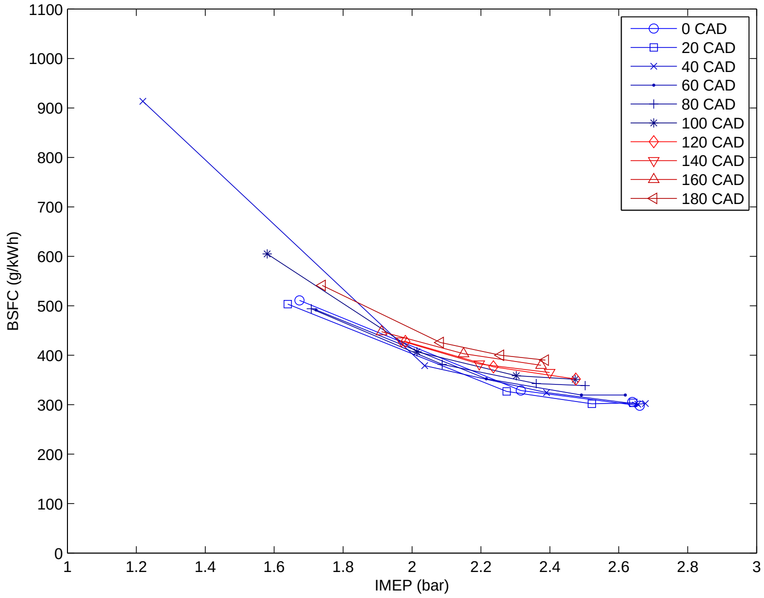

(b) PRF20

Figure 4.20: Plot of IMEP versus BSFC with lines of constant SNVO for PRF0 and PRF20.

used to calculate $\eta_{Thermal}$ is:

$$\eta_{Thermal} = \frac{V_d IMEP}{E_{Injected}} = \frac{V_d IMEP}{LHV m_{Fuel}} \tag{4.4}$$

where $E_{Injected}$ is the amount of fuel injected per cycle in kJ, calculated by the product of injected fuel mass (m_{Fuel}) and the fuels lower heating value (LHV). The resulting efficiencies are compared to CA50, burn duration and work efficiency are shown in Figures 4.21, 4.22 and 4.23. Work efficiency is defined as:

$$\eta_{Work} = \frac{Q_{Total}}{E_{Injected}} \tag{4.5}$$

Where Q_{Total} is the heat release calculated from the pressure trace in Equation (2.4). The optimal efficiency found was 36% for PRF0 fuel at an SNVO duration of 140 CAD and a CA50 timing of -2.6 CAD aTDC with a burn duration of 4.8 CAD. The combustion efficiency was found to be 69% at that point. For PRF20 fuel, the most efficient point was 37% at an SNVO duration of 40 CAD, a CA50 timing of 0.6 CAD aTDC with a duration of 4.3 CAD, and a combustion efficiency of 72%. For the PRF20 fuel, the most efficient point is also around the highest load point, but for PRF0 fuel, the load continues to increase as timing is advanced further and, more significantly, as SNVO duration is increased. It is also seen that as combustion efficiency increases past the thermal efficiency peak for both fuels, into the higher load region for PRF0, the thermal efficiency begins to decrease.

Figures 4.21 through 4.23 show higher durations of SNVO result in higher thermal efficiency while Figure 4.20 suggests the opposite. This conflict can be attributed to the fact that $\eta_{Thermal}$ is calculated from in-cylinder pressures, while BSFC is calculated using dynamometer torque measurements. This loss in efficiency is due to the heat and pumping losses during the recompression stage of the SNVO, which increases

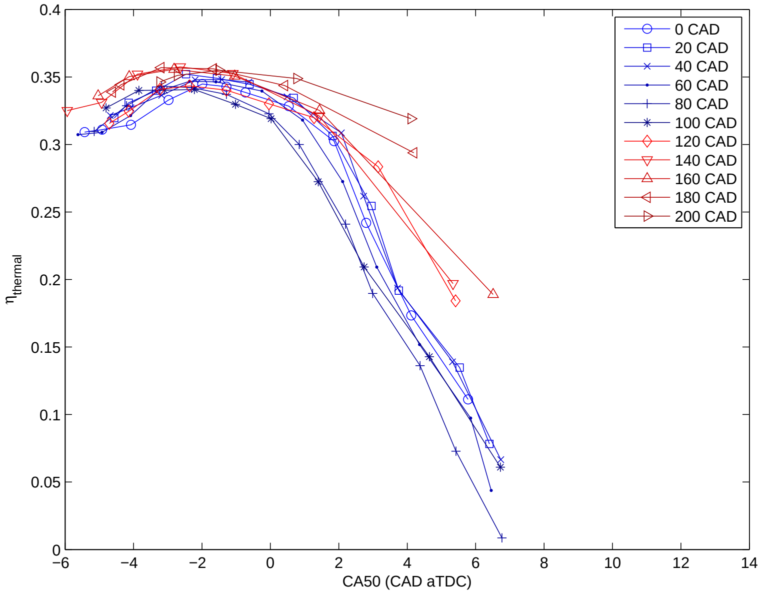

(a) PRF0

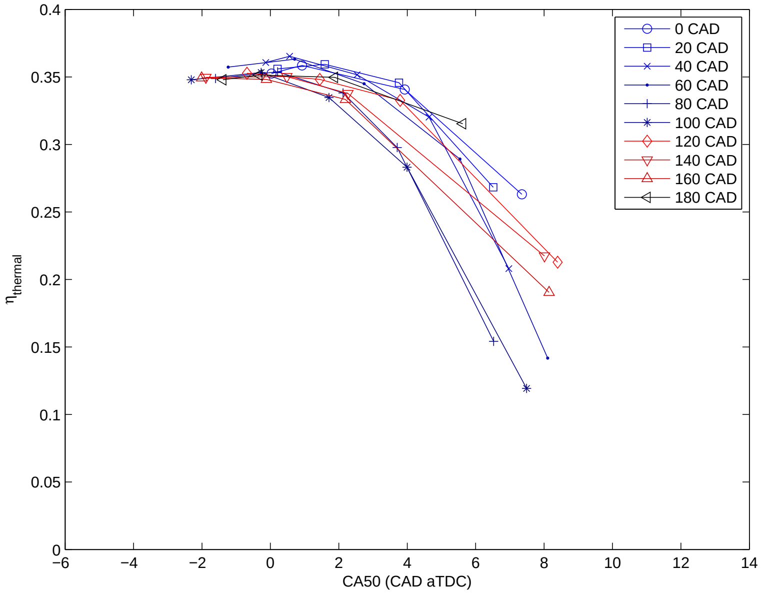

(b) PRF20

Figure 4.21: Thermal efficiency compared to CA50 with lines of constant SNVO for PRF0 and PRF20.

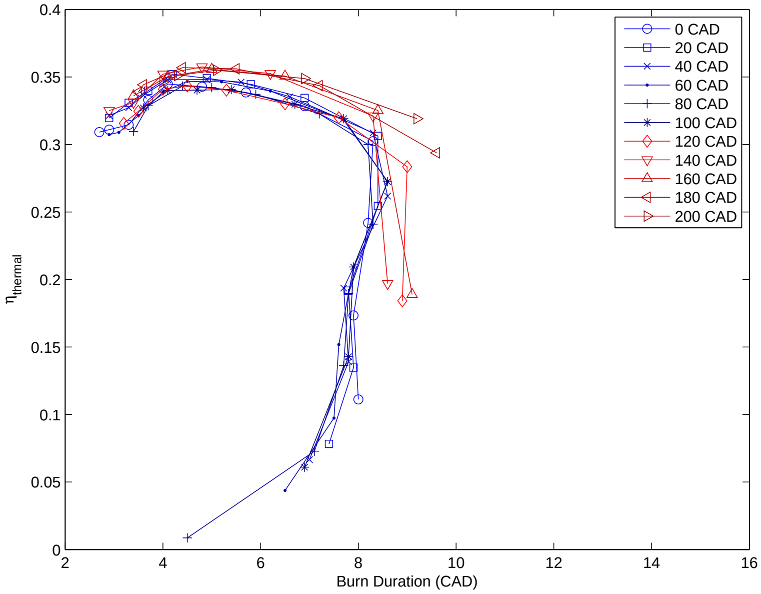

(a) PRF0

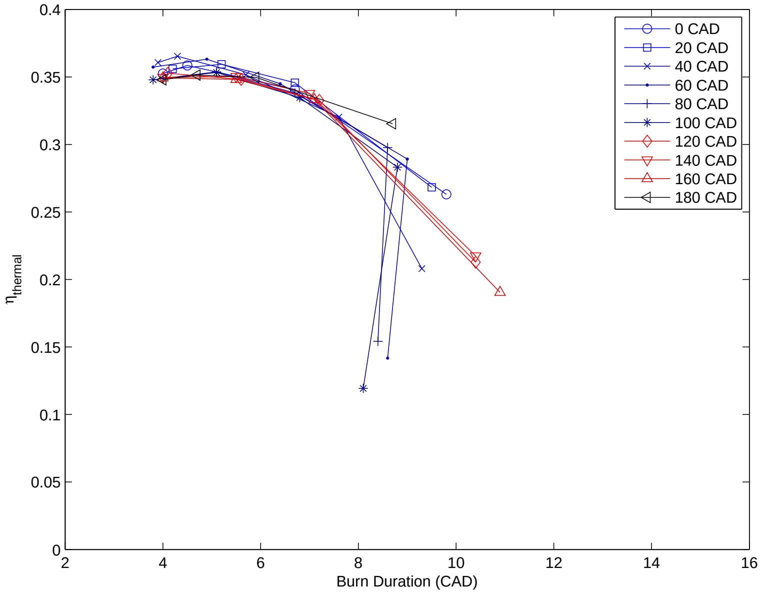

(b) PRF20

Figure 4.22: Thermal efficiency compared to burn duration with lines of constant SNVO for PRF0 and PRF20.

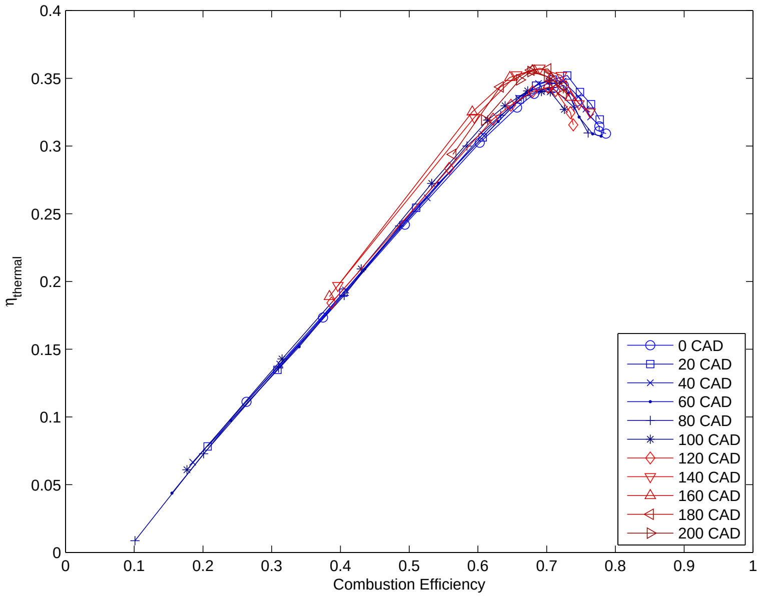

(a) PRF0

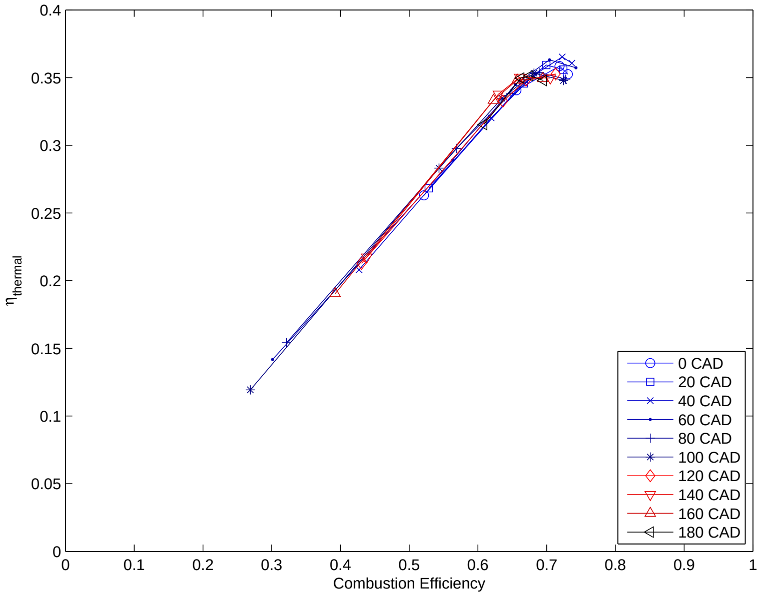

(b) PRF20

Figure 4.23: Thermal efficiency compared to combustion efficiency with lines of constant SNVO for PRF0 and PRF20.

with increasing SNVO.

To see the effects of timing on thermal efficiency and BSFC, a P-V diagram for two fuelling rates at 80 CAD of SNVO duration is plotted in Figure 4.24. This figure shows the P-V diagram for a low thermal efficiency point, corresponding to a CA50 timing of 4 CAD aTDC, and a point of high thermal efficiency, corresponding to a CA50 timing of -2 CAD aTDC. The work output for the higher efficiency plot can be seen to be much larger due to the much higher peak pressure at TDC of the compression stroke, whereas compression work for both plots remain similar. The low peak pressure in the other plot is due to the late combustion resulting in a late peak pressure timing, when the cylinder volume is larger, resulting in lower peak pressures. The pumping losses for both points are relatively equal.

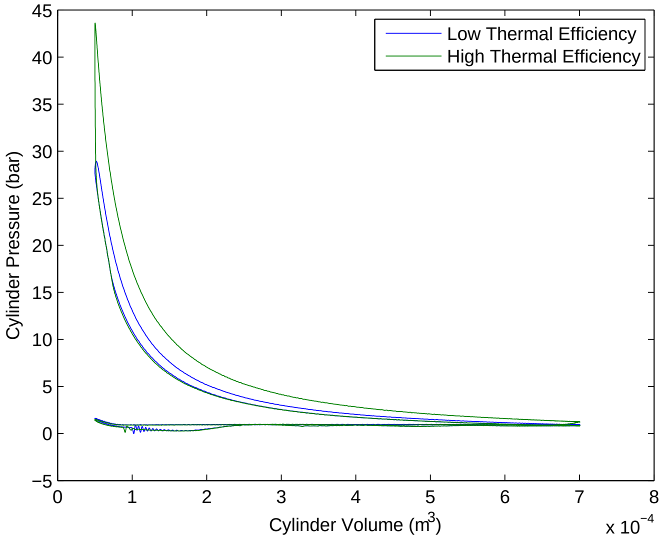

Figure 4.24: Comparison of a High Thermal Efficiency (CA50 = -2 CAD aTDC) and a Low Thermal Efficiency (CA50 = 4 CAD aTDC) points using a P-V Diagram

4.6 Effects of SNVO on Emissions

In this section the experimental results of SNVO effects on HCCI engine exhaust emissions is described. The emissions are collected with a 5-gas analyzer which can only capture emissions at steady state operation, due to the large time constant of the measurement system and samples lines. Measurements of CO_2, CO and O_2 in percentage, and NO_x and hydrocarbons in ppm are collected with details of the measurement errors in Table 3.4.

Since exhaust temperature control is of importance to maintain high efficiency in the catalytic converter, it is also measured. A typical catalytic converter has a light-off temperature of 600 K, the temperature at which the conversion of CO and hydrocarbons exceeds 50% [Heywood, 1988]. The low exhaust temperatures experienced during HCCI combustion will require special catalysts. Experimental results show that SNVO has a slight effect on exhaust temperature, as shown in Figures 4.25. There is a slight rise in exhaust temperature as more SNVO is introduced, but only at most 30 °C in change. [Caton et al., 2005] shows a similar slight increase in exhaust temperature. The temperatures seen in the exhaust of the engine are extremely low, which can be attributed to the low loads. Large combustion chamber crevices (see Figure 3.1) are regions of low temperatures and often have incomplete combustion which affects emissions significantly.

Figure 4.26 shows that the total airflow into the engine begins to reduce significantly above 100 CAD of SNVO. This is reflected in the residual ratio described in Figure 4.8. The effects of this can easily be seen in the lambda and fuelling rate contours of Figures 4.3, where the lambda gets richer at constant fuelling rates as SNVO increases past 100 CAD. This is the result of a short intake valve duration and a large amount of residual held within the cylinder cycle to cycle.

The effect of SNVO on CO_2 emissions is a linear increase in percentage of exhaust gas sample, seen in Figure 4.27. This can be attributed, in conjunction with the decrease in O_2 shown in Figure 4.28, to an increase in the completeness of combustion and results in a higher exhaust temperature (Figures 4.25). There is also a reduction in hydrocarbons (despite an outlier) in Figure 4.29. This reinforces the findings

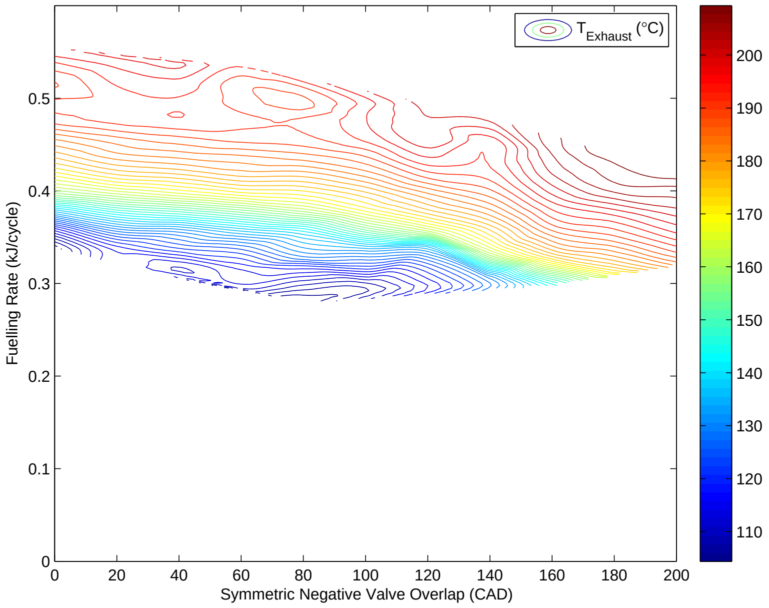

(a) PRF0

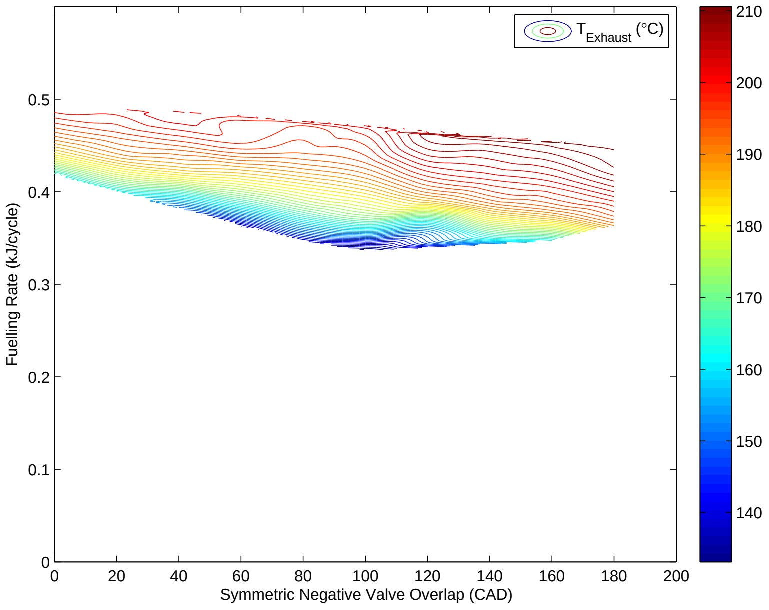

(b) PRF20

Figure 4.25: Effects of SNVO versus fuelling rate on exhaust temperature for PRF0 and PRF20.

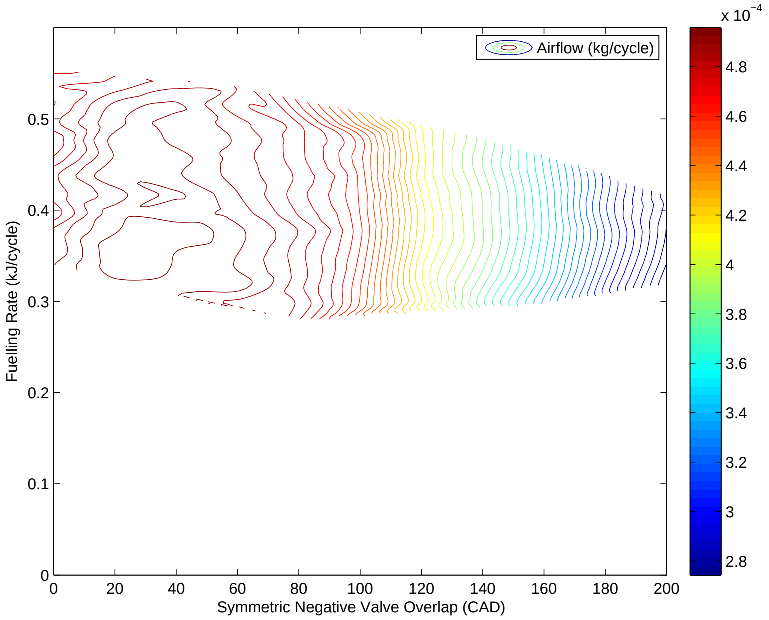

(a) PRF0

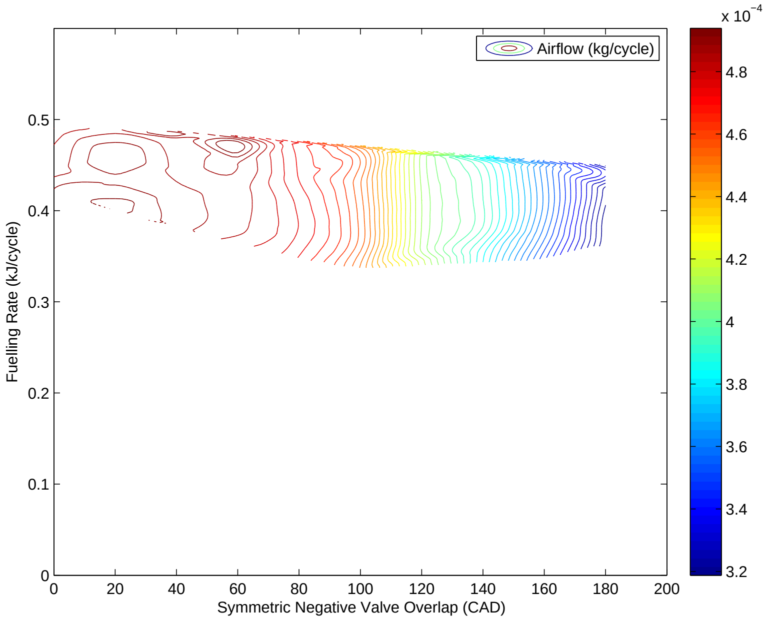

(b) PRF20

Figure 4.26: Effects of SNVO versus fuelling rate on airflow rate for PRF0 and PRF20.

of increased fuel efficiency in Section 4.4, as an increase in combustion efficiency generally results in an increase of fuel efficiency (Figure 4.23). [Caton et al., 2005] looks into hydrocarbon emissions as a result of SNVO, but does not clearly present the results as a function of SNVO angle or amount of EGR.

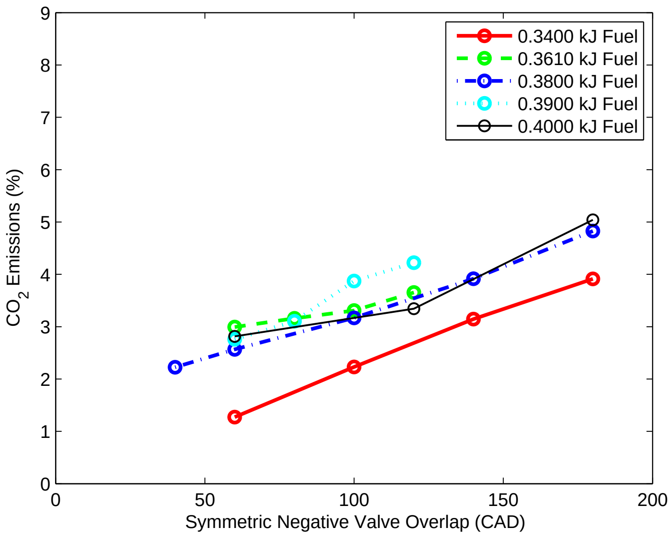

Figure 4.27: Effects of SNVO on CO_2 emissions for five fuelling rates of PRF0.

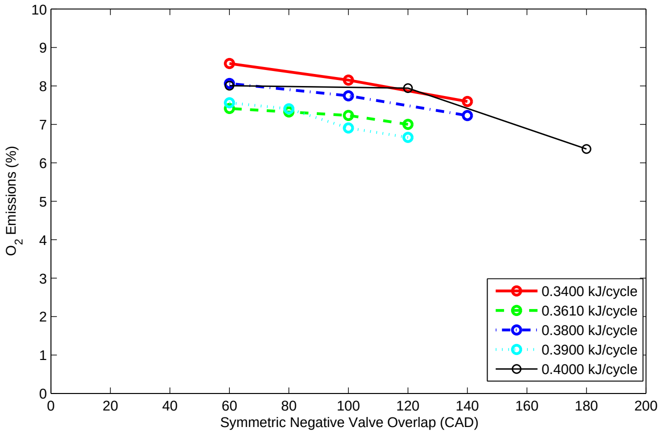

Figure 4.28: Effects of SNVO on O_2 emissions for five fuelling rates of PRF0.

The hydrocarbons presented in Figure 4.29 are fairly high. This is attributed to the large crevice volumes on the piston crown required for free-running EVVT operation, and low loads. There is also correlation with the low exhaust temperature, which indicates a lower in-cylinder temperature during combustion, and poor or no combustion in the crevices and near the walls [Christensen et al., 2001]. At low loads and high dilution, the chemical reactions also do not go to completion, resulting in higher hydrocarbon and CO emissions [Dec and Sjöberg, 2003].

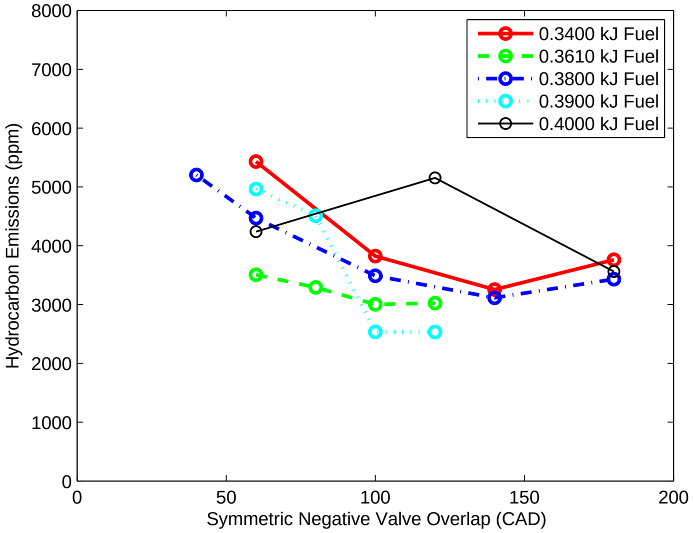

Figure 4.29: Effects of SNVO on hydrocarbon emissions for five fuelling rates of PRF0.

The NO_x emissions in Figure 4.31 are very low (near the resolution of the instrument) due to low combustion temperatures. The creation of NO_x occurs due to in-cylinder temperatures above 1800 C [Heywood, 1988]. In [Atkins, 2004], the investigation of NO_x versus in-cylinder peak pressure found that for increasing peak pressure and increasing PRF, NO_x increased. For the values of peak pressure and PRF in this study, NO_x will be nearly negligible. [Shi et al., 2006] found that NO_x increases with IMEP and NVO. [Caton et al., 2005] finds the same effect with increasing mean effective pressure (MEP). Both studies have NO_x measurment points much higher than 20 ppm probably due to the higher loads. [Shi et al., 2006] has loads between 3 and 4 bar IMEP and [Caton et al., 2005] between 2 and 3.5 bar IMEP.

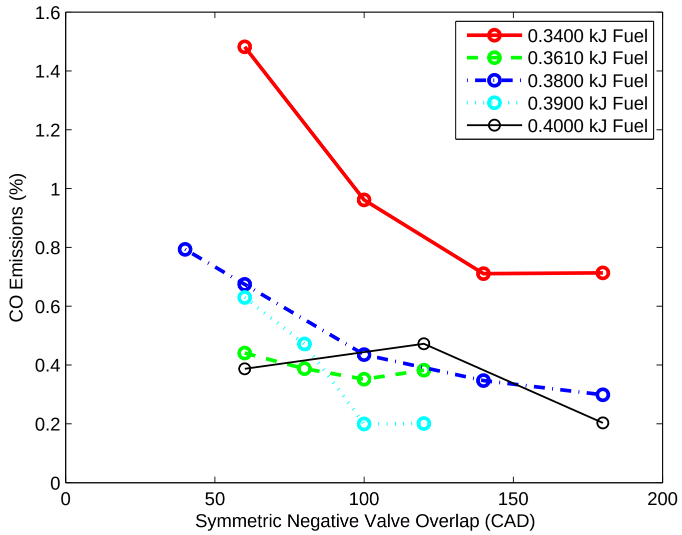

Figure 4.30: Effects of SNVO on CO emissions for five fuelling rates of PRF0.

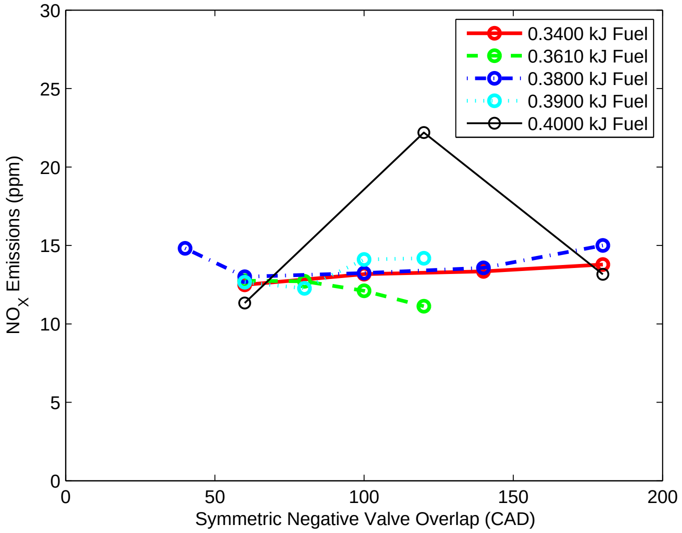

Figure 4.31: Effects of SNVO on NO$_x$ emissions for five fuelling rates of PRF0.

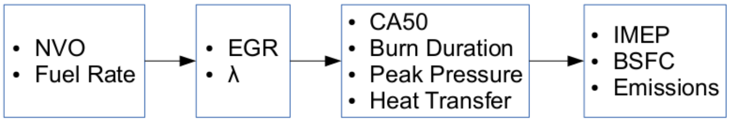

Figure 4.32: Flowchart of the effects of SNVO and fuelling rate on engine operation.

This section, along with the previous sections, shows that using SNVO and fuelling rates as inputs influence combustion timing, CA50 and burn duration, which in turn affects the load, IMEP. This is a result of the two inputs, SNVO and fuelling rate, affecting the internal exhaust residual and lambda of the in-cylinder mixture. The residual and lambda dictate the temperature and total fuel energy in the cylinder, influencing the duration and timing of the combustion. Figures 4.16 and 4.17 show that if the burn duration is short and the timing is advanced, the resulting IMEP is highest. The main effects of each value are shown in a flowchart in Figure 4.32.

4.7 Effects of Asymmetric NVO

Asymmetric NVO valve timing strategy is tested in this section. The timings shown are where the symmetry of the valves fall with respect to TDC, as explained in Section 2.3. Sets of tests are conducted at 40 CAD, 60 CAD and 80 CAD of NVO, and the timing is varied until the EVVT valves failed due to abnormal pressures. All the tests are run at 800 RPM and 0.4 kJ per cycle of PRF0 fuel.

Figures 4.33 through 4.35 show the early, late asymmetric and symmetric pressure trace and net heat release curves. The late asymmetric timing shows the fastest rising heat release curve and highest peak pressure, with the shortest burn duration and earliest CA50 in Figure 4.3.

The effects of asymmetric NVO on the dilution ratio of the cylinder charge is again calculated, and the result is no change between valve timings or durations. The dilution ratio remained approximately constant at 3.2 for the cases tested. The

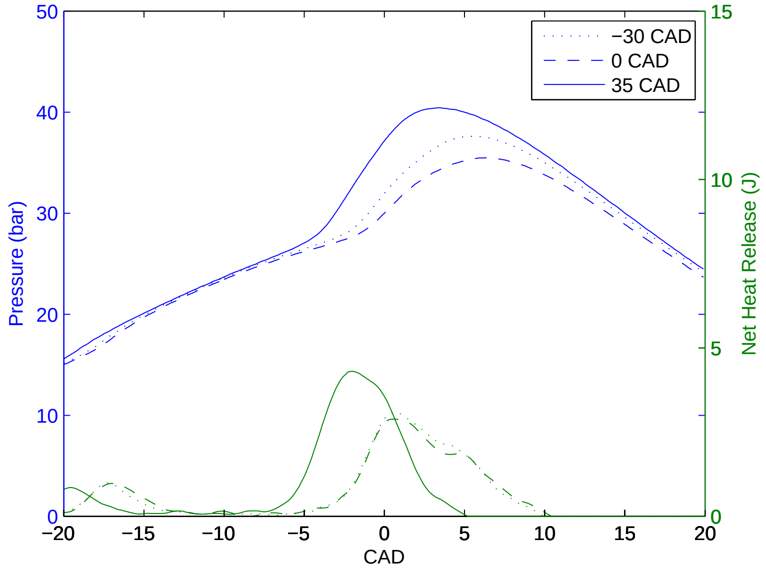

Figure 4.33: Pressure traces and heat releases for three separate asymmetric timings at 40 CAD of NVO.

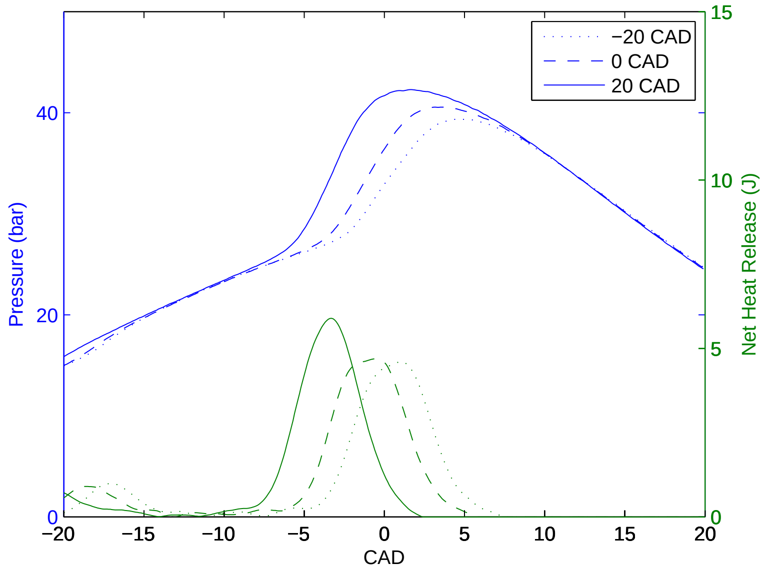

Figure 4.34: Pressure traces and heat releases for three separate asymmetric timings at 60 CAD of NVO.

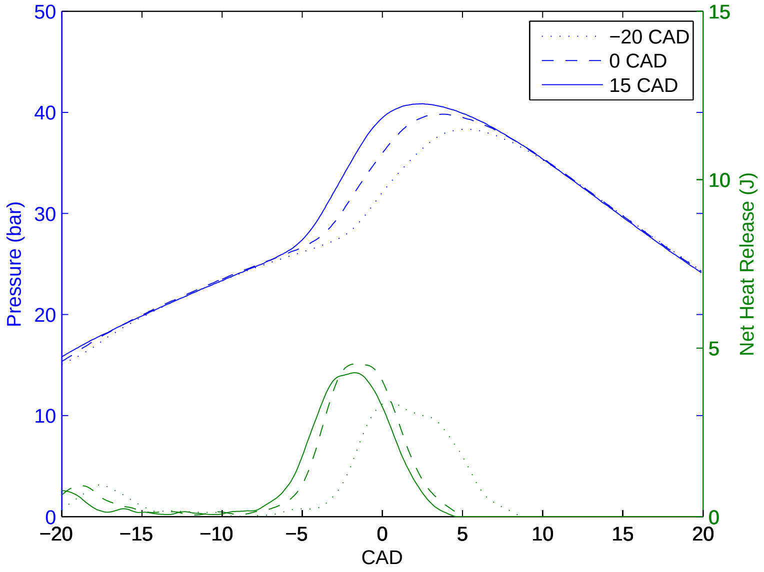

Figure 4.35: Pressure traces and heat releases for three separate asymmetric timings at 80 CAD of NVO.

residual ratio of the mixture is also more complicated for this valve strategy, and the simplified formula used in Section 4.2 will not take into account all the fluid dynamics occurring during the gas exchange process.

The timing effects of asymmetric NVO are shown in Figure 4.36. CA50 shows an approximately flat slope when the valve timing is before -5 CAD aTDC. This is very near the symmetric timings of 0 CAD aTDC. CA50 then begins to decrease for all NVO durations after -5 CAD aTDC. Although the burn duration trend is harder to discern, it can also be seen to be decreasing slightly after -5 CAD aTDC. This point of -5 CAD aTDC suggests that with asymmetric NVO there is a point where any more trapped exhaust residual has no effect, and this point is close to the symmetric point. This can be attributed to the mixing effects when the exhaust residual is pushed into the intake at earlier asymmetric timings which also causes some cooling.

Both 60 CAD and 80 CAD share similar results both sharing common trends and similar values of both CA50 and burn duration. At a NVO of 40 CAD, a retarding of

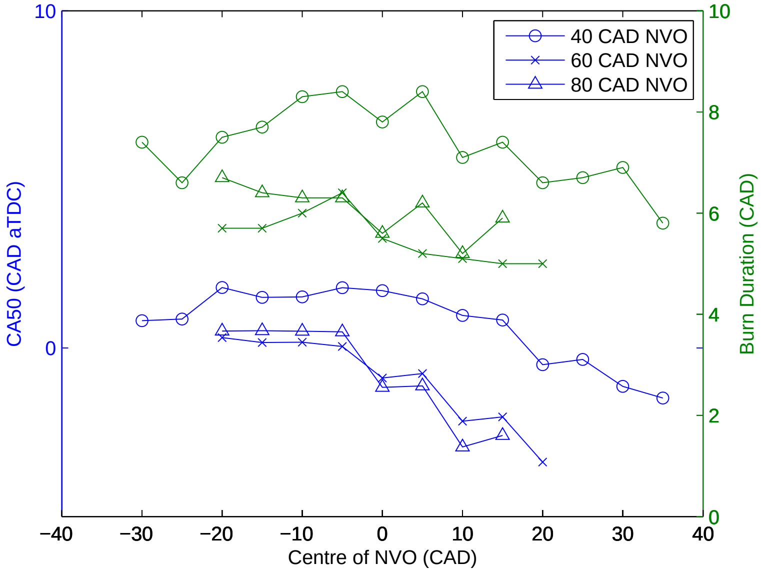

Figure 4.36: Variation of CA50 and burn duration plotted against the centre of NVO timing.

CA50 timing and an increase in burn duration is seen when compared to higher values of NVO duration. The trends change slightly as well. The tests with 40 CAD of NVO are able to go to much further extreme timings that those of 60 and 80 CAD of NVO. This suggests that the closer the NVO duration is to 0 CAD, the less volatile and abnormal the pressure changes are during valve events, allowing the EVVT valves to operate on a larger range. It also suggests that the residual amount, or temperature, is less due to a retarding of the CA50 timing.

Figure 4.37 shows the IMEP and BSFC of all three NVO durations. The durations of 60 and 80 CAD show similar trends again, but slightly different values. As the duration is expanded to 80 CAD, the BSFC increases and the IMEP decreases. Since timings for these two are similar (Figure 4.36), this suggests a decrease in volumetric efficiency, which can be seen in the large decrease in airflow rates between 60 and 80 CAD of NVO. The combustion efficiency seems to drop slightly, but not significantly as the emissions (Figure 4.40 and 4.41) remain close in value.

The NVO durations of 60 and 80 CAD show a decrease in IMEP and increase in BSFC as CA50 in Figure 4.36 advances before 0 CAD aTDC. The other region remains approximately flat. This confirms that the most fuel efficient location for CA50 is somewhere after TDC, but the exact maxima of IMEP is not seen due to limited valve timings available. Again, 40 CAD of NVO duration shows erratic behavior and a trend could not be discerned.

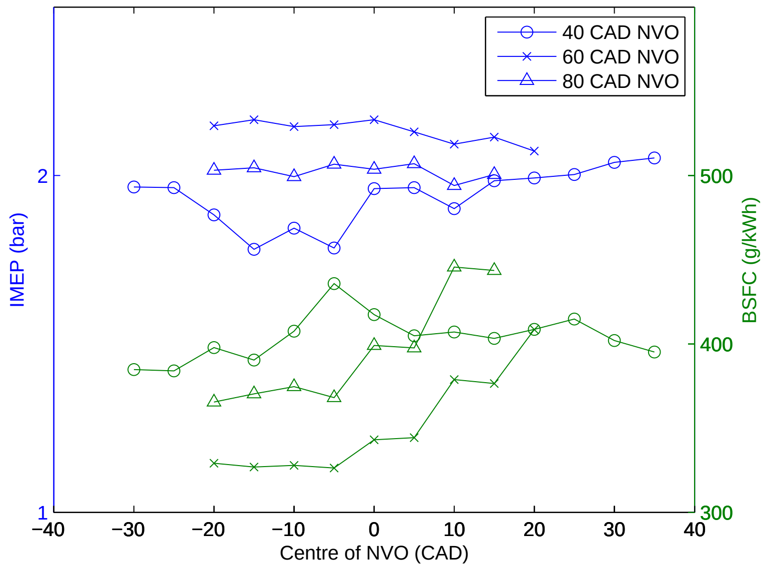

Figure 4.37: Variation of load (IMEP) and fuel efficiency (BSFC) plotted against the centre of NVO timing.

As expected, airflow and lambda follow similar trends in all three durations, shown in Figure 4.38. The airflow and lambda show a maximum in all three durations around the SNVO point. This suggests the volumetric efficiency of the valve timings is highest when the EVC and IVO timings are close to symmetric. This figure also shows that as NVO duration increases, airflow through the engine decreases. This is expected, as when NVO duration increases, there is less air expelled and inducted into the engine, as more time during those strokes the valves are closed.

Exhaust temperature for all three durations shows a local minimum at -5 CAD

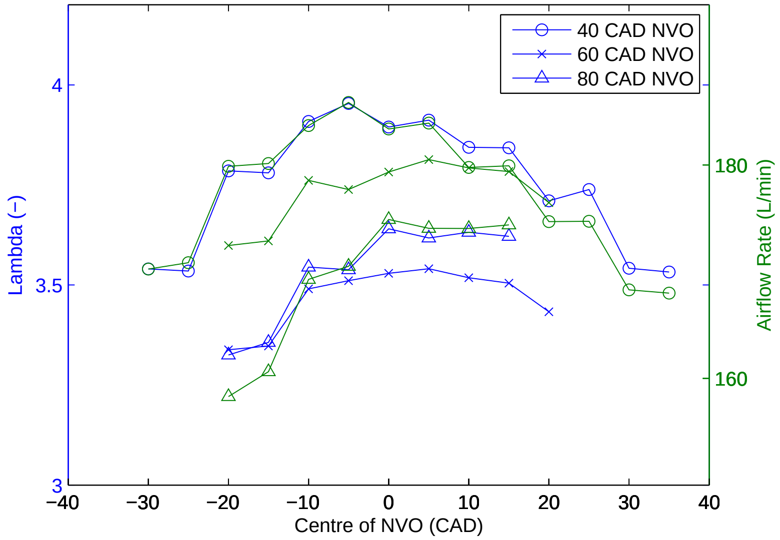

Figure 4.38: Variation of lambda and intake airflow plotted against the centre of NVO timing.

aTDC, suggesting combustion temperatures are lowest near symmetric NVO timings. This is shown in Figure 4.39. Local maxima/minima can also be seen in CO and CO_2 values in Figure 4.40. Figure 4.41 also shows peaks in both O_2 and hydrocarbons about the symmetric point. Because of the lower temperature, less CO converted to CO_2 and more O_2 and hydrocarbons in the exhaust, the results from these three figures suggest less complete combustion near SNVO timings.

Figure 4.40 show inverse relationships between CO and CO_2 for all NVO durations. This suggests that they are linked to combustion efficiency and completeness of the combustion.

The O_2 and hydrocarbons in the exhaust stream mimic the behaviour of airflow and lambda for all three NVO durations. In Figures 4.39, 4.40 and 4.41 the 40 CAD of NVO duration shows a lower exhaust temperature and CO_2 emissions and higher CO, O_2 and hydrocarbon emissions. The 60 and 80 CAD of NVO durations both share similar values and trends in the three figures.

NO_x for all valve durations and location timings in this section were found to be

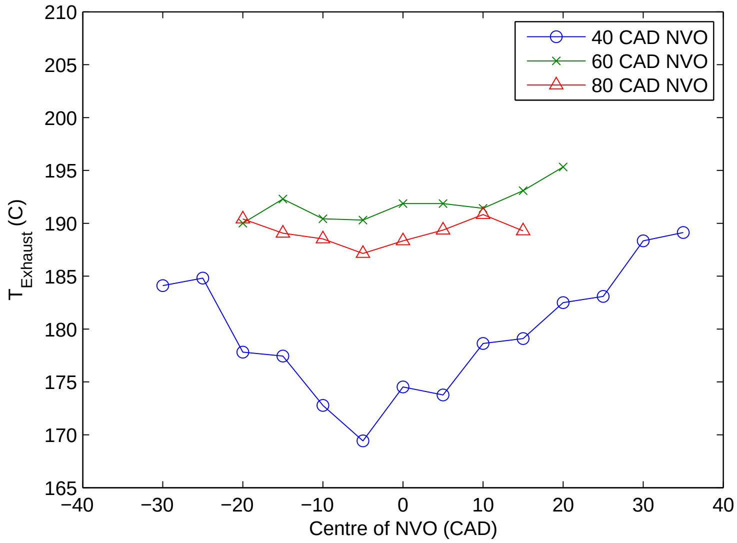

Figure 4.39: Variation of exhaust temperature plotted against the centre of NVO timing.

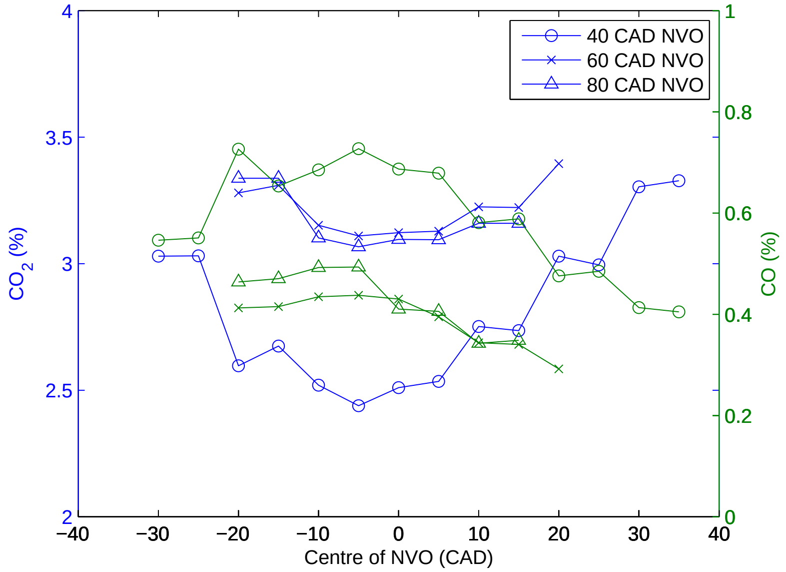

Figure 4.40: Variation of CO_2 and CO emissions plotted against the centre of NVO timing.

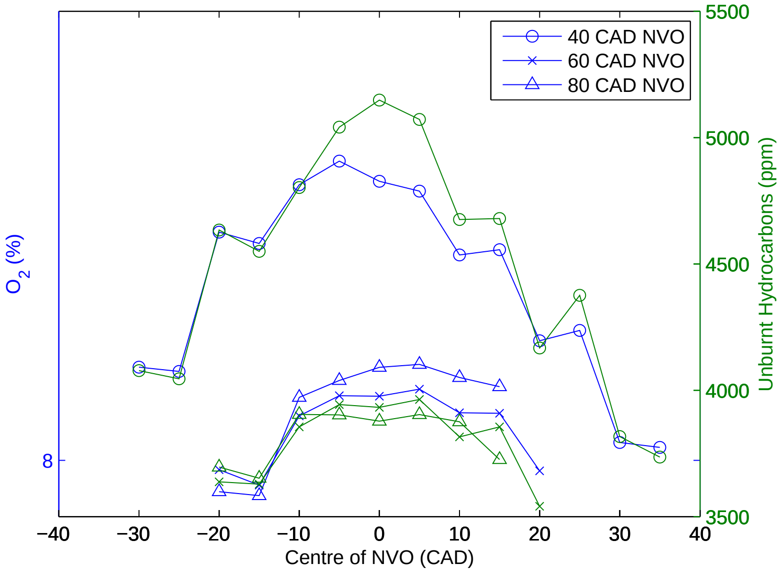

Figure 4.41: Variation of O_2 and hydrocarbon emissions plotted against the centre of NVO timing.

approximately 19 ppm and within the ±2 ppm experimental error given in Section 3.5. The values are therefore found to have no relation to the valve timings.

4.8 Trade-Offs within NVO Valve Strategies

In this section the applications and trade-offs of the different valve timing strategies presented in this study will be discussed. First, using the data from the asymmetric section, a sensitivity study is conducted. The results are tabulated in Tables 4.1 and 4.2. The units are given in CAD of combustion timing per CAD in NVO change, whether it be duration or centre of duration timing with respect to TDC. The most effective areas for control purposes are shown to be NVO duration changes at 40 CAD of NVO duration in the area of symmetric and late asymmetric centred timings. For constant duration sensitivity, 80 CAD of duration moved around symmetric TDC timings and 40 CAD of duration in the late centre timing region show the most sensitivity to combustion timing.

Location of NVO aTDC	-20 CAD	0 CAD	15 CAD
$\frac{\Delta CA50}{\Delta NVO Duration}$ at 40 CAD	-0.03	-0.13	-0.14
$\frac{\Delta CA50}{\Delta NVO Duration}$ at 80 CAD	0.01	-0.01	-0.03

Table 4.1: Sensitivity of combustion timing (CA50) to the duration of NVO at several different asymmetric timing locations for PRF0.

NVO Duration	40 CAD	60 CAD	80 CAD
$\frac{\Delta CA50}{\Delta NVO Location}$ at -20 CAD aTDC	0.06	-0.03	0.00
$\frac{\Delta CA50}{\Delta NVO Location}$ at 0 CAD aTDC	-0.03	-0.08	-0.16
$\frac{\Delta CA50}{\Delta NVO Location}$ at 15 CAD aTDC	-0.15	-0.12	0.07

Table 4.2: Sensitivity of combustion timing (CA50) to the asymmetric NVO timing location at several different NVO durations for PRF0.

A two-stage operating range is shown in the SNVO timing sections. In the range of SNVO durations between 0 and 100 CAD, we see little change in combustion timing in the first 40 CAD of change with the PRF0 fuel, but a near linear change in PRF20 and after 40 CAD for PRF0. The second range begins at 120 CAD where the timing retards suddenly compared to 100 CAD. The two ranges respond differently to load changes. Where the first range's overall slope decreases as the load decreases, the second range is not affected, allowing the two ranges to cross at a load of approximately 1.5 bar IMEP for both fuels. This dual range behavior can be seen by the "hump" witnessed in the contour plots of this chapter – this is partially attributed to unknown intake dynamic oscillations present that can be significant in a single cylinder engine.

The only major trade-off to the sensitivity of CA50 versus SNVO is the increase in BSFC as SNVO duration is increased. There is slight changes in load as well, although not significant. The CO_2 emissions increase while the CO and hydrocarbon emissions decrease. There is an apparent trade-off between combustion efficiency and load. This study was conducted at low loads and speeds, with low burn durations and timings around TDC. If the combustion event occurs prior to TDC, the rapid compression of the mixture during the burn will cause a more complete combustion efficiency, while decreasing the load due to the negative work exerted on the piston crown during its upstroke. If the combustion event occurs slightly after TDC, then the opposite occurs, with the load increasing due to more work being exerted on the piston crown during its downstroke, but a less complete combustion efficiency due to a less rapid pressure and temperature rise.

Asymmetric NVO timings show higher sensitivity in the late-EVC region. The trade-offs are also similar to that of symmetric timing: An increase in BSFC results in a slight change in load, an increase in CO_2 emissions and a decrease in CO and hydrocarbon emissions.

Chapter 5

Timing Control of HCCI[1,2]

In this chapter, HCCI ignition timing control strategies that are implemented on the single cylinder engine are described and results presented.

5.1 PI Controller

As a baseline case, a Proportional-Integral (PI) controller is implemented to control the combustion timing. It is implemented through Simulink on the dSpace Microautobox, with measured input of CA50 signal received from CAS. The controller output to the engine via valves is the amount of SNVO. The controller is used to track a CA50 setpoint. The equation implemented for the PI controller is:

$$u_k = u_{k-1} + K_p e_k + 0.5 K_i T_s (e_k + e_{k-1}) \tag{5.1}$$

Where u_k is the controller output, K_P is the proportional gain with a value of 4, K_I is the integral gain with a value of 6, T_s the sampling time which varies with engine speed, here at $N = 800$ RPM it is 0.146s, and e_k is the error between desired CA50 and measured CA50. The values for the gains are manually tuned in simulation using

---

[1] This work is done in conjunction with Khashayar Ebrahimi and is partially based on [Ebrahimi and Koch, 2013] [Ebrahimi et al., 2014] and [Ebrahimi et al., 2013].

[2] My contribution is the experimental implementation.

the detailed physical model [Ebrahimi et al., 2013].

Two setpoint steps are implemented to show the effectiveness of the control. The first is a step from CA50 at 3 CAD aTDC to -1 CAD aTDC, and the second is the reverse. The values seen by the dSpace controller (dSpace Microautobox - see Figure 3.4) are shown in Figures 5.1 and 5.2.

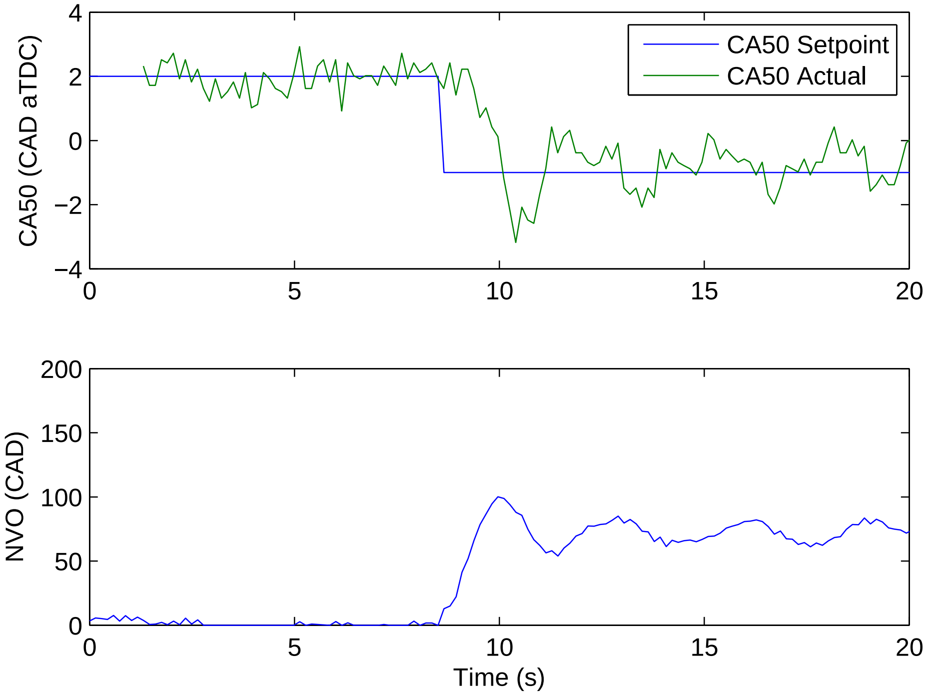

Figure 5.1: Single cylinder step test of the PI controller at a fuelling rate of 0.4 kJ per cycle PRF0.

The CA50 has substantial variability which is attributed to combustion timing variability at these low load operating points. The variability of CA50 is treated as noise in the controller. The signal tracks the setpoint even though the noise of CA50 is large. Due to the integral action of the PI controller the signal average remains near the setpoint. The response time is approximately 1.5 seconds for a step down in setpoint, which correlates to approximately 10 cycles and approximately 0.5 seconds for a step up, or four cycles. [Agrell et al., 2003a] presents a PI controller as well.

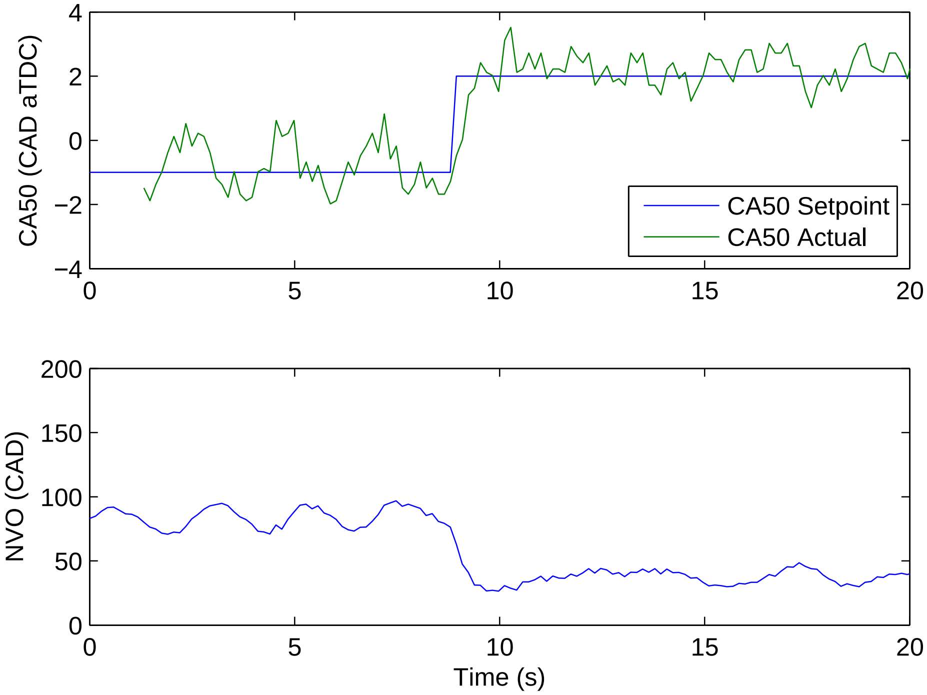

Figure 5.2: Single cylinder step test of the PI controller at a fuelling rate of 0.4 kJ per cycle PRF0.

Response times for that controller are 1 second, about eight cycles, although during a load step disturbance, the response time dropped to 5 seconds, approximately 42 cycles. That shows that there is possible room for improved step response speed of the PI controller.

5.2 Model Based Feed Forward Controller with Integrator

To improve the response time of the control, a feed forward/feedback controller is developed. The controller uses a look-up table of desired CA50 and current fuelling rate and gives an appropriate NVO for the setpoint. This table is developed using the control oriented model described in [Ebrahimi et al., 2013]. An integrator feedback loop is then added to reject the steady state error. The schematic of this controller can be seen in Figure 5.3. The value of the integral gain is set to 3, and the sampling time remains at 0.146 seconds.

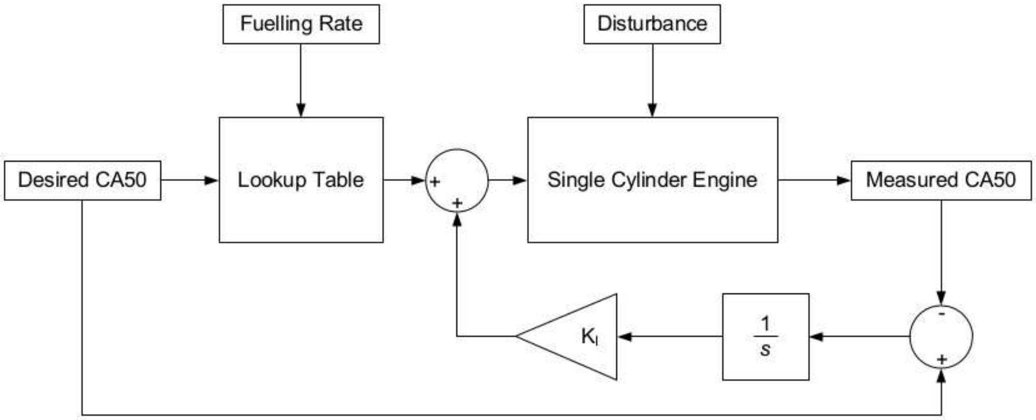

Figure 5.3: Schematic of the model based feed forward with integrator controller.

This controller is then put through some step tests. The results of these tests can be see in Figure 5.4.

The feed forward part of this controller provides a much better response time when compared to the PI controller. The rise time for the feed forward controller is

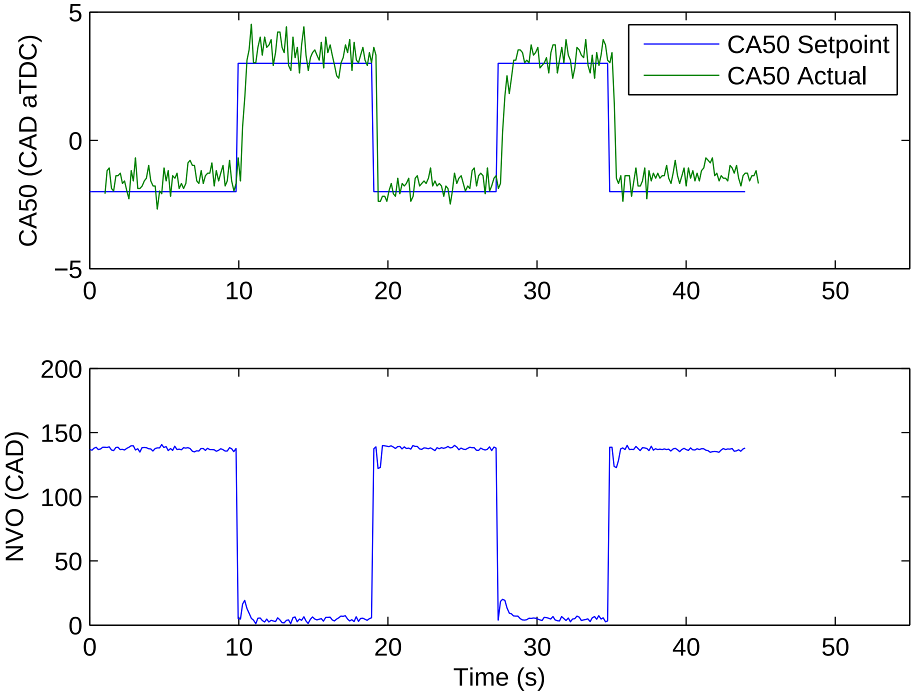

Figure 5.4: Single cylinder step test of the model based feed forward with integrator controller at a fuelling rate of 0.4 kJ per cycle PRF0.

on average approximately four cycles. This is compared to an average of seven cycles for the PI controller. This shows a decrease of over 40% in rise time. The CA50 reference step input applied to the feed forward controller is also one CAD larger than that of the PI controller. [Lundstrom, 2006] developed a controller using black-box modelling and pole-placement/loop-shaping, and resulted in a rise time of 5-7 cycles. The setup time for that controller is also significantly larger. [Bengtsson et al., 2006] uses physical modelling similar to this study, and developed a controller using loop-shaping, which also resulted in a larger rise time of approximately 12 cycles. The controller presented here therefore shows improvement over these controllers, although only for a limited load range. A wider load range can be implemented using feed forward tables which can be pre-calculated using the control oriented model described in [Ebrahimi et al., 2013].

5.3 Empirically Based Feed Forward Controller with Integrator

The feed forward controller discussed above uses a table calculated through the use of the control oriented model. In an attempt to develop more accurate data, the table is tuned using the experimental data. The data collected is at steady state, and the CA50 versus fuelling rate table is created using cubic interpolation to find SNVO durations at appropriate CA50 values. The control structure and implementation is exactly the same as above, only the table values are now based on experiment. The controller is put through the same step tests as above, and compared to the feed forward controller based on the engine model.

Figure 5.5 shows a rise-time for the empirical table on average of approximately six cycles. This is slower than the model-based controller, which shows a rise time of just four cycles on average. This shows that the model-based lookup table takes into consideration transients, where as the empirically-based table relies on steady-state

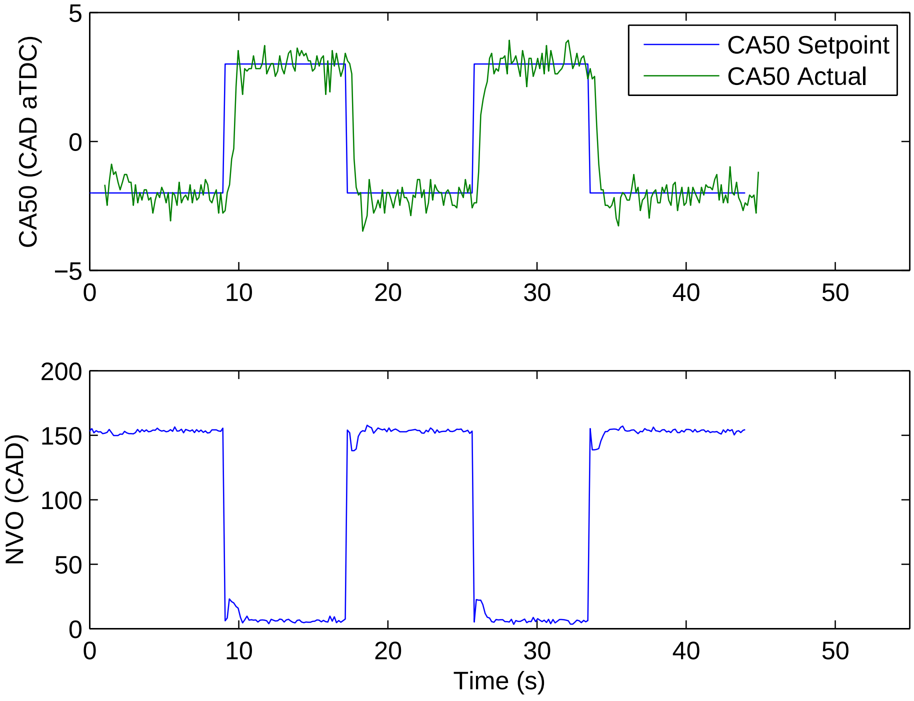

Figure 5.5: Single cylinder step test of the empirically based feed forward with integrator controller at a fuelling rate of 0.4 kJ per cycle PRF0.

tests to find NVO durations. This experimental table is also time consuming to fill with values as every point must be run on the engine.

CHAPTER 6

CONCLUSIONS

Conclusions and future work are described in this chapter.

6.1 Conclusions

The goal of this study is to investigate the effects of various valve timing strategies on HCCI combustion characteristics. A single cylinder engine is run through different operating points using state-of-the-art EVVT to apply cycle-by-cycle independent valve timings. The main valve timings changed are EVC and IVO, which are set to negative valve overlap, or NVO. This allows internal residual to be trapped within the cylinder which causes more heat to be retained in the mixture of the next cycle, as well as dilution, chemical and thermal effects.

The first strategy investigated is symmetric NVO, denoted SNVO, where both EVC and IVO are varied symmetrically about TDC of the gas exchange. This strategy showed a range of effects, including timing, load, efficiency and emissions. This strategy is acceptable for use in controlling combustion timing in HCCI operation. The engine had different responses to the symmetric strategy for low compared to high SNVO durations. The overall effects of increasing symmetric NVO duration are:

- An advance in combustion timing, as well as shorter burn duration.

- Since the engine is operated lean, a decrease in lambda and an increase load.
- An increase in BSFC.
- An increase in exhaust temperature.
- A decrease in fresh air intake.
- An increase in CO_2 emissions and a decrease in O_2, CO and hydrocarbon emissions.

The effects of PRF is also investigated in conjunction with SNVO. While a higher PRF produced a later combustion timing, longer burn and higher load, the region between misfire and knock is narrower.

Another strategy investigated is that of asymmetric NVO timings, where EVC and IVO are held a certain duration apart, then that duration is moved with respect to TDC of the gas exchange. This strategy showed more varied effects over the range of NVOs investigated, although in some ranges this strategy showed high sensitivity to combustion timing.

Using the knowledge gained from the valve timing investigations, controllers to control combustion timing in HCCI operation are implemented on the single cylinder engine. Initially a PI controller using the EVVT valves is found to perform similar to other VVT applications in the literature. Then a feed forward with integral action controller is implemented using a look up table parameterized by the model presented in [Ebrahimi et al., 2013]. This controller had excellent transient response to set point changes in CA50 and could reach the setpoint within four cycles.

6.2 Future Work

- A more in-depth investigation into the effects of asymmetric NVO is suggested, using a wider range of timings as well as different PRF fuels. This would allow the effects of the timings to be better understood, and the varied behavior of the timings investigated.

- Use of different fuels such as bio-fuels could be investigated using the same valve strategies and compared to the results of the primary reference fuels.
- More complex controllers that can handle a wider array of operating conditions while also taking into account the numerous constraints of the valves and range of engine operation between misfire and knock.
- Focus on higher extending the HCCI operating conditions into higher loads and engine speeds by maintaining CA50 timing after TDC.
- A dynamic analysis of the residual fraction so an accurate value for residual can be calculated during transients.

Appendix A

Engine Procedures

A.1 Engine Operating Procedure

For engine operation, follow these steps:

1. Turn on all devices, including:
    - Transducer pump
    - Valve controllers (2)
    - Valve power supplies (2)
    - CO canary and Lambda sensor
    - Power bar and three power supplies
    - Microautobox and CAS system
    - MTS board
    - Air and water
    - Fuel pumps and release tank screws
2. Turn on all four computers needed, including:
    - Valve computers (2)

- ADAPT/dSapce computer
- CAS Computer

3. Run ADAPT on the ADAPT/dSpace computer desktop, click ‘Yes’. Under ‘Control’ menu, click select test and select ‘phaser_sep28.tst’. Errors should occur in the error window, this is fine.

4. Under ‘Control’ menu, click start test, increment the test number by one, click ‘OK’.

5. Click ‘Manual’, then ‘Reset Safety String’. Wait for the indicators to go green and the fans turn on, then click ‘Start Dyno Drive’.

6. Set desired RPM, coolant temp, oil temp, air temp and throttle position. Do not forget to turn on the temp controllers.

7. On the valve computers (procedure is the same for both) go to ‘D:\mm\dspace’, right click on ‘fluxrev6’ and click command prompt here.

8. Type ‘down1103 fr.mk’ and hit enter.

9. When the build process is complete open Control Desk from the desktop. Click ‘File>Open Experiment’. Open ‘ValveControlv3a.cdx’. Once open, click the ‘Parameter’ tab on the bottom and drag the divider bar up. right click on ‘bk1_hand_flt4’ and click ‘Declare status set’. Click ‘Parameter Editor>Write’ all parameters now. Then click the ‘Run’ mode.

10. On the intake valve, increase the brake current to 9.

11. On the exhaust valve, increase the opener current to 5.5, the closer current to 4.7 and set the brake velocity to 3.5.

12. Turn on power on both valves. Click ‘Fail’ then ‘Swing’ until the valve shuts, then click the RPM box. Repeat for both valves
13. Once the valves are running with the engine motoring, run CAS on the CAS computer desktop. Connect to the CAS computer, and click the green flag to start the pressure trace.
14. Open Control Desk on the ADAPT/dSpace computer desktop. ‘File>Open Experiment’ and select the experiment you wish to run. Click the ‘Run’ mode and press F11 for fullscreen.
15. Once ready for fuel, turn on the emergency switch on the desk. If the valves fail during the test, immediately turn this switch off to stop the fuel injection.

To take data in dSpace, make sure you drag any parameters from the bottom of the screen into the data log box (a good starting set is to drag all the values under ‘Labels’). Once the engine is running, make sure the data log is on cycle-based, and click ‘Take’. Once it is completed, click ‘Save’ and save where you want the data. For ADAPT, click ‘Data>Save Data’, once completed click ‘Report>Data Report’ and click ‘Save’ and save where you want the data, then click ‘Done’. For CAS, make sure you setup the data save under ‘Data>Save Data Setup’, then click ‘Data>Save Data’.

The shut down is essentially the reverse of the power up phase of this procedure. Hit ‘Stop’ on the ADAPT screen, then ‘Control>Stop Test’ and close adapt. Click ‘Animation Mode’ on all three Control Desk Applications (dSpace and the two valves) and click the stop button, then close the Control Desks. Click the red flag in CAS then close CAS. Then turn off everything from step 1.

A.2 dSpace Controller Design Procedure

When a new Simulink model is desired, open MATLAB on the ADAPT/dSpace computer desktop. When loaded, type ‘tdc=230;’ and hit enter. Make sure the MATLAB workspace is set to ‘C:\MATLAB_R2007a\work\Fall2009’. Open the desired model to be modified. Click ‘Save As’ and rename if it is becoming a new model. Once the re-designs are completed, press ‘Ctrl+B’ to build the model.

If a new Control Desk experiment is required, copy a whole file over from a similar experiment and open it. In the parameter window at the bottom, right click on the .sdf and click ‘replace .sdf’. Choose your newly built .sdf from the MATLAB folder. Remove the old .sdf from the experiment, add in the new one and refresh implicit files (off a right click in the experiment browser). Save as a new experiment, close and reopen. Then load the new .sdf onto the MicroAutobox. Be sure to load any parameters into the Data Log box before starting the experiment.

A.3 Emissions Bench Procedure

To take emissions data, follow the same procedure as engine operation, but turn on the emissions bench by turning on the sample pump and the four switches on the emissions bench. Be sure the H_2 and N_2 bottles are also open. Once the bench is on, click the ‘Flame’ button on the hydrocarbon analyzer. On the emissions screen of the ADAPT interface, click the ‘downstream’ button. The emissions bench is now ready for experiments.

For calibration, go to the emissions bench screen in on the ADAPT interface. Make sure all the gas bottle are open. To zero out all the analyzers, click the ‘zero calib’ button and wait until the the analyzers settle, then hit the ‘zero’ buttons on the analyzers, or under the calibration menu (password is 111) hit the zero calibration. Then repeat for each analyzer using the span instead of zero. Make sure the span is set to the same as the concentration on the bottle.

Appendix B

Experimental Data

Date Collected	Number of Test Points	Description
July 19, 2012	9	Model Validation
August 28, 2012	5	Model Validation
September 8, 2012	11	Model Validation
September 25, 2012	8	Model Validation
October 2, 2012	20	Model Validation
October 5, 2012	10	Model Validation
November 8, 2012	8	Model Validation
December 21, 2012	6	Model Validation
January 23, 2013	6	Model Validation
January 29, 2013	148	Mapping
February 7, 2013	3	Model Validation
February 15, 2013	3	Model Validation
May 6, 2013	1	Frequency Analysis
May 7, 2013	1	Frequency Analysis
May 8, 2013	2	Frequency Analysis
May 9, 2013	1	Frequency Analysis
May 16, 2013	30	Frequency Analysis
June 11, 2013	1	PI
June 13, 2013	1	PI
August 20, 2013	17	Controller
August 22, 2013	55	Mapping
September 3, 2013	9	Controller
October 24, 2013	4	Model Controller and Repeatability
December 11, 2013	7	RBS and Repeatability
December 17, 2013	6	RBS and Repeatability
January 16, 2014	1	RBS
January 20, 2014	5	Asymmetric Mapping
January 29, 2014	9	Asymmetric Mapping
February 6, 2014	24	Observer Test and Asymmetric Mapping
February 13, 2014	3	MPC Test
February 17, 2014	1	MPC Test
March 13, 2014	4	Observer, PI and MPC Test
March 17, 2014	2	Feedforward Test
April 10, 2014	2	Fuel RBS
May 1, 2014	2	NVO Model Input
May 5, 2014	6	PRBS

Table B.1: Experimental Data Summary

File Name	Description
adapt.m	Code for extracting values from imported Adapt data
adaptcsvchange.m	Code for modifying Adapt csvs for use in Matlab
DATAMASTER.m and variations thereof	Code for extracting and calculating needed data from mapping experiments
derivativeP.m	Code for calculating multiple derivatives of the pressure trace
Dspace_Data.m	Code for extracting values from imported dSpace data
ERRORCALC.m	Code for calculating sample error from one test point
FFTsystem.m	Frequency analysis code
HRfcn.m	Code called by other codes when heat transfer analysis data was needed
Interpolation.m	Code used to line up input and output data's sampling times by interpolation
knockcharateristics.m	Code used to looked at different knock characteristics
LINEARIZINGFORMULA.m	Code used when looking at different linearizing options
linecount.pl	Python code called in adaptcsvchange.m to count lines in a csv
loadgraph.m	Plotting code
MA.m	A discrete filter type code
max1.m	Code called in DATA.m codes
min1.m	Code called in DATA.m codes
plotcontour.m	Plotting code
plotIVC.m	Plotting code
plotNVO.m	Plotting code
plots.m	Plotting code
plotyyy.m	Downloaded code for plotting on 3 y-axes
spectrumsys.m	Frequency analysis code
spectrumXY.m	Frequency analysis code
subplots.m	Plotting code
subplotyu.m	Plotting code
THESIS_cas2mat_converter.m	Code to convert CAS files to Matlab files
timestep.m	Code to calculate the timestep in data
tIVC.m	Sampling time adjustment code
tNVO.m	Sampling time adjustment code
truncate.m	Code use to truncate data

Table B.2: Computer Program Summary

References

Abd-Alla, G. (2002). Using exhaust gas recirculation in internal combustion engines: a review. *Energy Conversion and Management*, 43(8):1027 – 1042.

Abernethy, R., Benedict, R., and Dowdell, R. (1985). ASME measurement uncertainty. *ASME Journal of Fluids Engineering*, 107(2):161–164.

Agarwal, D., Singh, S. K., and Agarwal, A. K. (2011). Effect of exhaust gas recirculation (EGR) on performance, emissions, deposits and durability of a constant speed compression ignition engine. *Applied Energy*, 88(8):2900 – 2907.

Agrell, F. (2006). *Control of HCCI by aid of Variable Valve Timings with Specialization in Usage of a Non-Linear Quasi-Static Compensation.* PhD thesis, KTH.

Agrell, F., Ångström, H.-E., Eriksson, B., Wikander, J., and Linderyd, J. (2003a). Integrated simulation and engine test of closed loop HCCI control by aid of variable valve timings. In *SAE Paper 2003-01-0748*.

Agrell, F., Ångström, H.-E., Eriksson, B., Wikander, J., and Linderyd, J. (2003b). Transient control of HCCI through combined intake and exhaust valve actuation. In *SAE Paper 2003-01-3172*. SAE International.

Allen, J. and Law, D. (2002). Variable valve actuated controlled auto-ignition: Speed load maps and strategic regimes of operation. In *SAE Paper 2002-01-0422*. SAE International.

Atkins, M. A. and Koch, C. R. (2003). A well-to-wheel comparison of several powertrain technologies. In *SAE Paper 2003-01-0081*.

Atkins, M. J. (2004). Experimental examination of the effects of fuel octane and diluent on HCCI combustion. Master's thesis, University of Alberta.

Audet, A. (2008). Closed loop control of HCCI using camshaft phasing and dual fuel. Master's thesis, University of Alberta.

Audet, A. and Koch, C. R. (2009). Actuator comparison for closed loop control of HCCI combustion timing. In *SAE Paper 2009-01-1135*, page 8.

Bengtsson, J., Strandh, P., Johansson, R., Tunestal, P., and Johansson, B. (2006). Model predictive control of homogeneous charge compression ignition (HCCI) engine dynamics. In *Computer Aided Control System Design, 2006 IEEE International Conference on Control Applications, 2006 IEEE International Symposium on Intelligent Control, 2006 IEEE*, pages 1675–1680. IEEE.

Bidarvatan, M., Shahbakhti, M., Jazayeri, S., and Koch, C. (2014). Cycle-to-cycle modeling and sliding mode control of blended-fuel HCCI engine. *Control Engineering Practice*, 24(0):79 – 91.

Bögemann, S. (2009). Control design for disturbance rejection on a HCCI model. Master's thesis, Technische Universiteit Eindhoven.

Camacho, E. F. and Bordons, C. (2004). *Model Predictive Control*. Springer.

Caton, P. A., Song, H. H., Kaahaaina, N. B., and Edwards, C. F. (2005). Strategies for achieving residual-effected homogeneous charge compression ignition using variable valve actuation. In *SAE Paper 2005-01-0165*. SAE International.

Chen, R., Milovanovic, N., Turner, J., and Blundell, D. (2003). The thermal effect of internal exhaust gas recirculation on controlled auto ignition. In *SAE Paper 2003-01-0751*. SAE International.

Chladny, R. R. (2003). Modeling and simulation of automotive gas exchange valve solenoid actuators. Master's thesis, University of Alberta.

Chladny, R. R. and Koch, C. R. (2008). Flatness-based tracking of an electromechanical VVT actuator with disturbance observer feed-forward compensation. *IEEE Transactions on Control Systems Technology*, 16:652–663.

Chladny, R. R., Koch, C. R., and Lynch, A. F. (2005). Modeling of automotive gas-exchange solenoid valve actuators. *IEEE Transactions on Magnetics*, Volume 41, Issue 3:1155–1162.

Christensen, M., Johansson, B., and Hultqvist, A. (2001). The effect of piston top-land geometry on emissions of unburned hydrocarbons from a homogeneous charge compression ignition (HCCI) engine. In *SAE Paper 2001-01-1893*. SAE International.

Dec, J. E. and Sjöberg, M. (2003). A parametric study of hcci combustion - the sources of emissions at low loads and the effects of gdi fuel injection. In *SAE Paper 2003-01-0752*. SAE International.

DOT, NHTSA (2012). 2017 and later model year light-duty vehicle greenhouse gas emissions and corporate average fuel economy standards; final rule. Federal Register Vol. 77, No. 199.

Ebrahimi, K. and Koch, C. R. (2013). HCCI combustion timing with variable valve timing. *American Control Conference*, 1:1.

Ebrahimi, K., Schramm, A., and Koch, C. R. (2013). A control oriented model with variable valve timing for HCCI combustion timing control. In *SAE Paper 2013-01-0588*, page 12.

Ebrahimi, K., Schramm, A., and Koch, C. R. (2014). Feedforward feedback control of HCCI combustion timing. In *2014 American Controls Conference (ACC), Portland, USA*, page 6.

EPA (2012). EPA and NHTSA set standards to reduce greenhouse gases and improve fuel economy for model years 2017-2025 cars and light trucks. Regulatory Announcement, EPA-420-F-12-051.

EPA (2013). Control of air pollution from motor vehicles: Tier 3 motor vehicle emission and fuel standards; proposed rule. Federal Register Vol. 78, No. 98.

Franklin, G. F., Powell, J. D., and Emami-Naeini, A. (2010). *Feedback Control of Dynamic Systems*. Pearson Education Inc.

Ghazimirsaied, A. (2012). *Extending HCCI Low Load Operation Using Chaos Prediction and Feedback Control*. PhD thesis, University of Alberta.

Ghazimirsaied, A. and Koch, C. R. (2012). Controlling cyclic combustion timing variations using a symbol-statistics predictive approach in an HCCI engine. *Applied Energy*, 92(0):133 – 146.

Haraldsson, G., Tunestl, P., and Hyvönen, J. (2002). HCCI combustion phasing in a multi cylinder engine using variable compression ratio. In *SAE Paper 2002-01-2858*. SAE International.

Haraldsson, G., Tunestl, P., and Johansson, B. (2004). HCCI closed-loop combustion control using fast thermal management. In *SAE Paper 2004-01-0943*. SAE International.

Heywood, J. B. (1988). *Internal Combustion Engine Fundamentals*. McGraw-Hill, Inc.

Jungkunz, A. F. (2013). *Actuation strategies for cycle-to-cycle control of homogeneous charge compression ignition combustion engines*. PhD thesis, Stanford University.

Law, D., Kemp, D., Allen, J., Kirkpatrick, G., and Copland, T. (2001). Controlled combustion in an IC-engine with a fully variable valve train. In *SAE Paper 2001-01-0251*. SAE International.

Ljung, L. (1999). *System Identification: Theory for the User (2nd Edition)*. Prentice Hall.

Lundstrom, M. (2006). Model based HCCI engine combustion control. Master's thesis, KTH.

Lupul, R. (2008). Steady state and transient characterization of a HCCI engine with varying octane fuel. Master's thesis, University of Alberta.

Mashkournia, M. (2012). Electromagnetic variable valve timing on a single cylinder engine in HCCI and SI. Master's thesis, University of Alberta.

Mashkournia, M., Audet, A., and Koch, C. R. (2011). Knock detection and control in an HCCI engine using DWT. In *Proceedings of the ASME 2011 Dynamic Systems and Control Conference, Morgantown, USA*, pages 391–399. ASME.

Moffat, R. J. (1988). Describing the uncertainties in experimental results. *Experimental thermal and fluid science*, 1(1):3–17.

Najt, P. M. and Foster, D. E. (1983). Compression-ignited homogeneous charge combustion. In *SAE Paper 1983-0264*.

Seethaler, R., Mashkournia, M., Chladny, R. R., Zhao, J., and Koch, C. R. (2013). Closed loop electromagnetic valve actuation motion control on a single cylinder engine. In *SAE Paper 2013-01-0594*, page 8.

Shaver, G., Gerdes, J., and Roelle, M. (2004). Physics-based closed-loop control of phasing, peak pressure and work output in HCCI engines utilizing variable valve actuation. In *American Control Conference, 2004. Proceedings of the 2004*, volume 1, pages 150 –155 vol.1.

Shi, L., Cui, Y., Deng, K., Peng, H., and Chen, Y. (2006). Study of low emission homogeneous charge compression ignition (HCCI) engine using combined internal and external exhaust gas recirculation (EGR). *Energy*, 31(14):2665 – 2676.

Stolk, T. and Gaisberg, A. (2001). Elektromagnetischer aktuator. *German Patent Application DE 10025491 A1.*

Weall, A., Szybist, J., Edwards, K., Foster, M., Confer, K., and Moore, W. (2012). HCCI load expansion opportunities using a fully variable HVA research engine to guide development of a production intent cam-based VVA engine: The low load limit. *SAE Int. J. Engines*, 5(3):1149–1162.

Weissler, P. (2013). Larger vehicles will remain available in 2025, despite cafe. *http://articles.sae.org/*.

Widd, A. (2009). *Predictive control of HCCI engines using physical models.* Department of Automatic Control, Lund University.

Widd, A., Johansson, R., Borgqvist, P., Tunestl, P., and Johansson, B. (2011). Investigating mode switch from SI to HCCI using early intake valve closing and negative valve overlap. In *SAE Paper 2011-01-1775*. Copyright 2011 Society of Automotive Engineers of Japan, Inc. and SAE International.